2014-12

COMPARISON BETWEEN TWO SENSORS AND MULTIPLE SENSORS WITH TOA AND TDOA/FDOA FUSIONS AND NON-FUSIONS UNDER NOISE JITTER MITIGATION

Dobias, Richard G.

NAVAL POSTGRADUATE SCHOOL

MONTEREY, CALIFORNIA

THESIS

COMPARISON BETWEEN TWO SENSORS AND MULTIPLE SENSORS WITH TOA AND TDOA/FDOA FUSIONS AND NON-FUSIONS UNDER NOISE JITTER MITIGATION

by

Richard G. Dobias

December 2014

Thesis Advisor: Weilian Su
Second Reader: Tri Ha

Approved for public release; distribution is unlimited

THIS PAGE INTENTIONALLY LEFT BLANK

REPORT DOCUMENTATION PAGE

Form Approved OMB No. 0704–0188

1. AGENCY USE ONLY *(Leave blank)*	**2. REPORT DATE** December 2014	**3. REPORT TYPE AND DATES COVERED** Master's Thesis

4. TITLE AND SUBTITLE
COMPARISON BETWEEN TWO SENSORS AND MULTIPLE SENSORS WITH TOA AND TDOA/FDOA FUSIONS AND NON-FUSIONS UNDER NOISE JITTER MITIGATION

5. FUNDING NUMBERS

6. AUTHOR(S) Richard G. Dobias

7. PERFORMING ORGANIZATION NAME(S) AND ADDRESS(ES)
Naval Postgraduate School
Monterey, CA 93943-5000

8. PERFORMING ORGANIZATION REPORT NUMBER

9. SPONSORING /MONITORING AGENCY NAME(S) AND ADDRESS(ES)
N/A

10. SPONSORING/MONITORING AGENCY REPORT NUMBER

11. SUPPLEMENTARY NOTES The views expressed in this thesis are those of the author and do not reflect the official policy or position of the Department of Defense or the U.S. Government. IRB Protocol number ____N/A____.

12a. DISTRIBUTION / AVAILABILITY STATEMENT
Approved for public release; distribution is unlimited

12b. DISTRIBUTION CODE

13. ABSTRACT (maximum 200 words)

The prominence of geolocation technology and its demand has risen in recent years. Stringent and precise positioning is at the forefront of both civilian and military applications. The importance of precision leads to a rise in processing and algorithm run times. In addition, space, time and atmospheric conditions contribute to the complexity of geolocation operations.

Past research measured time-of-arrival, time-difference-of-arrival, and frequency-difference-of arrival under stringent conditions using a synthetic aperture approach of two airborne sensors. While four sensors have been proven to be ideal in the geolocation of an emitter, we aim to decrease the requirement to three sensors and retain the purity of the original two sensor algorithm. Three-sensor fusion from multiple time-samples enhances the precision of the estimate and provides the end-user a better positioning solution.

We propose the utilization of three airborne sensors collecting measurements from the synthetic aperture model. Sensor angular separation and aperture size are addressed. A thorough investigation into ionosphere mitigation is provided. Finally, an overall summary and comparison between two- and three-sensor approaches are documented.

14. SUBJECT TERMS Satellite, Global Positioning System, Ionosphere, Noise, Synthetic Aperture, Unmanned Aerial Vehicle, Sensors, Time of Arrival, Time Difference of Arrival, Frequency Difference of Arrival, Jitter, Fusion	**15. NUMBER OF PAGES** 139
	16. PRICE CODE

17. SECURITY CLASSIFICATION OF REPORT	**18. SECURITY CLASSIFICATION OF THIS PAGE**	**19. SECURITY CLASSIFICATION OF ABSTRACT**	**20. LIMITATION OF ABSTRACT**
Unclassified	Unclassified	Unclassified	UU

NSN 7540–01-280-5500

Standard Form 298 (Rev. 2–89)
Prescribed by ANSI Std. 239–18

THIS PAGE INTENTIONALLY LEFT BLANK

Approved for public release; distribution is unlimited

COMPARISON BETWEEN TWO SENSORS AND MULTIPLE SENSORS WITH TOA AND TDOA/FDOA FUSIONS AND NON-FUSIONS UNDER NOISE JITTER MITIGATION

Richard G. Dobias
Lieutenant, United States Navy
B.S. University of Memphis, 2009

Submitted in partial fulfillment of the
requirements for the degree of

MASTER OF SCIENCE IN ELECTRICAL ENGINEERING

from the

NAVAL POSTGRADUATE SCHOOL
December 2014

Author: Richard G. Dobias

Approved by: Weilian Su
Thesis Advisor

Tri Ha
Second Reader

Clark Robertson
Chair, Department of Electrical and Computer Engineering

THIS PAGE INTENTIONALLY LEFT BLANK

ABSTRACT

The prominence of geolocation technology and its demand has risen in recent years. Stringent and precise positioning is at the forefront of both civilian and military applications. The importance of precision leads to a rise in processing and algorithm run times. In addition, space, time and atmospheric conditions contribute to the complexity of geolocation operations.

Past research measured time-of-arrival, time-difference-of-arrival, and frequency-difference-of arrival under stringent conditions using a synthetic aperture approach of two airborne sensors. While four sensors have been proven to be ideal in the geolocation of an emitter, we aim to decrease the requirement to three sensors and retain the purity of the original two sensor algorithm. Three-sensor fusion from multiple time-samples enhances the precision of the estimate and provides the end-user a better positioning solution.

We propose the utilization of three airborne sensors collecting measurements from the synthetic aperture model. Sensor angular separation and aperture size are addressed. A thorough investigation into ionosphere mitigation is provided. Finally, an overall summary and comparison between two- and three-sensor approaches are documented.

THIS PAGE INTENTIONALLY LEFT BLANK

TABLE OF CONTENTS

LIST OF FIGURES

THIS PAGE INTENTIONALLY LEFT BLANK

LIST OF TABLES

THIS PAGE INTENTIONALLY LEFT BLANK

LIST OF ACRONYMS AND ABBREVIATIONS

BDS	Beidou Navigation Satellite System
CCMC	Community Coordinated Modeling Center
CT	computerized tomography
EKF	extended Kalman filter
FDOA	frequency difference of arrival
GLONASS	Global Navigation Satellite System
GPS	Geolocation Positioning System
KF	Kalman filter
MIDAS	Multi-Instrument Data Analysis System
MSE	mean square error
NLOS	non-line-of-sight
PIM	parameterized ionospheric model
PRN	pseudorandom
RMSE	root-mean-square error
SuPIM	Sheffield University Plasmasphere Ionosphere Model
TDOA	time difference of arrival
TEC	total electron content
TOA	time of arrival
UAV	unmanned aerial vehicles
UKF	unscented Kalman filter

THIS PAGE INTENTIONALLY LEFT BLANK

EXECUTIVE SUMMARY

The widespread use of Geolocation Positioning System (GPS) technology continues to grow with each passing year. Research is meeting the demand with new and ingenious ways of increasing precision, while maintaining a low computational demand in the use of time-of-arrival (TOA), time-difference-of-arrival (TDOA), and frequency-difference-of arrival (FDOA) algorithms. One tactic to maximize the performance of these algorithms is to employ them utilizing a synthetic aperture approach where the geolocation information from multiple time steps is fused into a single estimated position for the emitter. In using this approach, multiple estimates can be evaluated to provide a higher precision. The main goal of our research is to employ three airborne sensors collecting accurate measurements from the synthetic aperture model through the evaluation of sensor angular separation and aperture size. In addition, a thorough investigation into ionosphere mitigation is provided. Finally, an overall summary and comparison between two and three sensor approaches are documented.

In order to construct the fundamental understanding of the principles required to perform the testing of the research, we first describe the governing equations and applicable dimensional solutions for TOA, TDOA and FDOA. To provide real-world applicability of these algorithms, the algorithms are processed at two specific heights representing the operating parameters for satellite and unmanned aerial vehicle (UAV) sensors. Furthermore, the atmospheric effects to the signal are investigated as well as the appropriate models and mitigations are provided for precise geolocation operations. For satellite sensors, the various effects of the ionosphere are considered, and the total electron content (TEC) is used to provide the delay to the signal as it traverses the atmosphere. For UAV sensors, the effects of the troposphere are considered and provide the delay to the signal. Additionally, both satellite and UAV geolocation is tested under conditions where the respective delay is mitigated.

The main goal of this research with respect to the TOA algorithm was to test the geolocation performance of an unknown emitter utilizing a synthetic aperture model of three sensors and compare the results to that of two sensors. For the three-sensor

approach, at each time step of the synthetic aperture three measurements are calculated. Once the synthetic aperture distance D is completed, each sensor measurement is combined into a single estimate of the emitter's position. Overall, our results have a significantly lower root mean square (RMS) error for the three sensor model over the two sensor model; however, both models require additional noise mitigation techniques to be applied in order to lower the RMS error into ranges where it can be applied in real world scenarios. The three UAV sensor model also outperformed the two sensor model in testing. The lowest RMS error recorded by the three sensor model was 5.6 meters, eclipsing the precision of the two sensor model by 6.4 meters. As the results are suitable for high precision applications, the addition of further sensors to this model would serve to decrease the error further.

The research for the TDOA-FDOA fusion model was centered on the optimization of the bounding box with respect to the number of samples calculated for each time step of the synthetic aperture. For the three sensors satellite approach, at each time step of the synthetic aperture, six measurements are collected, which results in three TDOA measurements and three FDOA measurements. Once the satellites collect measurements across the synthetic aperture, they are combined into a single estimate of the emitter's position inside a cube, also referred to as the bounding box, which is centered on the best known position of the emitter. With sample points evenly mapped within the bounding box, the bounding box estimate and last known location points are used to calculate the lowest RMS error. In order to maximize the performance of the bounding box and discretization of the samples within it, an exhaustive search methodology was applied to determine the optimum ratio between the number of samples applied to the geolocation and the smallest bounding box size that resulted in the lowest possible RMS error in the geolocation solution. The optimum ratio was then tested by increasing the bounding box size by a factor of $(2+\Delta)g$ where Δ is the size of the next incremental step and g is one half of the cube's side length. The number of samples was also increased by increasing the original sample size by a factor of four for each increase in bounding box size. The results from the calculations show RMS error values as low as 0.001564 meters at 160 samples, which significantly outperforms TOA results. In order

to accomplish these high precision calculations, a priori information about the emitter's location must be included in the beacon symbol sent from the emitter to the sensors. This allows a reduction in the initial bounding box size and reduces the computational requirements of the geolocation calculation.

Future employment of the synthetic aperture algorithm requires a focus on decreasing the overall RMS error of the TOA model, implementing real time integration of atmospheric noise values into calculations, and further refining the TDOA-FDOA fusion algorithm to reduce computation times when large bounding box sizes are required. Prospective enhancements to the algorithm are addressed. In summary, the three sensor synthetic aperture approach produced significantly lower RMS error values than the two sensor model. More specifically, the UAV implementation is already capable of handling higher precision operations. The TDOA-FDOA fusion algorithm requires additional research to maximize the precision while minimizing the computational requirements.

THIS PAGE INTENTIONALLY LEFT BLANK

I. INTRODUCTION

A. BACKGROUND MOTIVATION

Over the last decade, there has been a sharp rise in the need for Geolocation Positioning System (GPS) information in the public, corporate, and military sectors. The rise of commercial applications for smart watches, cell phones, and cars has required location information for a wide range of products. The military's use of geolocation technology includes unmanned aerial vehicles (UAVs), precise weaponry, and more accurate search and location equipment. The applications using this technology require a high level of accuracy to meet the demands placed on them by the user. These users are taking the devices from the most remote locals to the highest mountaintops.

The systems and algorithms that make up GPS are constantly interacting with the environment, creating a highly sophisticated and constantly evolving process. As the Earth is impacted by natural and man-made events, GPS must be able to identify, process, and adjust to these fluctuations in real time. A loss of GPS data has devastating effects for unintended recipients of powerful munitions. The safety of commercial assets relies heavily on the accuracy that GPS can provide [1]. In addition, research continues to monitor and adjust to changes in space and the atmosphere that affect GPS [2]. Dedicated networks of computers and receivers constantly receive data on key indicators and report them to awaiting stations to update algorithms. As we move further into the twenty first century, the need for new research and analysis is required to meet the demand.

B. GEOLOCATION FUNDAMENTALS

The basic components of a geolocation system are composed of airborne sensors, a control network of satellites, and a user's device known as an emitter [3]. Airborne sensors are often composed of satellites in most applications, while Unmanned Ariel Vehicles (UAVs) can also be used. Global Positioning System (GPS) satellites circle the Earth in elliptical orbits and are equipped to transmit on two bands, 1575.42 MHz and 1227.6 MHz [4]. The control network monitors satellite position and timing. These measurements are relayed to the satellites to help ensure accuracy. The emitter relays a

beacon toward the airborne sensor. The beacon radiates in either line-of-sight (LOS) or non-line-of-sight (NLOS), depending on the environment of the emitter. Traditional GPS algorithms utilize time-of-arrival (TOA), time-difference-of-arrival (TDOA), or frequency-difference-of-arrival (FDOA) methods. TOA methods are performed by calculating the absolute time a signal propagates from an emitter to a sensor as well as a known velocity of the signal. Time synchronization between the emitter and sensor is often a factor but not required to obtain a position [5]. In contrast, TDOA does not utilize synchronization as it calculates the different arrival times at separate sensors from a single emitter [5]. FDOA is centered on the difference in transmitted frequency and received frequency known as a Doppler shift [6].

GPS measurements outside of a purely theoretical environment are heavily impacted by three main components of error. First, time precision is a vital input to TOA and TDOA algorithms in that an offset of only a few seconds can result in errors measured in miles [7]. The main source of time error is located in the sensor, the emitter, or both. Next, the GPS signal is affected by environmental factors such as multi-path arrival, tropospheric noise, and ionosphere noise. Multipath delay is present when the signal propagates off of manmade and natural sources. These structures cause attenuation and delay to the signal before it reaches the sensor and is noted in literature as a dominant source of error [8]. Troposphere conditions vary extensively based on weather, location, time of day, and time of year. Extreme weather formations can render GPS signals unusable. Ionosphere delay is centered on the quantity and fluctuations of electron density. Terrestrial and space events lead to delay effects which severely impacts location accuracy. Obtaining range measurements is based on either the least-square (LS) method or the maximum-likelihood (ML) technique [9]. The LS technique strives to reduce error, while the ML technique attempts to determine the highest probability that an event occurred [10]. Both techniques are used in many engineering applications and often used together to draw out the individual strengths of both algorithms. In order to properly gain reliable ranging information, noise filtering must be applied. Filtering algorithms are split into two categories. Linear systems utilize the Kalman filter (KF), which at regular intervals takes real-time samples and predicted future values and compares them [11].

This is ideal for linear systems that involve movement where obtaining and calculating future positional information would be difficult when handled at high speeds. Non-linear systems use either the unscented Kalman filter (UKF) or the extended Kalman filter (EKF). Both variants of the linear KF are prevalent in geolocation research.

C. RESEARCH GOAL

Previous research determined the likelihood that two airborne sensors could reliably produce accurate geolocation when implemented by fusing multiple time steps [12]. Proof-of-concept was developed using a TOA algorithm. In addition, a combination of TDOA and FDOA was utilized to test the feasibility of the concept. Two separate tests were run comparing emitter location root-mean-square error (RMSE) to angular separation and aperture size. Common problems throughout the testing centered on excessive computational time and high emitter location RMSE that rendered precision geolocation useless. In addition, the TDOA and FDOA technique utilized a bounding box method that also suffered from significant run times that would leave real-time implementation unfeasible. To accomplish the stated goals while keeping the experiment closer to real-world design, a location system utilizing a single frequency band is assumed. This method decreases cost and is the basis for first generation satellite construction. Noise mitigation was handled through the use of a single-point calculation of total electron content (TEC) derived from the Community Coordinated Modeling Center (CCMC). As the satellites or UAVs traveled along their respective paths, noise calculation was held constant based on the calculated sheet of electron density and utilized as the high bound for calculations. Low calculations were based on a value one-tenth of the calculation for the high bound.

In this research, we propose to research the correlation between two and three airborne sensors under the proof-of-concept using TOA angular separation and aperture size tests versus emitter location RMSE. The original formula will only be changed to incorporate the third sensor. All other variables will be held constant to preserve the legitimacy between the two tests. In addition, we propose to research and investigate the effect of the bounding box in the combined TDOA and FDOA calculations to bring about

a more accurate measure of the requirements to maximize this technique. Finally, we propose a research survey of ionosphere noise mitigation techniques for signals operating over a single frequency.

II. TIME-OF-ARRIVAL

A. GOVERNING EQUATION

Simple yet effective methods for determining geolocation led to the development of the TOA measurement. The basic requirement for determining the position requires that the absolute time is known and synchronized for the emitter and the sensor to obtain optimized results. The emitter *e* sends a signal to sensor *s*. The time it takes to propagate from the emitter to the sensor is known as the propagation time. In a two-dimensional plane, the *i*-th sensor has an initial position at $p_{si} = [x_{si}, y_{si}]$, and the emitter's initial position is $p_e = [x_e, y_e]$. The height component of the sensor *z* is set to zero. The distance between the emitter and sensor is determined by

$$d = \| p_e - p_{si} \| = \sqrt{(x_e - x_{si})^2 - (y_e - y_{si})^2}, \quad i = 1,2,...,I \tag{1}$$

which is valid for ideal cases without error in a coordinated group of *I* sensors.[13] The time difference τ_{eS_i} it takes for a signal to propagate from the emitter to the sensor is calculated by

$$TOA_m = \tau_{eS_i} c_o. \tag{2}$$

where c_o is the speed of light. Real-world calculations of the TOA measurement must account for error due to noise. Sources of error vary widely based on type and location. Atmospheric sources include the effects from the troposphere, ionosphere, weather, and space. Deeper analysis of this error reveals that the TOA signal can be affected by absorption, scattering, attenuation, and multi-path effects. These errors are accounted for in the TOA measurement by adding noise error w to the TOA_m given by Equation (2). The modified equation for TOA_m is calculated as

$$TOA_m = (\tau_{eS_i} c_o) + w. \tag{3}$$

The addition of noise errors causes significant geolocation position inaccuracies depending on their presence and intensity.

B. TWO-DIMENSIONAL SOLUTION

The two-dimensional scenario provides the fundamental basis for a high dimensional understanding of the TOA solution as depicted in Figure 1. The single sensor s_1 located at $(-5, 0)$ km attempts to geolocate emitter e located at (1, 7) km, which is initially unknown. In this scenario, the movement of the sensor with respect to the emitter is fixed. This is not a requirement in real-time calculations but is provided for simplicity.

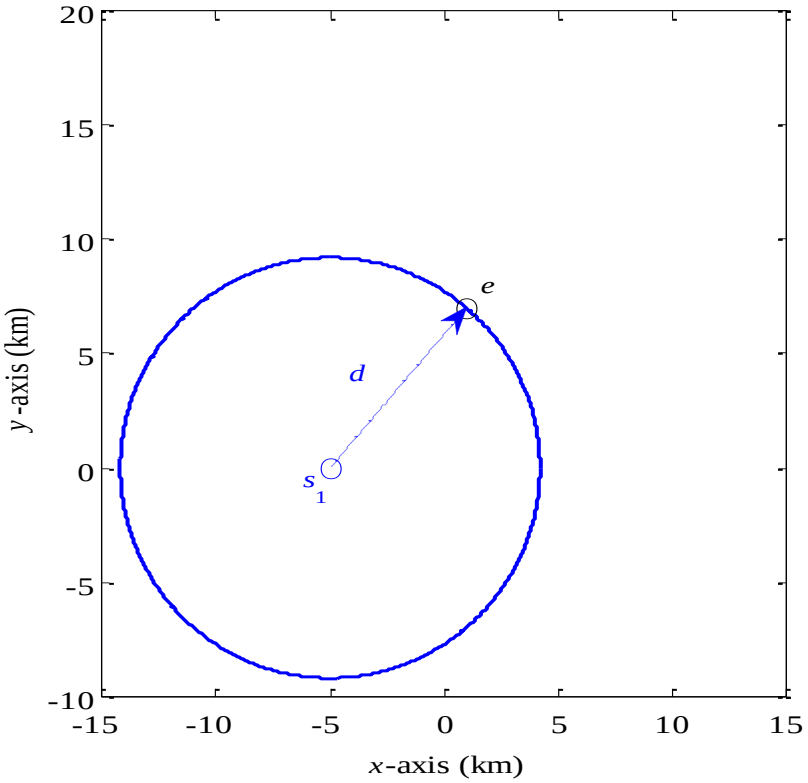

Figure 1. One sensor attempts to geolocate an unknown emitter.

The emitter begins the process by emanating an omni-directional beacon symbol. The signal received by a sensor is processed for its TOA measurement or the radial range to the emitter. The radial range, when swept through an arc of 360 degrees, limits the location of the emitter to all points on the circle centered at s_1 with a range of *d*.

For the three-sensor scenario (I = 3), the sensors' positions and their respective curves as well as the emitter is shown in Figure 2.

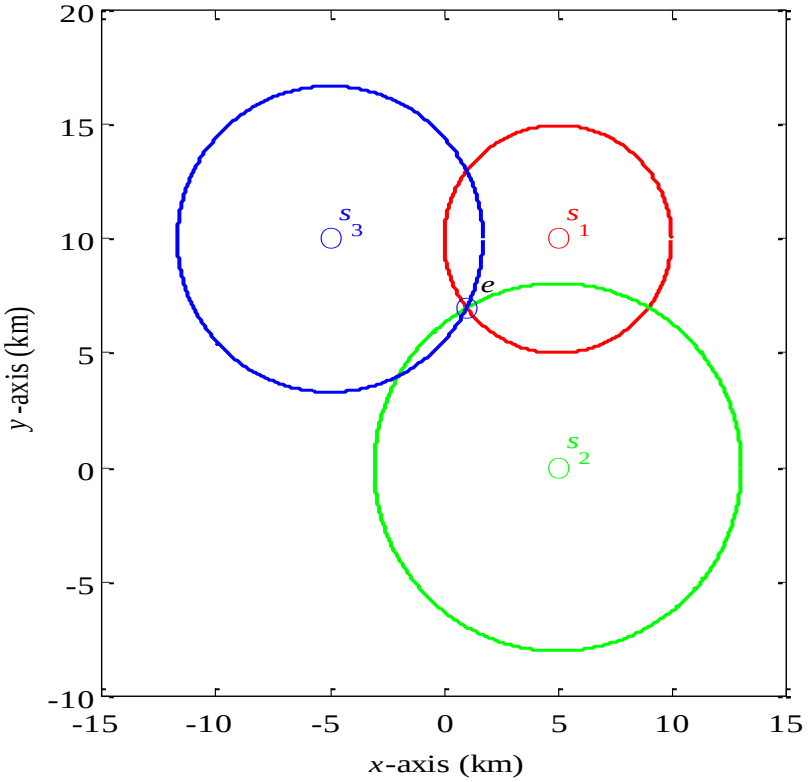

Figure 2. Three sensors geolocate an unknown emitter.

Three sensors without extraneous noise error appear to geolocate the emitter without ambiguity. By taking a closer look at the solution, we see a very small deviation in precision as depicted in Figure 3.

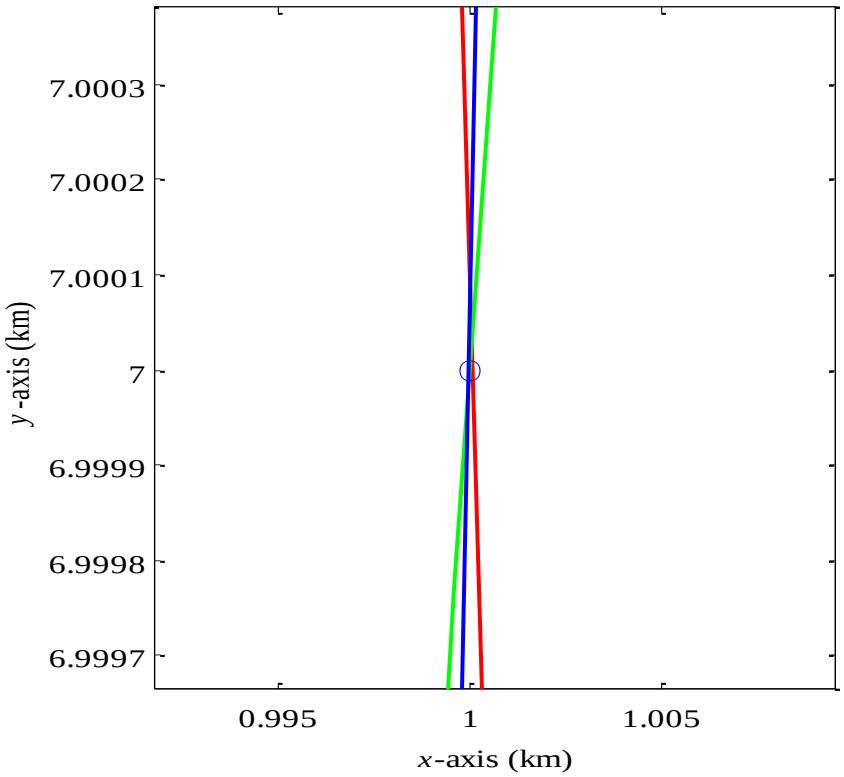

Figure 3. Three sensors obtain an error of 0.1 meters when attempting to geolocate an emitter.

In a perfect environment without noise, error still exists. This fact serves to illustrate that the algorithm can produce a certain amount of error depending on how it is coded. In this scenario, the sensors are only 4 km from the emitter. This accuracy is adequate for many applications involving UAVs; however, in a noise free environment using satellites, the separation is significantly greater. Using the same algorithm, we move the three sensors out to 5,281,680 meters, or the nominal height of an operating GPS satellite, as depicted in Figure 4.

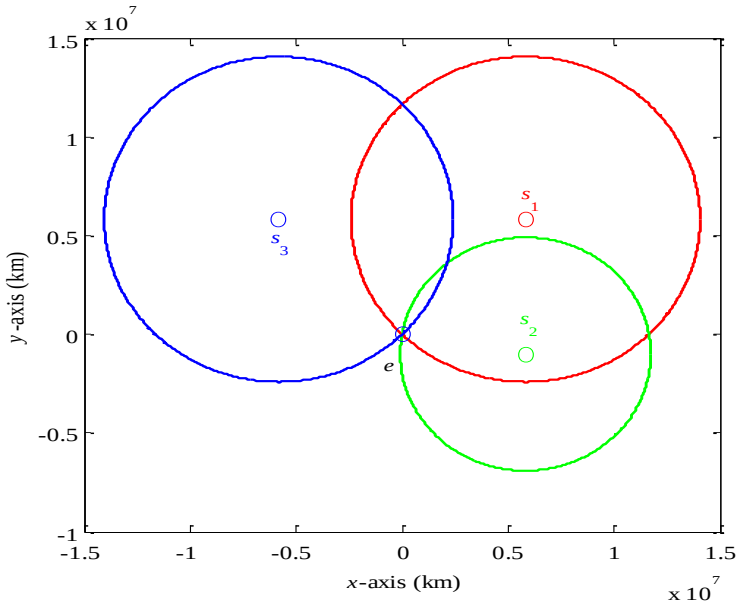

Figure 4. Three satellite sensors geolocate an unknown emitter.

As seen previously, it appears that the three sensors have correctly located the emitter e. Due to the large range being observed, it is imperative to take a closer look at the intersection point of the three spheres as depicted in Figure 5.

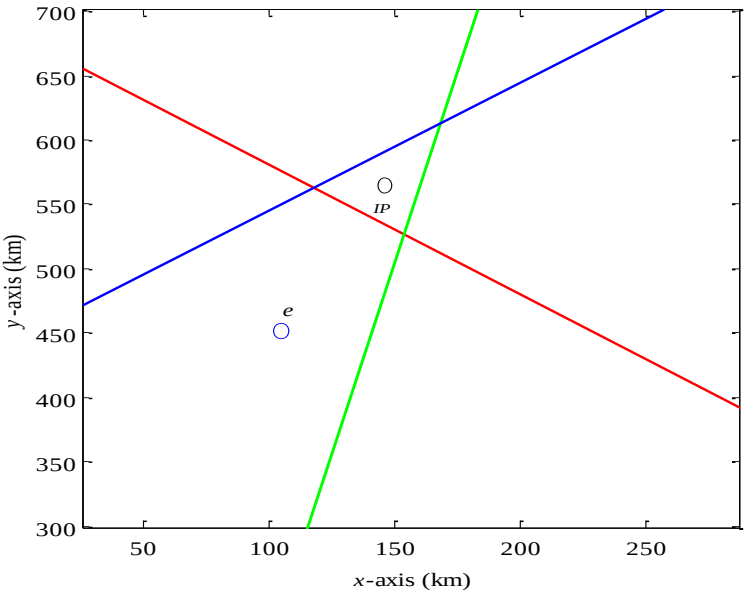

Figure 5. Three satellite sensor error of approximately 110 kilometers when attempting to geolocate an emitter.

The radial curves of the three sensors create a triangle point. The area inside the triangle signifies all of the possible geolocation points where the emitter could be found as well as the error in the algorithm in determining the true emitter's position. An intersection point IP is located within the triangle and denotes the centroid or the average locus of all points in the two dimensional shape. The centroid is the best estimate to the calculated position of the emitter. The error of the algorithm is roughly 110 km or 68 miles using U.S. standard measurement. Clearly, a refined algorithm is a necessary component in geolocation systems.

C. THREE-DIMENSIONAL SOLUTION

Geolocation in three dimensions is the foundation for real world geolocation. Instead of a two-dimensional circle, the beacon from emitter e and the solution to Equation (2) is characterized as a sphere. The sphere is centered on the corresponding sensor with the radius equal to TOA_m. The surface of the TOA sphere represents all of the possible points of the emitter. With three available sensors, it first appears that there are many different intersection points between the spheres as depicted in Figure 6.

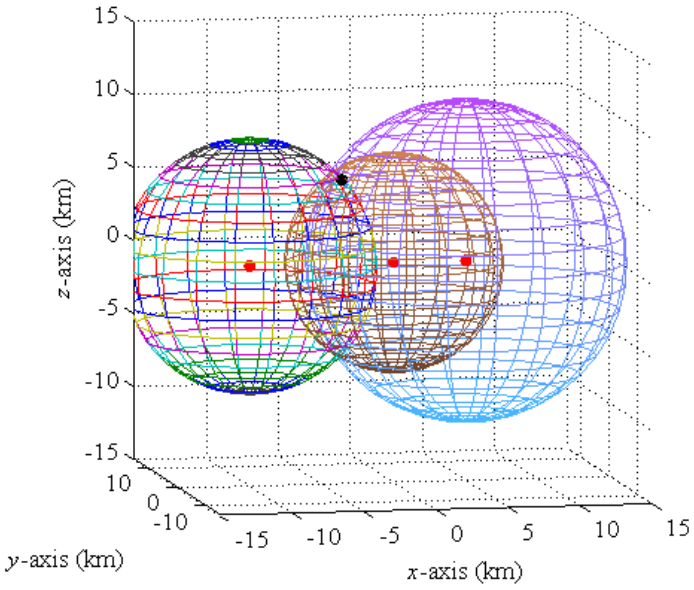

Figure 6. Three-dimensional geolocation of an unknown emitter with three sensors.

The three sensor positions depicted with red dots are located at $(-25,0,0)$, (5,0,0) , and $(0,-35,0)$. The emitter is positioned at $(-4,-2,6)$ and indicated as a black dot. It is visually difficult to determine the intersection points between the spheres. A simple approach to obtain the geolocation solution is view the problem in three steps. The first step takes two spheres and determines the intersection point between them. A second TOA sphere generates a circular arc of intersection points and is represented by a blue radial range circle and possible location of the emitter as depicted in Figure 7.

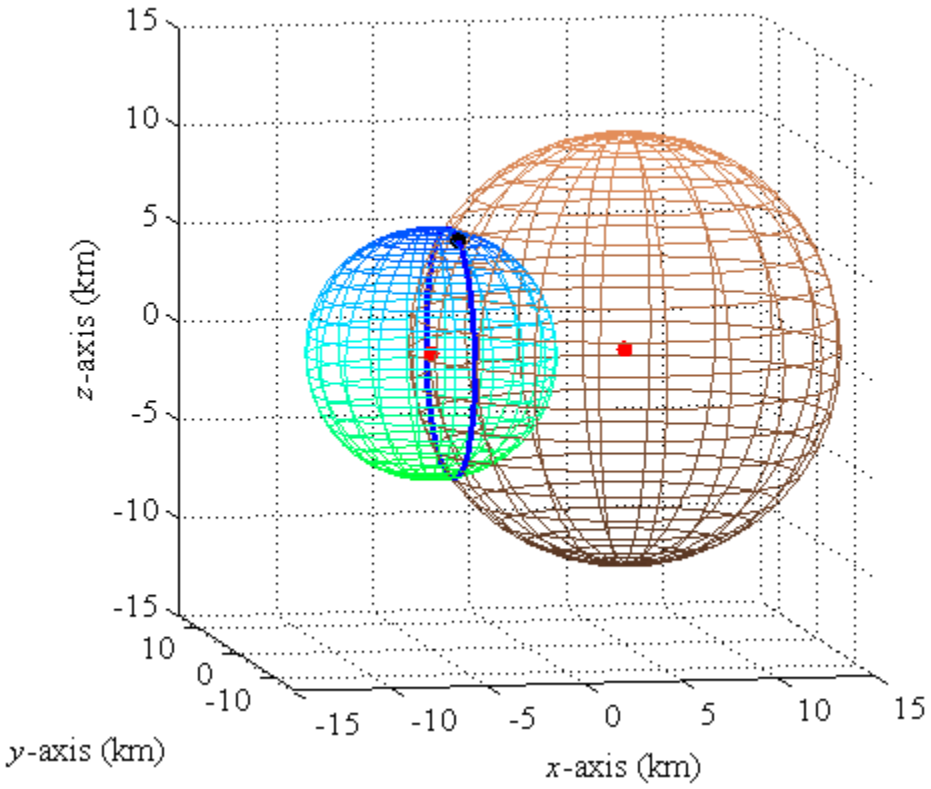

Figure 7. Three-dimensional geolocation of an unknown emitter with two sensors.

The second step incorporates a third sensor into the calculation creating another sphere. This third sphere will have multiple intersection points with the radial range circle determined in step one and is depicted in Figure 8.

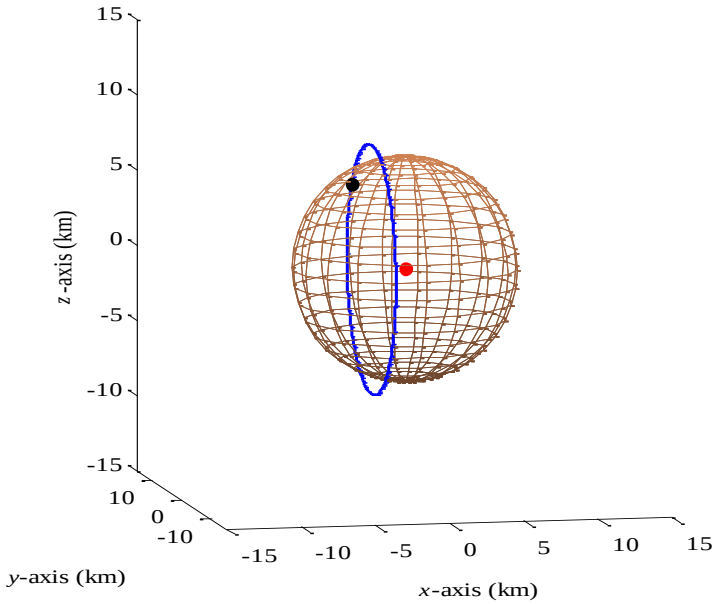

Figure 8. A third sensor's three-dimensional geolocation intersects a radial range circle.

The corresponding set of points that intersect the sphere and the radial range circle determined in step two create a new red radial range circle as depicted in Figure 9.

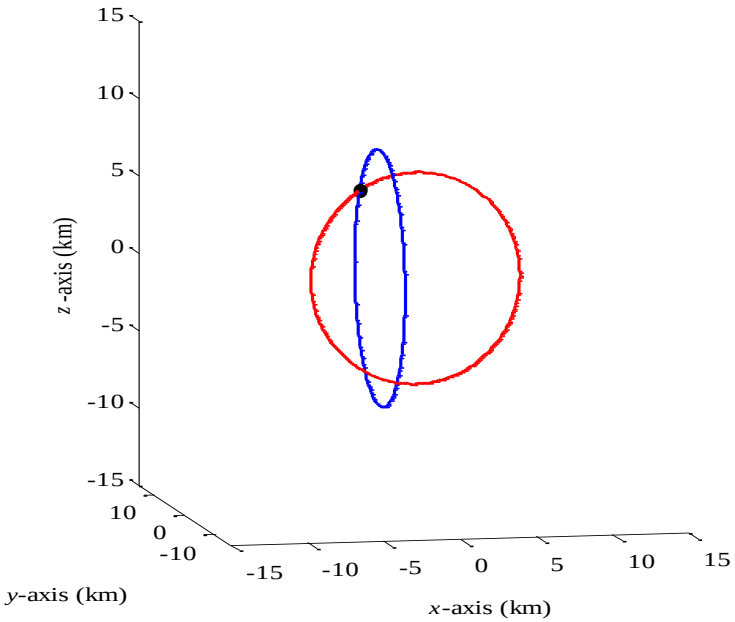

Figure 9. Two radial range circles intersect in two dimensions.

The final step is to determine the intersecting point of the two radial range circles. Two points of intersection remain between the red and blue radial range circles. Adding a fourth satellite is required to determine which point is valid. Both radial range circles are orientated perpendicular to the axis of orientation of the respective sensors. This positioning always occurs under these conditions. Furthermore, the determination of the two-dimensional and three-dimensional scenarios balances between the number of dimensions and the number of sensors. An ideal two-dimensional situation has two sensors to solve the calculations successfully. In the case of only one sensor, the system is termed underdetermined. Three sensors in a two-dimensional system is termed overdetermined and leads to better positional accuracy. The same methodology applies to three dimensions.

THIS PAGE INTENTIONALLY LEFT BLANK

III. TIME-DIFFERENCE-OF-ARRIVAL

A. GOVERNING EQUATION

An emitter beacons a signal, and the signal is received by two or more sensors. Time-difference-of-arrival is determined at the time when the signal is received. The time utilized for calculations can be based in absolute time, as in the case of TOA, or can be determined from relative time. Despite the freedom that TDOA creates, satellites still retain strict control on time to minimize error within the entire system. In a two-dimensional scenario, the difference of the distances between the sensors and the emitter is determined by

$$d = \sqrt{(x_e - x_{si})^2 - (y_e - y_{si})^2} - \sqrt{(x_e - x_{sj})^2 - (y_e - y_{sj})^2},\ i = 1,2,...,I,\ \text{j} = 1,2,...,\text{J} \quad (5)$$

where two separate sensors si and sj in two networks of sensors I and J receive the signal from the emitter e. The TDOA equation depicted by

$$TDOA_m = (\tau_i - \tau_j)c_o \quad (6)$$

where τ_i and τ_j are the relative time components of the received signal from separate satellites si and sj. The $TDOA_m$ value can also be calculated based on absolute time determined by

$$TDOA_m = ((\tau_i - \tau_o) - (\tau_j - \tau_o))c_o \quad (7)$$

where τ_o is the reference time set from the moment the emitter beacon emanates the signal. The TDOA geometry created by Equation (5) is a hyperbola in two dimensions and a hyperboloid of two sheets in three dimensions [14]. The location of the emitter e can be found on any point of the respective shape. Two sensors are the foci of the hyperbola or hyperboloid. In addition, there is a fixed distance from any point on the hyperbola to the difference in distances to the foci [15].

B. TWO-DIMENSIONAL SOLUTION

The basic representation for the two-dimensional TDOA calculation from Equation (6) is depicted in Figure 10, where sensors *si* and *sj* are the foci of the respective hyperbolas located at $(-2,0)$ and (2, 0) km while the emitter *e* is located at (2.05, 1.79) km.

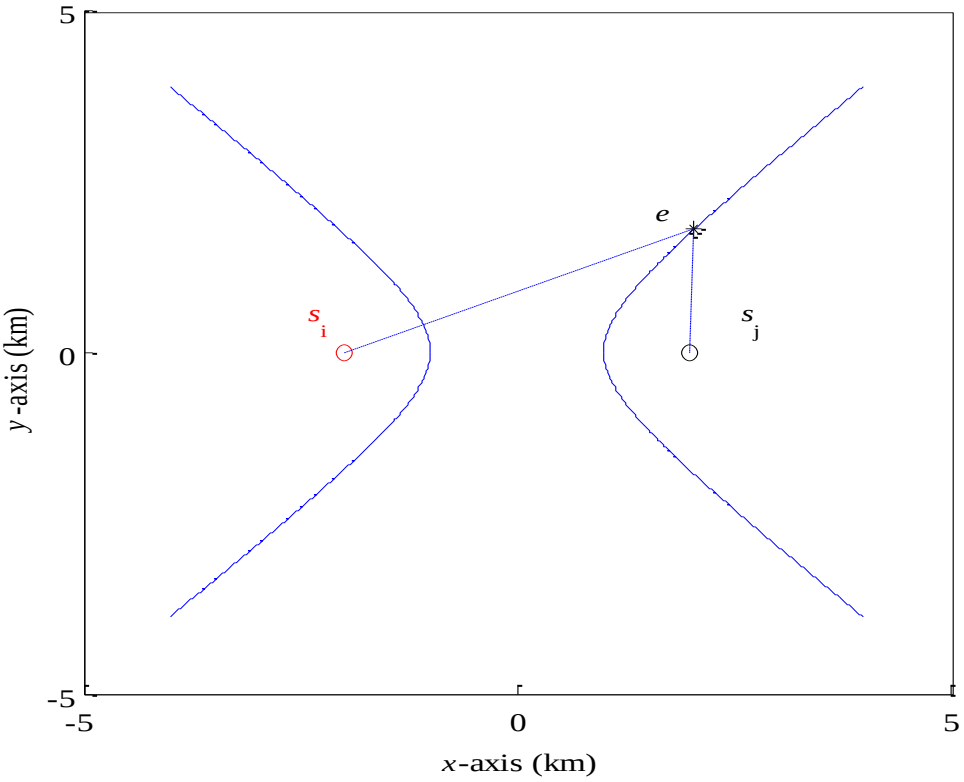

Figure 10. A two-dimensional TDOA solution locates an emitter.

The hyperbola definition states that the difference in distance from any point on either hyperbola to the foci will always be constant [16]. Mathematically this is calculated by

$$|d1-d2|=2a \tag{7}$$

where $d1$ and $d2$ are the distances from the foci to the emitter and $2a$ is two times the distance from the center to a single vertices. With respect to the TDOA parameters of Equation (5), $|d1-d2|$ is calculated by

$$\sqrt{(x_e - x_{si})^2 - (y_e - y_{si})^2} - \sqrt{(x_e - x_{sj})^2 - (y_e - y_{sj})^2} = 2a \tag{8}$$

where sensors *si* and *sj* are located on the *x*-plane of the Cartesian coordinates system. The *x* components x_{si} and x_{sj} are designated g and $-g$ in turn for simplicity while y_{si} and y_{sj} are set to zero. Rearranging terms in Equation (8) yields

$$\sqrt{(x+g)^2 + (y-0)^2} = 2a + \sqrt{(x-g)^2 + (y-0)^2}. \tag{9}$$

After expanding Equation (9) and collecting like terms, we express the resulting form as

$$-4a^2 + 4gx = 4a\sqrt{(x-g)^2 + y^2}. \tag{10}$$

Next, we simplify Equation (10) and square both sides. After simplifying the calculation, we obtain from Equation (10)

$$g^2x^2 - 2a^2gx + a^4 = a^2x^2 - 2a^2gx + a^2g^2 + a^2y^2. \tag{11}$$

Simplifying once again provides

$$x^2\left(g^2 - a^2\right) - a^2\left(g^2 - a^2\right) = a^2y^2. \tag{12}$$

Subsequently, we introduce the hyperbolic parameter

$$b = \sqrt{c^2 - a^2}. \tag{13}$$

Substituting *g* for *c* as in Equation (9), we can express Equation (13) as

$$b = \sqrt{g^2 - a^2}. \tag{14}$$

Substituting Equation (14) into Equation (12) gives

$$b^2x^2 - a^2b^2 = a^2y^2. \tag{15}$$

Rearranging Equation (15) results in the customary form of a hyperbola given as

$$\frac{x^2}{a^2} - \frac{y^2}{b^2} = 1 \tag{16}$$

provided that the sensors s_i and s_j are located along the *x*-axis. From the basis of Equation (16), the TDOA curve involving two sensors is depicted in Figure 11.

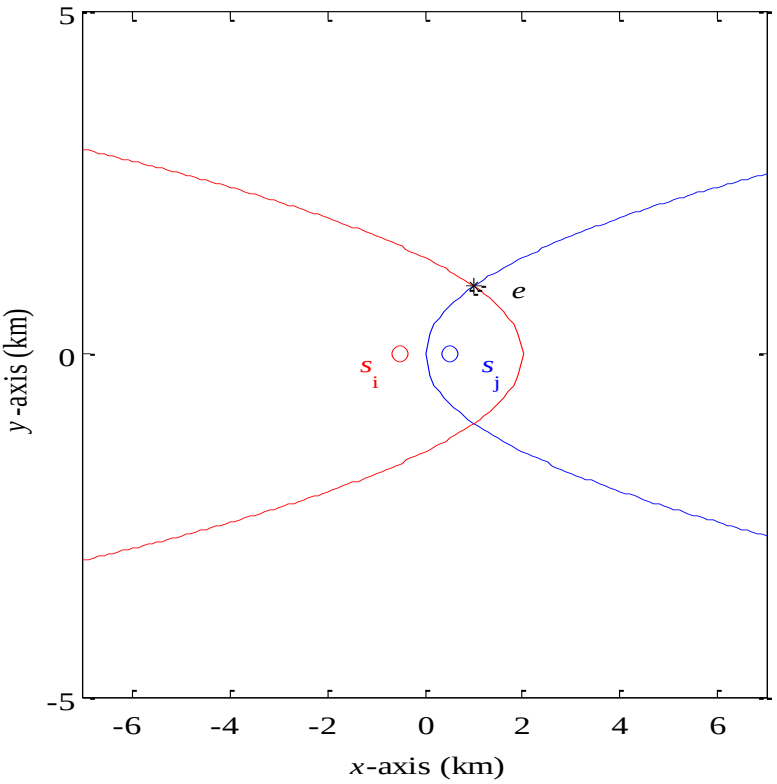

Figure 11. The two sensor TDOA geometry locates a known emitter.

In TDOA geometry, an emitter may be located anywhere on the surface of either hyperbola for a single sensor. The sign of the corresponding TDOA measurement dictates which hyperbola will be kept and which one will be discarded [17]. The intersection between the red and blue hyperbolae, from sensors *si* and *sj* located at $(-2,0)$ and (2, 0), respectively, details the crossing point and locates the emitter at position (2.05, 1.79) as depicted by the black star providing a priori information about the emitter is known. Without a priori information about the emitter's location, a third sensor *sk* is required to remove the ambiguity as depicted in Figure 12.

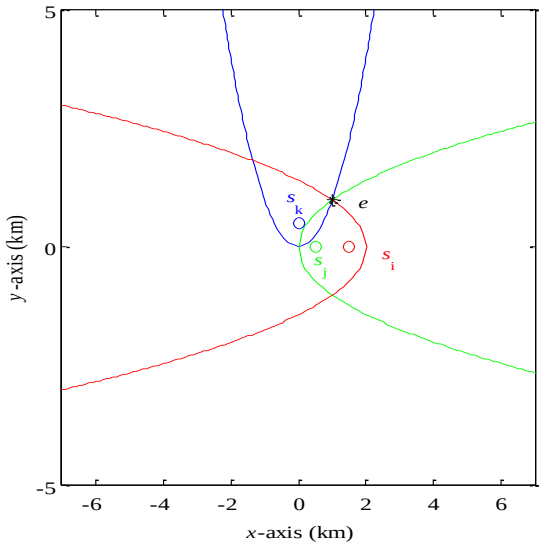

Figure 12. The three sensor TDOA geometry locates a known emitter.

The addition of the third sensor *sk* at positon (0, 0.5) resolves the location ambiguity of the sensor as denoted by the crossing at emitter *e*. Additional sensors added to the scenario further refine the emitter location and reduce ambiguity that may be present due to inherent algorithm inconsistencies in calculating the position as represented in Figure 13.

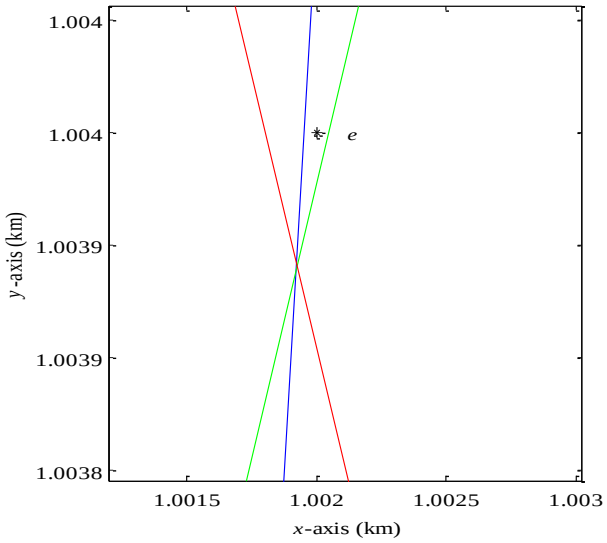

Figure 13. The three sensor TDOA geolocation results in a position error.

The error present in the utilized TDOA geolocation of the emitter is 1.0 m. Real world application of this concept is important in military applications. The military equivalent of this scenario provides practical application to the implications of the algorithm error. Sensors si, sj and sk can be viewed as three UAVs patrolling the battlefield. Emitter e is the enemy that is targeted. From the results described in Figure 13, there is no problem putting large munitions on the target; however, if the target is to be neutralized by a sniper, the error in the algorithm could provide faulty data resulting in a failure to accomplish the mission.

C. THREE-DIMENSIONAL SOLUTION

A third dimension expands the TDOA solution resulting in a hyperboloid of two sheets. The mathematical equation is given by

$$\frac{x^2}{a^2}+\frac{y^2}{b^2}+\frac{z^2}{b^2}=1 \tag{17}$$

where the hyperboloid is orientated along the *x*-axis [18]. Shifting the a^2 term to be positioned under the y^2 or z^2 term is analogous with shifting the orientation in the respective direction.

A single sensor produces a hyperboloid of two sheets as depicted in Figure 14. As in the case of the two-dimensional TDOA measurement, only one of the sheets will be valid.

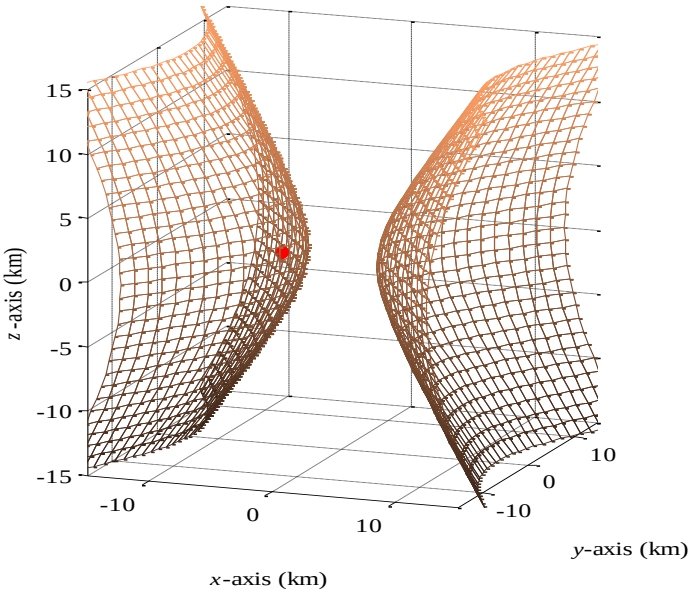

Figure 14. Three-dimensional TDOA measurement with one sensor.

We advance this concept with an illustration of a two sensor TDOA geolocation of an unknown emitter in Figure 15. The red dots signify sensors si and sj located at $(-5,0,0)$ and $(5,0,0)$, respectively. Emitter e is depicted by the black dot located at $(-1.4,-3.7,.9)$.

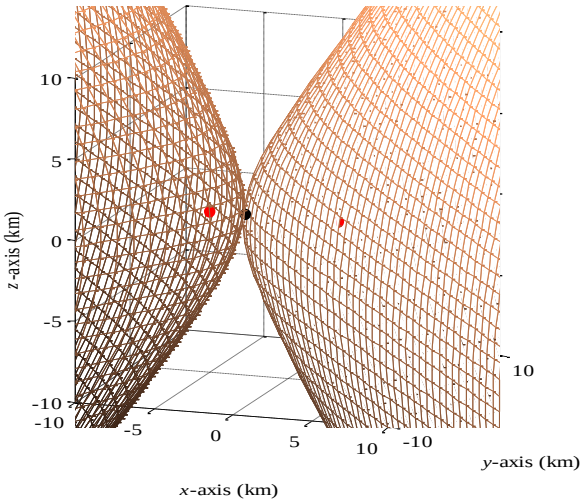

Figure 15. Three-dimensional TDOA measurement with two sensors.

The introduction of noise into the calculation will cause uncertainty in the precision of the geolocation. Furthermore, an emitter located higher or lower on the hyperboloid will cause an ambiguous solution to become present in the same manner as the two-dimensional calculation. In this environment, refinement is made through the use of additional TDOA measurements from additional sensors. Adding a third or fourth sensor will further remove the ambiguity and provide increased accuracy.

IV. FREQUENCY-DIFFERENCE-OF-ARRIVAL

A. GOVERNING EQUATION

An emitter sends a beacon signal that is received by two or more airborne sensors. Natural and man-made interferences interact with the beacon causing unique delays before the signal reaches each of the sensors. The frequency difference between the received signals is processed, and the resulting geolocation is sent back to the ground station [6]. The principle of Doppler states that sound changes with movement. Given that we have two objects and one is at rest while the other is in motion while making noise, the received frequency sensed by the stationary object is different depending on the direction and speed of movement. When the moving object is traveling away from the stationary object, the frequency goes down and vice versa for when the moving object is moving toward the stationary object. The frequency of a signal at the moment it leaves the transmitter is known as the base frequency and is denoted by f_o. The Doppler change in frequency respective of motion is noted as Δf. The basic frequency-difference-of-arrival (FDOA) equation derivation is attempted by way of [17]. The general equation is calculated through the following scenario. Two sensors s_i and s_j move in respective velocities v_{s1} and v_{s2} along a prepositioned axis around the Earth. Emitter e beacons an omnidirectional signal f_o requesting locational data at the initial time τ_0. The signal is received by the two sensors and measured as the Doppler difference by

$$\Delta f_{sisj} = (\Delta f_{si} + f_o) - (\Delta f_{sj} + f_o) = \Delta f_{si} - \Delta f_{sj} \tag{18}$$

where Δf_{si} and Δf_{sj} are the Doppler change in frequencies for sensors s_i and s_j while f_o is the base frequency. This difference is related to the relative transmitter velocity which is calculated by

$$\Delta f_{sisj} = \frac{f_o}{c_o}(v_e) \tag{19}$$

where c_o is the speed of light and v_e is the relative emitter velocity. The parameters from Equation 7 can be rewritten in terms of the delay and is evaluated by

$$TDOA_d = \frac{\| S_j(t) - e(t) \| - \| S_i(t) - e(t) \|}{c_o} \tag{20}$$

where $S_i(t)$, $S_j(t)$, and $e(t)$ are the positions of sensor one, sensor two and the emitter with respect to time. In conjunction with the time-difference delay, the frequency-difference delay is rendered by

$$FDOA_d = \frac{f_o}{c_o}\left[\frac{S_j(t) - e(t)}{\| S_j(t) - e(t) \|}\left(v_{s2}(t) - v_e(t)\right) - \frac{S_i(t) - e(t)}{\| S_i(t) - e(t) \|}\left(v_{s1}(t) - v_e(t)\right)\right] \tag{21}$$

where $v_{s1}(t)$ and $v_{s2}(t)$ are the velocities of sensor one and sensor two with respect to time.

B. TWO-DIMENSIONAL EQUATION

The basic two sensors scenario is depicted in Figure 16. Sensors s_i and s_j are moving in the plane of the sensor axis at velocities $v1$ and $v2$ while d_{e1} and d_{e2} represent the respective distances from the emitter to each sensor.

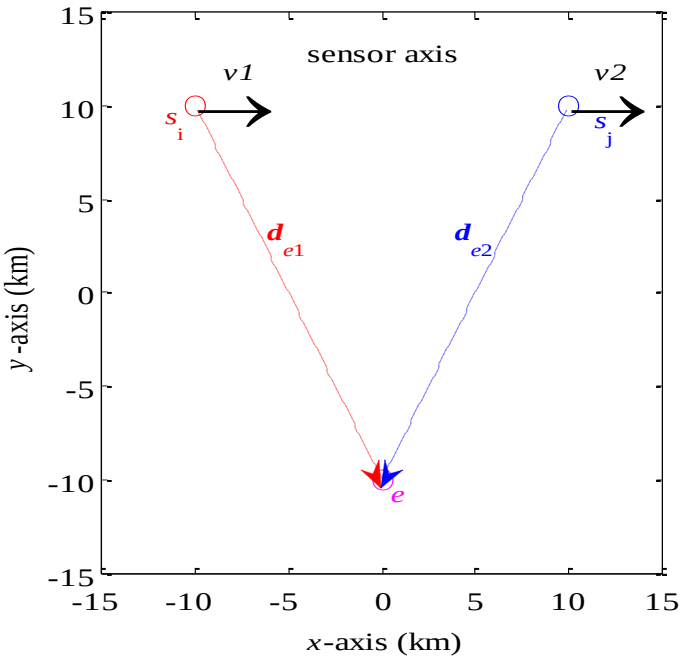

Figure 16. Two-dimensional FDOA measurement with two sensors.

The FDOA solution for two airborne sensors is depicted in Figure 17. Sensors s_i and s_j move along the sensor axis at a constant velocity, which creates a closed curve perpendicular to the axis that intersects the stationary emitter's position. A nearly identical curve is created that will intersect the emitter providing that it remains stationary when the speed of the sensors in the direction of the axis or the frequency of the signal changes; however, changes in environmental conditions can cause multipath scattering that have a significant effect on accuracy [18].

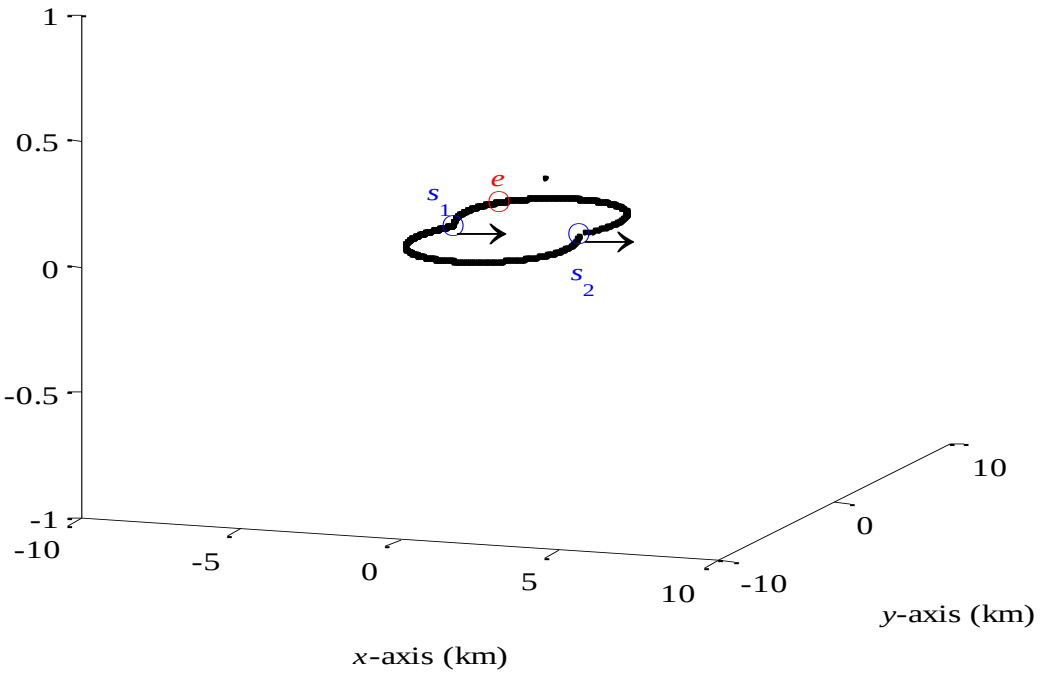

Figure 17. Two sensors with constant velocity attempt to geolocate an emitter using FDOA measurements along a search axis.

Changing the relative motion of the sensor with respect to the emitter affects the accuracy of the geolocation. As depicted in Figure 18, sensors s_i and s_j are moving along the *y*-axis with a constant velocity at a right angle to the sensor axis. The difference in this shift, away from the sensor axis, results in a nonlinear state in the FDOA curve.

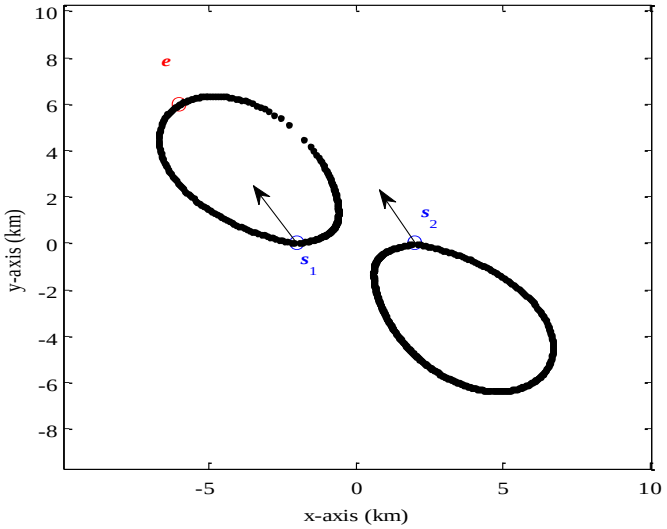

Figure 18. Two sensors with constant velocity attempt to geolocate a stationary emitter at a right angle to the sensor axis.

Under closer inspection, if the emitter was positioned between $(-1.8, 3.3)$ and $(-2.2, 3.7)$ on the curve, it would not have been located as depicted in Figure 19.

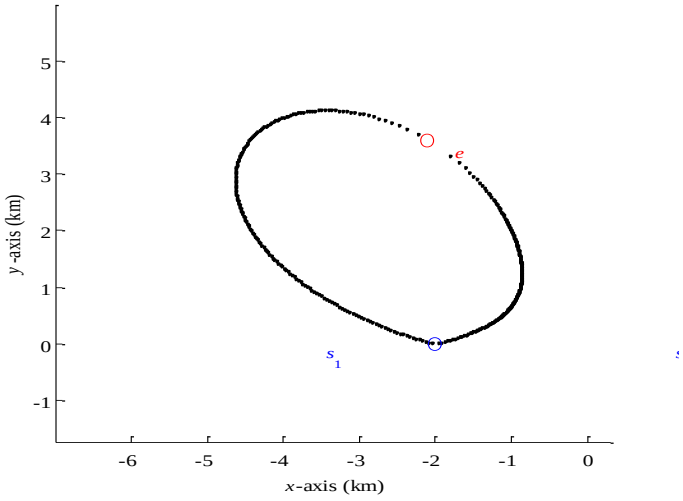

Figure 19. FDOA failed geolocation of a stationary emitter.

However, geolocation of the emitter is possible. By utilizing a combination of TDOA and FDOA calculations, the emitter is successfully located by the sensors as depicted in Figure 20.

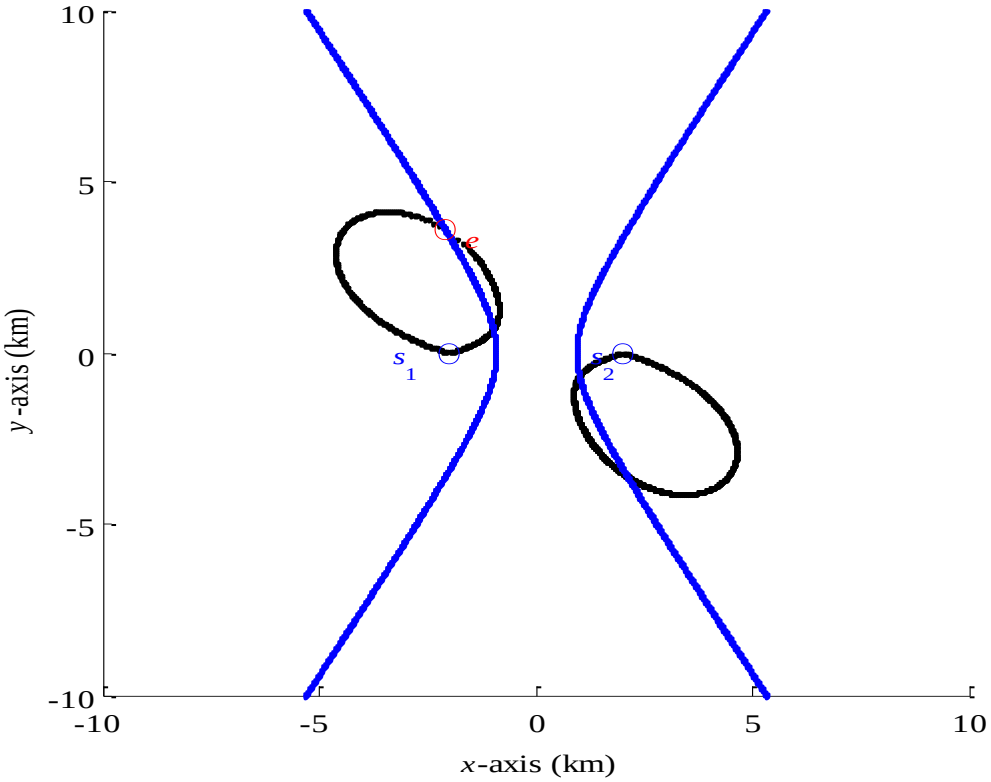

Figure 20. Two sensors successfully locate an unknown emitter through TDOA/FDOA fusion.

A closer inspection of the geometry reveals a matching response to Cassini's ovals. The basic Cassini Oval equation derivation is attempted by way of [19]. The basic understanding of the equation states that the sum of all points between an emitter and two sensors $(s_i,0)$ and $(s_j,0)$ have a constant product p^2 providing that the sensors are equidistant from a central point. Through the manipulation of Equation (5), the distance from emitter e to sensor S_i is depicted by

$$d_{esi} = \left(\sqrt{(x_e - x_{si})^2 - (y_e - y_{si})^2}\right). \quad (22)$$

Furthermore, the distance from emitter e to sensor S_j is depicted by

$$d_{esj} = \left(\sqrt{(x_e - x_{sj})^2 - (y_e - y_{sj})^2}\right). \quad (23)$$

The Cassini Oval equation combines Equations 22 and 23 to be given by

$$(d_{esi})(d_{esj}) = p^2. \quad (24)$$

Since S_i and S_j are equidistant from a central point between them, it is more succinct to designate a single term S to represent this relationship. Through the conversion to Cartesian coordinates, the quadratic polynomial equation is calculated by

$$[(x+S)^2 + y^2][(x-S)^2 + y^2] = p^4. \quad (25)$$

The ratio of S/p determines the shape of the FDOA curve as the angle between the emitter and sensors changes. When the ratio falls between $\sqrt{2}/2$ and 1, the shape of the curve resembles Figure 17. In contrast, a ratio of $S/p > 1$ resembles the shape of Figure 18. While the Cassini Oval aids in the understanding of the geometric properties, it does not provide a detailed analysis of the non-linearity found in the FDOA calculation. Furthermore, detailed analysis outside the scope of this thesis is required to locate and possibly remove this occurrence.

V. NOISE CONSIDERATIONS

A. SOURCES

Noise is defined as any unwanted frequency occurrence that interferes with the intended transmitted signal. It is imperative that these sources are identified and removed to preserve the quality of the signal to the greatest extent possible. While consistent narrowband sources are more easily eliminated through filtering, other noise sources such as non-stationary, impulsive, and white noise require more difficult removal techniques [20]. Noise interference is a major factor that affects geolocation precision. The main sources of noise that are applicable to GPS are man-made and environmental. Man-made sources include noise generated by other devices operating near the same frequency band as GPS, emanations in the electromagnetic spectrum, system and antenna noise, as well as high power radio-frequency operation in the vicinity of the GPS receiver [21]. In addition, many man-made sources are located in urban areas comprised of tall buildings and various intrusive structures. This intensifies the noise problem as non-line-of-sight (NLOS) conditions increase the signal degradation and range errors through multi path interference. Environmental noise includes factors such as electron density, space disturbances, and weather conditions. The combination of these sources creates significant geolocation error for airborne sensors. More specifically, the noise in the troposphere directly effects UAV precision while ionosphere fluctuations have a similar negative impact on satellites.

B. IMPACT OF NOISE FACTORS

The atmosphere contains different regions based on elevation from the Earth's surface as shown in Figure 21. The lower red band is the troposphere region and extends upwards through the Stratosphere and beyond.

Figure 21. Earth's atmosphere layers viewed from the International Space Station, from [22].

Three main regions have quantifiable impacts on geolocation operations. First, the Troposphere region is important to GPS due to the increased role that UAVs play in these operations. This region extends from the Earth's surface to a region between eight and seventeen kilometers. It contains the majority of weather patterns and is variable based on location, time of day, and time of year. Next, above the Stratosphere and Mesosphere, the Ionosphere region encompasses distances from roughly fifty kilometers to one thousand kilometers and varies based on time of day and location. Additionally, the Ionosphere is divided into three regions. The highest region F is present during the day as well as the night. The next lower region E is also present during the day but weakens during the night. The lowest region D is present during the daytime but disappears during the night. Ionization in this region occurs through solar radiation during the day and space radiation at night. The radiation referred to as photons break apart atoms freeing electrons into the atmosphere. In turn, these free electrons interfere with radio frequencies at varying

degrees depending on the frequency of the signal and the density of the electrons [23]. The effects from electron disturbances heavily affect the precision of geolocation. Finally, the Exosphere varies in range above the Thermosphere between roughly one thousand kilometers to upwards of ten thousand kilometers. The upper bound of the Exosphere determines the limit between the Earth's atmosphere and interplanetary space. All GPS satellites including the United States Global Positioning System, Russian's Globalnaya Navigatsionnaya Sputnikovaya Sistema or Global Navigation Satellite System (GLONASS), the European Union Galileo system, as well as the Chinese Beidou Navigation Satellite System (BDS) operates in this region.

1. Noise Factors Affecting the Troposphere

The troposphere presents two major delays that affect geolocation signals. The first is a "dry delay" also known in literature as a hydrostatic delay. The majority of these delays are due to dry gases located in the upper region of the troposphere. It is important to note that it is not a completely dry region and water vapor is present; however, the volume of water vapor is not as large as the lower troposphere. At lower altitudes in the troposphere, water vapor is more prominent and a second delay is noted as the "wet delay" [24]. Geolocation operations in the troposphere are most directly affected by the temperature, pressure, and water vapor found in this region. These factors and their refractivity cause the sound wave of the signal to bend causing delays that affect the precision of location [25]. The basic derivations of noise delay in the troposphere are attempted by way of [26]. A signal traveling from the emitter to the sensor undergoes a hydrostatic delay, a wet delay, and an elevation angle delay. These three delays must be removed in order to accurately determine the delay only for the signal. First, we define the refractive path delay. The actual distance from the emitter to the sensor vice the ray path distance is depicted by

$$SPDN_{eS_i} = \int_{RP} IAR(s)\, ds - \int_{VRP} ds \tag{26}$$

where $SPDN_{eS_i}$ is the neutral slant path from the emitter e to the sensor S_i, RP is the ray path that travels from the emitter to the sensor, $IAR(s)$ is the index of atmospheric

refraction as a function of the slant path, and *VRP* is the virtual ray path from the emitter to the sensor in a vacuum.

Next we calculate the hydrostatic and water vapor delays. The neutral slant path is further broken down into two components as given by

$$SPDN_{eS_i} = SPDN_{eS_i[HYD]} + SPDN_{eS_i[WET]} \tag{27}$$

where $SPDN_{eS_i[HYD]}$ is the "dry delay" and $SPDN_{eS_i[WET]}$ is the wet delay. The total path between the emitter and the sensor contains symmetric and asymmetric components based on the refractivity of the environment to which the signal is propagated. This understanding allows Equation (27) to be given by

$$SPDN_{eS_i} = SPDN_{eS_i[HYDSYM]} + SPDN_{eS_i[WETSYM]} + SPDN_{eS_i[HYDASYM]} + SPDN_{eS_i[WETASYM]} \tag{28}$$

where $SPDN_{eS_i[HYDSYM]}$ and $SPDN_{eS_i[WETSYM]}$ are the symmetric components and $SPDN_{eS_i[HYDASYM]}$ and $SPDN_{eS_i[WETASYM]}$ are the asymmetric components. In order to extract the wet delay, the hydrostatic delay must be first removed through highly accurate measurements [27]. The simplified neutral delay from the gradient maps is depicted by

$$SPDN_{eS_i} = m(\mathrm{d}_e^{Si})_{[\mathrm{HYD}]} ZHD_e + m(\mathrm{d}_e^{Si})_{[WET]} ZWD_e + m(\mathrm{d}_e^{Si})_{[\mathrm{eZ}]} [G_{e[N]} \cos\alpha_e^{Si} + G_{e[E]} \sin\alpha_e^{Si}] \tag{29}$$

where $m(\mathrm{d}_e^{Si})$ is the mapping function, ZHD is the zenith hydrostatic delay, ZWD is the zenith wet delay, $G_{e[N]}$ is the gradient in the north direction with respect to the true north, and $G_{e[E]}$ is the gradient in the east direction with respect to true north The northern and eastern measurements are taken into account for gradients along the latitude and longitude lines, respectively. The Zenith hydrostatic delay, ZHD, is calculated by integrating the hydrostatic refractivity H_R through the space between the emitter and sensor in the troposphere region; it is illustrated as follows

$$ZHD = 10^6 \int_{h_e}^{\infty} H_R \ \mathrm{dh} \tag{30}$$

where h_e is the height of the emitter. Water vapor refractivity is given by

$$W_R = r_2 \frac{pwvp}{T_K} Z_{wet}^{-1} + r_3 \frac{pwvp}{T_K^2} Z_{wet}^{-1} \tag{31}$$

where $pwvp$ is the partial water vapor pressure, r_2 and r_3 are refraction constants, and T_K is the temperature in Kelvin. The Zenith wet delay, ZWD, is calculated by integrating the wet refractivity W_R through the space between the emitter and sensor in the troposphere region; it is illustrated as follows

$$ZWD = 10^6 \int_{h_e}^{\infty} W_R \, dh \,. \tag{32}$$

While hydrostatic, wet and zenith delays comprise the majority of delay on a geolocation signal, other natural phenomenon such as sandstorms and volcanic ash, as well as scattering from rain, hail, and snow also contribute to the delay [28].

2. Noise Factors Affecting the Ionosphere

The ionosphere region is aptly named for the location where atoms are ionized or broken apart by energy from space or from electromagnetic sources. When the atom is split apart, free electrons are dispersed into the surrounding atmosphere. The amount of electron density in a region through which a geolocation signal travels creates a delay. The basic derivations of electron density in the ionosphere are attempted by way of [29] and [30]. Absorption in the ionosphere is different based on location and altitude. Energy loss is calculated as a combination of the electron density present and the amount of received energy from space. The depth of the atmosphere to a known height h is given by

$$d = \sec(\chi)\left(\int_{\infty}^{h} A_{cs} N_{am} \, dh\right) \tag{33}$$

where A_{cs} is the cross-section absorption amount, N_{am} is the number of atoms that are currently absorbing energy and $\sec(\chi)$ is the angle between a zenith equal to zero and the elevation of the sensor. The strength of the energy at height h is given by

$$E_s = Le^{-h\sec(\chi)} \tag{34}$$

where L is the light intensity from space and $e^{-h\sec(\chi)}$ is the exponential density variation at a constant height h. When Equation (34) is evaluated in conjunction with the cross-section absorption and the number of atoms absorbing energy along the path from the emitter to the sensor through the ionosphere, the resulting energy loss equation is determined by

$$E_l = LA_{cs} N_{am} e^{-h\sec(\chi)}. \tag{35}$$

Molecules in the ionosphere are constantly striving for balance. Atoms search to regain neutrality when electrons break free. The production of energy is given by

$$E_p = \mathrm{I}_{max}\, e^{(1-h'-\sec(\chi)\mathrm{e}^{-\mathrm{h}'})} \tag{36}$$

where $\mathrm{I}_{\max}$ is the maximum amount of ion production and h' is the reference height. Subtracting Equations (35) from (36) results in the general formula for electron density N_e given by

$$\mathrm{N}_\mathrm{e} = E_p - E_l. \tag{37}$$

When the electron density is integrated along the signal's path from the lower bound of the ionosphere to the upped bound, it is referred to as the total electron content and is given by

$$TEC = \int_h^\infty E_l - E_p. \tag{38}$$

In terms of geolocation, the TEC formula is broken down into slant TEC, which designates a straight line between the emitter and sensor, as well as vertical TEC where the ionosphere due to its complex nature and various regions is represented by a thin shell and is measured via a mapping function and the pierce point of the slant TEC [31]. The TEC for a single frequency sensor is calculated by way of [31]. Slant TEC is given by

$$TEC_S = 40.3\frac{N_e}{f} \tag{39}$$

where f is the single frequency of the geolocation center, which is set at 1575.42 MHz for the L1 band of single frequency geolocation satellites. The combination of Equation (39) and a mapping function results in the vertical TEC given by

$$TEC_V = M(\mathrm{S}_{\mathrm{i}\alpha})TEC_S \tag{40}$$

where $M(\mathrm{S}_{\mathrm{i}\alpha})$ is the mapping function with respect to the elevation angle $\mathrm{S}_{\mathrm{i}\alpha}$ of the sensor and is given by

$$M(\mathrm{S}_{\mathrm{i}\alpha}) = \left[1 - \left(\frac{\cos(\mathrm{S}_{\mathrm{i}\alpha})}{1 + \frac{s_h}{E_r}} \right)^2 \right]^{(1/2)} \tag{41}$$

where s_h is the height of the modeled ionosphere shell and E_r is the radius of the Earth.

C. NOISE MODELS

Accurately modeling the atmosphere for time-sensitive operations is a statistically and mathematically complex endeavor. Simplicity versus accuracy is the trade off in noise model generation. Basic theoretical models often leave out higher order statistics due to complexity leaving lower precision that the sensor requires [32]; however, they retain a general overview of predicted results through the utilization of a generic distribution. In carrying forward the work given by [12], a simple exponential distribution allows a basic overview of algorithm capability; however, the full mitigation of delay requires a more robust integration of higher order statistics.

1. TOA Noise Model

Utilization of the exponential distribution in time-of-arrival calculations contains the following advantages. First, the distribution is linked to the Poisson process but contains a memoryless property [33]. In relation to geolocation, noise events happen at random time intervals. The exponential distribution is focused on the importance of the noise interference occurring rather than on the time it took to occur or not to occur. This simplicity allows an environment with modeled random noise without the complexity of matching real-world time interactions of the noise and the signal. Next, the failure and success rate of interference is constant as both results in an exponential distribution [34]. The exponential random distribution for values either greater or equal to zero is given by

$$f(x) = \lambda e^{-\lambda^x}. \tag{42}$$

The exponential distribution is often referred to as the parameter λ that has a variance given by $\sigma^2 = (1/\lambda)^2$, while its mean and standard deviation is given by $u = \sigma = (1/\lambda)$ [12]. In terms of geolocation principles, the standard deviation of the exponential distribution becomes an additive component to the TOA measurement resulting in the total TOA given by

$$TOA_T = TOA_m + \left(\frac{1}{\lambda}\right) \tag{43}$$

where TOA_m is the noiseless measured TOA value and $1/\lambda$ is the mean exponential distributed noise.

2. TDOA Noise Model

The TDOA noise model is built similarly to the TOA model. Instead of the absolute time for a signal to propagate to a pair of sensors, the relative time is measured. For sensors S_i and S_j, Equation (6) is calculated with the additive noise for both sensors and given by

$$TDOA_T = TDOA_m + \left(\left(\frac{1}{\lambda_{S_i}}\right) - \left(\frac{1}{\lambda_{S_j}}\right)\right). \tag{44}$$

The property of adding independent random variables that are identically distributed gives the variance as $2\sigma^2_{S_{ij}}$, while the subtractive property of independent random variables results in the mean $(1/\lambda) - (1/\lambda)$ equal to zero, and the standard deviation equal to $\sqrt{2}(1/\lambda)$ [17].

3. FDOA Noise Model

The FDOA noise model is built around the concept of the difference in the Doppler shift of a signal from an emitter between two sensors. Instead of the exponential random distribution, the Gaussian random distribution was chosen in [12] due to the variations in frequency above and below the central value of the base frequency sent from the emitter. This work is summarized here for continuity and familiarity. The two sensors

S_i and S_j are both subjected to additive noise. Adding this noise to Equation (24) gives the total FDOA equation given by

$$FDOA_T = \frac{f_o}{c_o}\left[\frac{S_j(t)-e(t)}{\| S_j(t)-e(t)\|}\left(v_{s2}(t)-v_e(t)\right)-\frac{S_i(t)-e(t)}{\| S_i(t)-e(t)\|}\left(v_{s1}(t)-v_e(t)\right)\right]+(\phi_{S_i}-\phi_{S_j}) \quad (45)$$

where $(\phi_{S_i}-\phi_{S_j})$ is the difference of two Gaussian distributed noises from both sensors and is added as a bias.[12] The Gaussian PDF is given by

$$f(x)=\frac{1}{\sqrt{2\pi\sigma^2}}e^{\frac{-(x-m)^2}{2\sigma^2}} \quad (46)$$

where m is the mean and σ^2 is the variance. As in the case for the TDOA equation, the FDOA mean is zero. Similarly, if the standard deviations of the noises are equal, then the standard deviation of the Gaussian noise $\phi_{S_i}-\phi_{S_j}$ is equal to $\sqrt{2}$ times greater than the original Doppler shift [12].

D. NOISE MODELING AND MITIGATION

Noise correction and mitigation techniques play an integral part in ensuring the precision required in modern GPS implementation techniques. The delay caused by noise factors is difficult to predict, varies greatly, and changes with each passing year. Individually, the troposphere and ionosphere have unique variables that interact with the signal and cause degradation and delay. Moreover, these two regions are not isolated from one another but overlap causing complex interactions that require detailed analysis in order to account for the combination of effects on the signal as it propagates. In order for a delay to be mitigated, it must be calculated or modeled with precision according to real-time measurements to achieve a high level of accuracy. In this section, we reveal the background techniques that make mitigation techniques today successful. This provides a baseline necessary to understand and implement future model and mitigation techniques necessary for single frequency geolocation.

1. Troposphere Nosie Factor Mitigation

The troposphere is not frequency dependent up to 15 GHz and, therefore, cannot be mitigated through the use of dual frequency measurements [35]. While the troposphere's dry components can be calculated through the use of timely pressure data from ground stations, the wet component has high variability in space and temperature [36]. Therefore, models represent the best estimates of delay through this region that otherwise could be left unmitigated. In addition to these components, the elevation angle from the emitter to the sensor is an important factor in understanding delay in this region. Typically, low elevation angles result in high tropospheric delay and can have high precision modeling inaccuracies [37]. Lower angles can see upwards of 20 m error in positioning [38]. This is due to the long path that a signal travels through the atmosphere. In addition, rarely does a signal travel in a straight line from the emitter to the sensor. Instead, NLOS conditions are readily present with numerous refractive elements existing in the atmosphere [39].

a. Empty Set Model

The simplest model to implement for tropospheric mitigation is the Empty Set. This set is based around the assumption that the troposphere region is nonexistent. The removal of this region is modeled by adding a constant delay ranging between two and twenty meters [40]. The advantage of this model is that increased focus can be leveraged toward system and ionosphere effects on the signal rather than effects from the troposphere. While this is advantageous for region or system specific modeling, it carries the disadvantage of real-time and high-precision application. Additionally, the overlapping parameters between the troposphere and ionosphere may be miscalculated or extremely complex leaving undeterminable variables that lead to additional errors in positioning.

b. Hydrostatic and Wet Tropospheric Models

While hydrostatic or "dry" conditions for the troposphere can be calculated more easily due to high accuracy temperature, pressure, and ideal gas law conditions, modeling aids in the complex interaction between the troposphere and the ionosphere as well as

extending predictions further into the future [41]. The following models attempt to drive elevation angle as low as possible while not sacrificing accuracy. The lower the elevation angle allows more usable sky to incorporate accurate geolocation calculations. In addition, the models attempt to capture the correct variability in seasonal and yearly changes in the environment in order to output values that are relevant.

c. Saastamoinen Mapping Model

In 1972, Eino Saastamoinen created a model for Tropospheric delay that was the cornerstone of future research. The basic premise is based on the idea that the elevation angle direction in an equal dry environment, when taking the amount of surface pressure and correcting for latitude and height, produces accurate results for the atmosphere conditions [42]. The equation for the Tropospheric delay is given by

$$\delta = \frac{.002277(1+G)}{\cos(\alpha)}\left(S_p + \left(\frac{1255}{S_t} + .005 \right) S_{ppwv} - H_c \tan^2(\alpha) \right) + E_c \qquad (47)$$

where G is the correction for gravity, α is elevation angle at the emitter, S_p is the emitter antenna pressure, S_t is the emitter antenna temperature, S_{ppwv} is the emitter partial pressure of water vapor, H_c is a height dependent correction, and E_c is an elevation dependent correction. Accuracy of this model is in excess of 100 mm [42]. The Saastamoinen model represents the first formal attempt to model the troposphere. It recognizes the important factors that affect signals in this region and attempts to quantify them in a way that allows for a general use over a wide range of operations.

d. Marini, Davis, Neil, and Herring Mapping Models

Another way to look at the delays of the Tropospheric model is to analyze the main operational areas of the satellite and then separate operating parameters from atmospheric parameters [43]. This was accomplished in variations by Marini [43], Davis [44] , Neil [42] and Herring [45] through the use of continued fractions that attempt to find the most precise value for a function. The advantages of the continued fraction include increased speed in mathematical computation, fewer errors, and increased

precision [46]. The general formula in relation to geolocation principles is given by the mapping function

$$M_f(\varepsilon) = \frac{1}{\sin(\varepsilon) + \dfrac{v_1}{\sin(\varepsilon) + \dfrac{v_2}{\sin(\varepsilon) + v_3}}} \tag{48}$$

where v_1 and v_2 are comprised of the surface pressure of the atmosphere, surface temperature, temperature decrease rate, water vapor pressure, and height of the troposphere while ε is the elevation angle [47]. Variable v_3 is a constant. From these variables, the mapping function is equal to the delay of the signal through the troposphere for a given elevation angle. Precision errors using variations of this method reduce the usable elevation angle down to three degrees and places the errors within the millimeter range. The greatest delays recorded came from the accuracy of ground station data inputted into the variations of the continued fraction equations to produce the delay from the mapping function. Radiosonde data is collected from a balloon equipped with atmospheric monitoring equipment that monitors conditions in real time and immediately passes the information to a local station. Comparison of this data to the mapping function inputs provides the best measure of resolution accuracy. In addition, it provides a precise baseline to measure the validity of the tropospheric environmental data used in the calculations. The inherent problem with long term use of Radiosonde data is the relatively short time on station that prevents long term use as a direct geolocation correction input to the chosen mapping function.

2. Ionosphere Noise Factor Mitigation

Ionospheric variability heavily outweighs that of the troposphere and is the most significant component of delay as Hoque states: “The first order term includes about 99% of the total ionospheric effect”[48]. The first order term as derived in Equations (40) through (48) is one of the most important factors in mitigating delay; however, it is not the only effect that the signal must endure as it passes through this region. The remaining one percent that is composed of propagation delays such as residuals, scintillation, higher order ionospheric terms, refraction, and group delays enables

precision in order of millimeters [48]. When a weapon traveling at hundreds of miles an hour over long ranges is off by a millimeter at each calculation of precision, it may miss the target. The following discussion provides a summary of the "one percent" factors as applicable to high altitude sensors. In addition, three ionospheric categories of models are explored for their applicability to the geolocation solution. Lastly, ionospheric tomography is discussed as this method shows significant findings for current and future research in geolocation.

a. Propagation Delay

The ionosphere is a region of the atmosphere in constant flux due to the changes in solar and space activity. When a burst or stream of energy is strong enough, it causes electrons to break free from the atom. Factors, such as wind, time of day, and solar cycle, cause the strength of electron fields to vary, which results in different refraction coefficients for signals largely based on their frequency [49]. The proper mitigation of ionosphere data starts with this understanding. Data must be collected for not only the ionosphere but also for space events based on the exact time when the signal propagation occurs. In addition, for accurate geolocation, being able to predict upcoming changes in space weather is paramount in adjusting algorithms and calculations to remove these affects.

b. Refractive Index

The basic concept of a refractive index in geolocation terms is the difference that a signal bends in a theoretical non-noise environment to that which it bends in a specific time and place in the ionosphere. Calculating the index is accomplished by way of [50]. It is assumed that the airborne sensor is a satellite operating at 19,000 kilometers and its signal is propagating through the ionosphere to geolocate an unknown target within its footprint. The reflective index is given by

$$R_i = \sqrt{1 - \frac{P}{1 - \frac{Q^2 \sin^2 \theta_{wm}}{2(1-P)} \pm \sqrt{\frac{Q^4 \sin^4 \theta_{wm}}{4(1-P)} + Q^2 \cos^2 \theta_{wm}}}} \tag{49}$$

where

$$P = \left(\frac{P_f}{f} \right)^2, Q = \frac{G_f}{f}, G_f = \frac{e_c P_{mf}}{2\pi e_m}, P_f = \frac{1}{2\pi} \sqrt{\frac{N_e e_c^2}{e_m e_o}}, \tag{50}$$

where f is the single frequency utilized by the satellite, θ_{wm} is the angle between the signal propagating through the ionosphere and the magnetic field of the Earth, e_c is the charge of the electron, P_{mf} is the plasma magnetic field magnitude, G_f is the gyro frequency of the electron, e_m is the mass of the electron, N_e is the number of electrons in unit volume $(/m^3)$ in the local plasma's medium, and e_o is the permittivity of free space. The index is simplified through the known parameter of the signal frequency at 1575 MHz. In addition, if the ionosphere is approximated as a thin sheet, the pierce point of the signal with the atmosphere has a singular refraction coefficient thereby reducing the variability in this factor. This results in the magnetic field and the electron densities being the two major components in which precise real-time measurements are necessary. The difficulty in assuming a thin sheet model is due to the higher order effects found in the ionosphere. The ionospheric ordered effects are directly related to the phase delay and group delay due to the complex nature in the bending of the ray as it passes through the medium. The calculations of these effects are given by way of [51] and allow for signal precision in the millimeter range. The first order effect that is used to calculate the delay is given by

$$IPD_1 = \frac{7527 c_o}{2 f^3} \int N_e P_{mf} \cos\theta \, dz \tag{51}$$

where c_o is the speed of light and θ is the angle between the magnetic field and wave vectors. The first order term reveals that as frequency increases the ionospheric delay decreases by a cubed factor. The electron density and the magnetic field are integrated across the thickness of the ionosphere where the signal passes through. The second ordered term is given by

$$IPD_2 = \frac{7527 c_o}{2 f^3} P_{mf} u_v \int N_e \, dz \tag{52}$$

where u_v is a unit vector pointing from the emitter to the airborne sensor. Now the magnetic field is a multiplier, and the electron density is still integrated from the lower to the upper part of the ionopsheric region. The third ordered effect is given by

$$IPD_3 = \frac{812.4}{f^4} \int N_e^2 \, dz. \tag{53}$$

Now the magnetic field influence has diminished while the frequency and electron density are the sole influencing agents. While the frequency is known, the constant presence of electron density through each of the ordered effects amplifies its importance in calculations, modeling, and precision.

c. Scintillation

A signal traveling through the ionosphere endures vibrations due to the variability of free electrons along its path. These vibrations cause amplitude and phase changes in the signal before it reaches the satellite. Signals emanating from the Polar Regions and mid latitudes are more prone to this scintillation than others as shown in Figure 22.

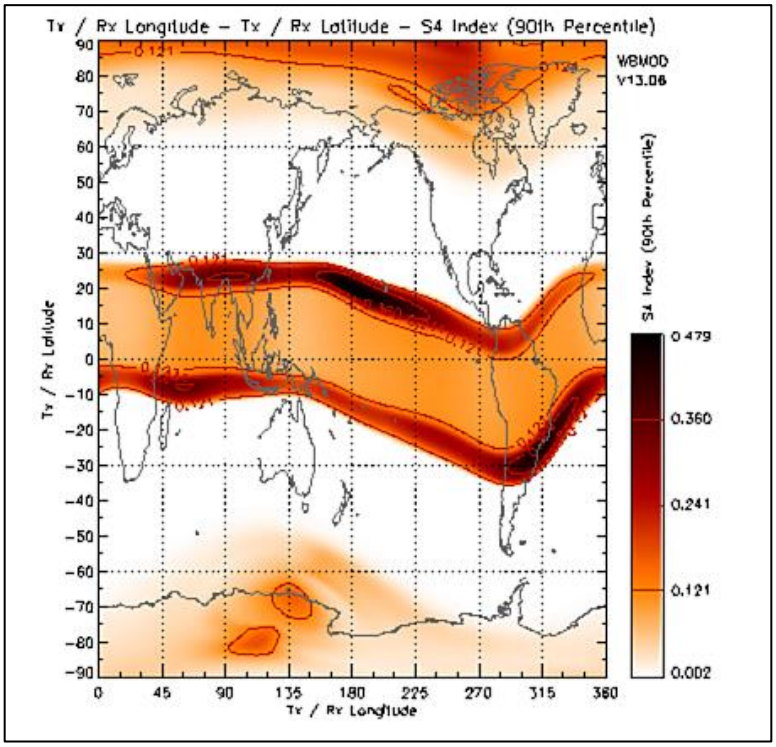

Figure 22. Locations containing heavily focused scintillation, from [52].

The scintillation amplitude delay is performed by way of [53] where the calculation is given by

$$S_A = \sqrt{\frac{(\mathrm{S_e A_s}^2) - (\mathrm{S_e A_s})^2}{(\mathrm{S_e A_s})^2}} \tag{54}$$

where $\mathrm{S_e}$ is the signal traveling from the emitter to the sensor, and $\mathrm{A_s}$ is the amplitude of the signal. Non-inclusion of scintillation effects is explained by Humphreys when he states: "…as severity increases, can lead to navigation bit errors, cycle slipping, and complete loss of carrier lock" [54]. Leaving the mitigation to focus on the ninety-nine percent of the ionosphere delay found in electron density can lead to serious errors going undetected. In addition to amplitude delays, scintillation also results in phase delays of the signal. A satellite locks onto the time and frequency of the signal sent by the emitter when the pseudorandom (PRN) code of the signal matches the replicated code generated by the satellite and is in phase, which results in a high correlation [55]. Failure to exactly match the phase results in a lower correlation or possibly an inability to lock the satellite, which causes an additional delay until the process can be successfully completed within a predetermined number of trials. Phase scintillation hampers this process by injecting rapid shifts in the phase of the signal as it travels through these zones. The phase derivation is completed by way of [56] as applicable to our research. The phase equation is given by

$$\varsigma_d = \frac{e_c^2}{2c_o e_o e_m f (2\pi)^2} \int TEC \tag{55}$$

where e_o is the permittivity of free space, e_m is the mass of an electron, and e_c is the charge of an electron. The TEC shapes and determines the extent of the variability of the ionosphere. Furthermore, the various processes outlined in this section detail the complex environment in which a signal must travel in order to reach its target. Mitigation is more than calculations of neatly separated factors. Instead, it is an intertwined network of forces that must be understood in parts and mitigated as a whole in order to fully remove its effects.

d. Tomography

The first order ionospheric effect of the ionosphere as calculated in Equation (51) lays a dependence on the integral of electron density from the lower bound of the ionosphere to its upper bound. Taking this methodology one step further results in the growing field of tomography. Tomography calculates discrete integrals at angles through the volume of the ionosphere in which a signal could travel. The total of these measurements allows for a more detailed analysis of very specific points in order to attempt to model the interactions of free electrons and the signal. The same procedure is accomplished in computerized tomography (CT) scans of human structures in order to diagnose a range of problems. In relation to geolocation, tomography applies similar properties to accomplish the mitigation of TEC. The tomography derivation via the projection slice theorem is explained by way of [57]. Projections of electron density are created parallel to an axis of rotation from a line through the ionosphere. In addition, the one-dimensional Fourier transforms of the projection is equal to the two-dimensional Fourier transforms along the line it is taken from. Each two-dimensional projection is a slice of the density along the path of the signal. The volume of electron density is mapped by way of compiling the two-dimensional Fourier transforms of the slices along a radial path in polar coordinates. Once the polar coordinates have been mapped back to their corresponding Cartesian coordinates, an inverse Fourier transform is performed to create the projection copy of the actual electron volume along the path of the signal. The corresponding ray path coverage is shown in Figure 23 from the Multi-Instrument Data Analysis System (MIDAS) headquartered at the University of Bath.

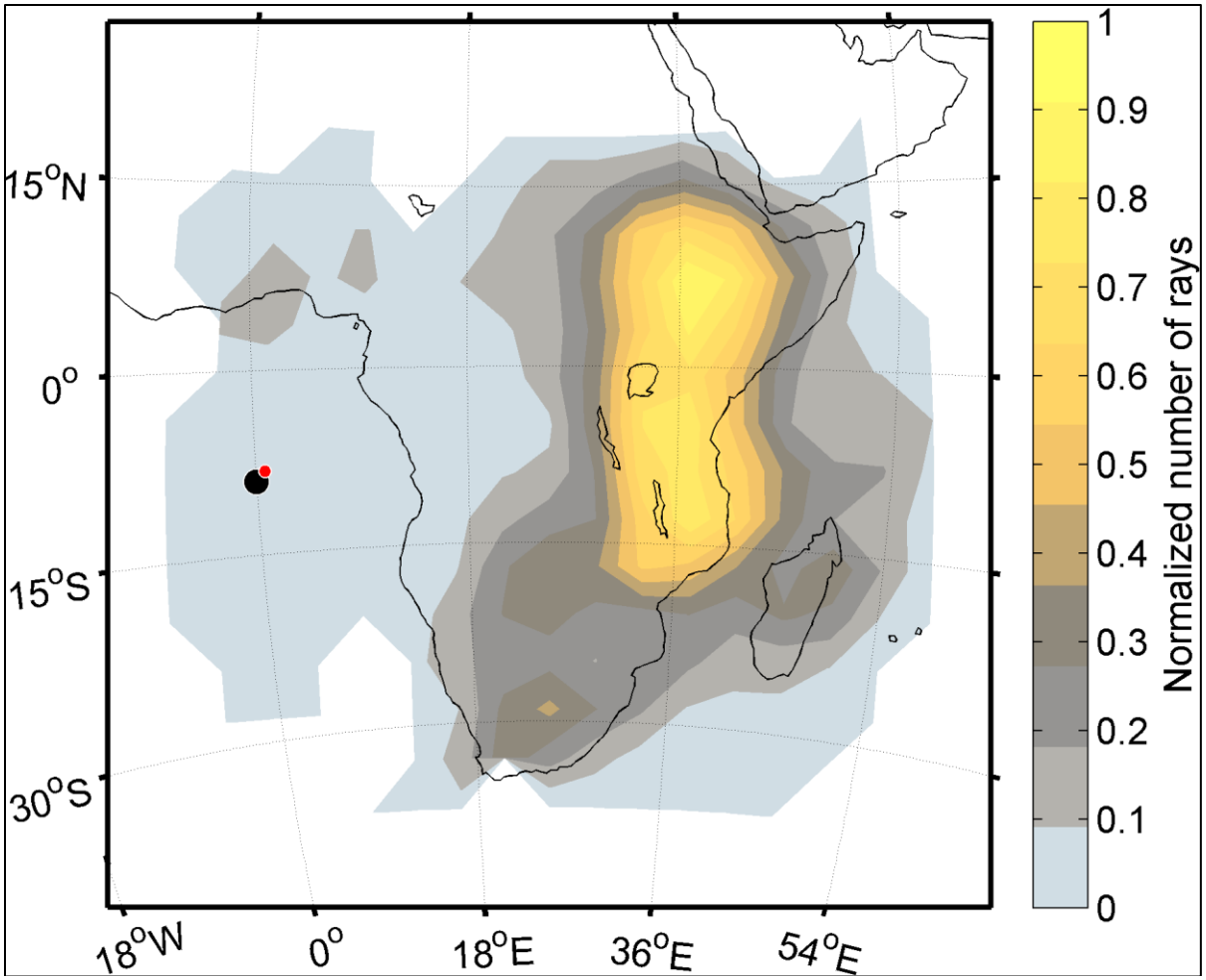

Figure 23. Ray coverage is given based on a requested position near Africa, from [58].

A higher concentration of rays is displayed over the equatorial region which is noted due to the higher levels of electron density found in this region. The red dot signifies the requested ray coverage for geolocation from MIDAS. The corresponding TEC coverage is shown in Figure 24.

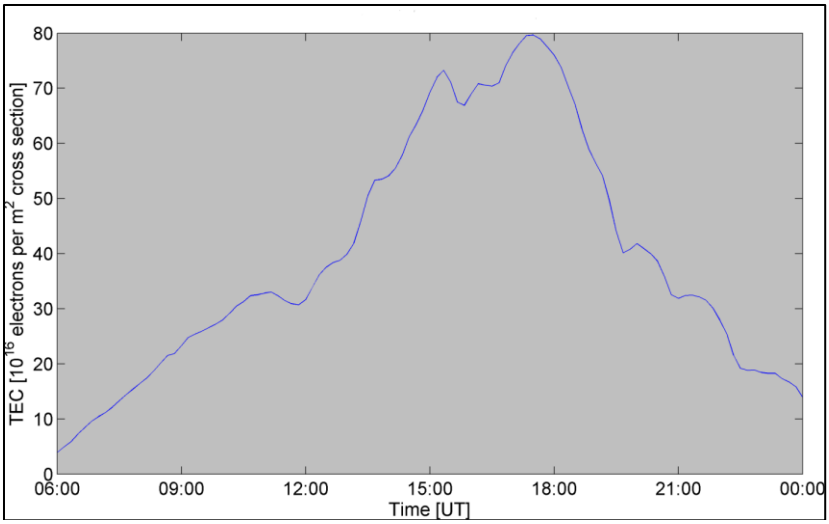

Figure 24. The determination of TEC based on a requested position near Africa for a single day, from [58].

The diurnal changes in TEC values for the corresponding ray coverage in Figure 23 are seen in Figure 24. Peak electron density is reached around 1800, and the lowest levels are recorded at night. Through the use of tomography, the TEC map over Africa is created and shown in Figure 25.

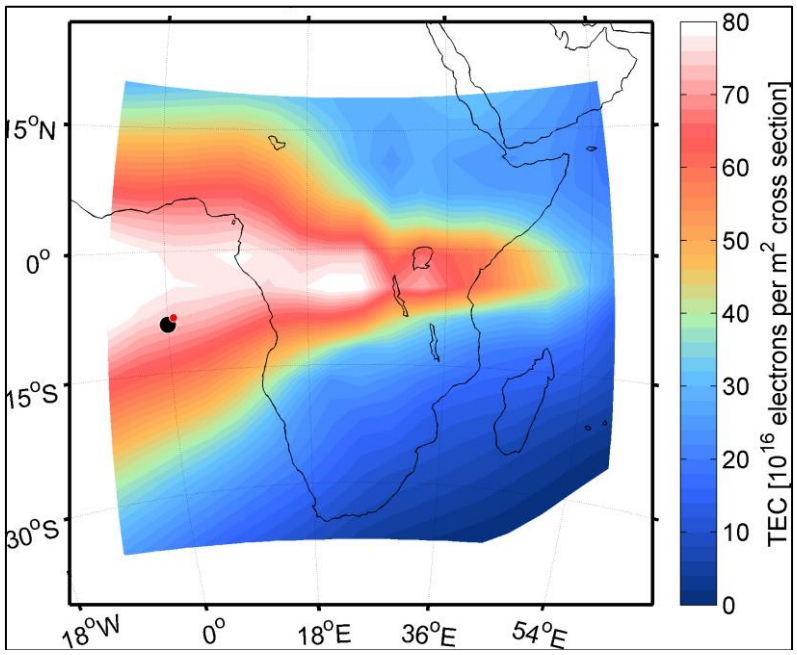

Figure 25. A TEC map is centered on a geolocation position near Africa, from [58].

According to Figure 25, a TEC value of 76 is used for the mitigation of the ionospheric effects. Further accuracy is obtained by the use of mitigation from scintillation, multi-path, refraction, and algorithm specific contributions.

e. Ionospheric Models

Dual-frequency satellites retain the ability to accurately remove first order ionosphere conditions as in Equation (39) through the use of linearly combining the code and phase observables from both the L1 and L2 bands. Single-frequency satellite operations, which only use the L1 band, rely on either a physical or empirical ionosphere model to accurately compensate for the delay [59].

(1) Physical

The two main physical models in operation are the Parameterized Ionosphere Model (PIM) and the Sheffield University Plasmasphere Ionosphere Model (SuPIM). Both models look at the physical and chemical interactions within the ionosphere as a basis to understand how the signal interacts with these factors. The main advantage of the physical model is to produce a close representational model to the actual ionosphere vice one that outputs a mean representation [60]. This allows for system and pre-operation testing at a fraction of the price where changes can be made quickly and retested without affecting systems already in operation. The model is designed to be used with seasonal, solar and regional profiles that affect the E and F layers of the ionosphere.[60] In contrast, the SuPIM model contains additional data relative to magnetic flux in its calculations [61]. Both models' accuracy is wholly dependent on the input measurements received. Inaccuracies on the input parameters negatively affect output accuracy as no filter or cross correlation with other references are utilized. While the physical model offers distinct research advantages, real-world satellite operations as well as a 1997 update to PIM operations focuses on Empirical Modeling to account for delays [62].

(2) Empirical

Empirical modeling defines the delay caused by the ionosphere through the input of real world measurements that are averaged over a long term and then passed along to

the geolocation system for use [63]. The averaging function allows for faster computation times over physical models due to the decrease in overall input parameters. The satellite still receives information that is modeled after real-world measurements; however, minor variations do not increase computation time that ultimately increases geolocation time. The main empirical model for North America is the Klobuchar Model.

The Klobuchar Ionosphere mitigation model is designed for both single-frequency and dual-frequency applications. The algorithm decreases complexity while still utilizing real-world data for input to the algorithm to derive TEC in a seven-step process as given by way of [64] and the ionospheric time delay is represented as

$$K_d = S_f \left[5(10^9) + \sum_{m=0}^{3} \partial_m G_m \left(1 - \frac{q^2}{2} + \frac{q^4}{24} \right) \right] \tag{56}$$

and

$$q = \frac{2\pi (T_l - 50400)}{\sum_{m=0}^{3} \wp_m G_m} \tag{57}$$

where S_f is the slant factor, ∂_m and $\wp_m$ are coefficients transmitted in the message to the satellite, T_l is the local time, and G_m is the geomagnetic latitude. The major drawback to the Klobuchar model is the limited number of factors that represent real-world conditions and results in a fifty percent reduction in delay only for regions between the highly variable equator and polar regions [61]. The limitation in coverage does not hinder operations throughout the continental United States as covered by the GPS satellite system.

THIS PAGE INTENTIONALLY LEFT BLANK

VI. SYNTHETIC APERTURE: TOA

A. OVERVIEW

The use of synthetic aperture calculations in GPS allows the data either from a single sensor over multiple time steps or multiple sensors over several time steps to be combined into a single solution. The refinement in the combination algorithm along with a high number of samples allows the system to output high resolution data. The flexibility of synthetic aperture calculations has allowed the implementation of the technique to be implemented in various fields such as imaging, acoustics, and radar. One major advantage that synthetic aperture delivers to geolocation implementation is the ability to geolocate sources in an under constrained environment. The optimal case of four or more sensors in geolocation is not always possible due to natural and man-made constraints. Synthetic aperture eliminates the hindrances of these constraints and still allows geolocation precision across a wide range of applications.

B. SOLUTION STRATEGY

Three sensors can geolocate an unknown emitter as detailed in Chapter II. Fundamentally, the intersection of three TOA spheres is determined by the intersection of two radial range curves (see Figure 9). This is the basis for determining the synthetic aperture TOA solution.

1. Parametric Circular Solutions

A parametric equation allows a set of points to be stated as a function of a given parameter. A parameterized circle is derived by way of [65] and is given by

$$r(t) = r\cos(t)\hat{n} + rsin(t)\hat{m} \tag{58}$$

where r is the radius of the circle, t is the set of points making up the circumference of the circle, $\hat{n}$ is a unit vector parallel to the circular plane, and $\hat{m}$ is a unit vector perpendicular to $\hat{n}$. The cross product $\times$ of $\hat{n}$ and $\hat{m}$ is given by the new variable

$$\hat{h} = \pm(\hat{n} \times \hat{m}) \tag{59}$$

and is graphically represented in Figure 26.

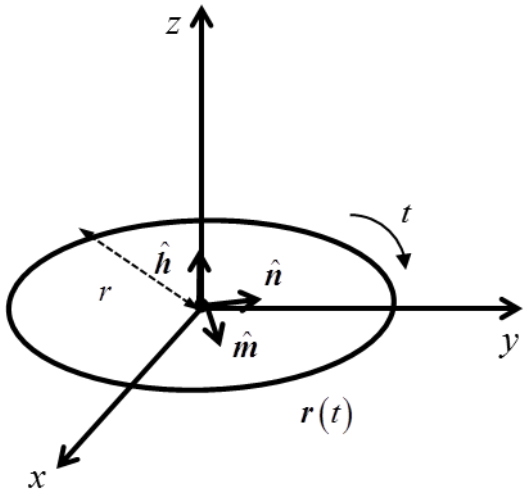

Figure 26. The graphical representation of a parameterized circle.

In geolocation operations, the sensor operates at a fixed distance above the emitter. This distance is denoted as a vector C_r where the emitter is at the origin and extends to the sensor as shown in Figure 27.

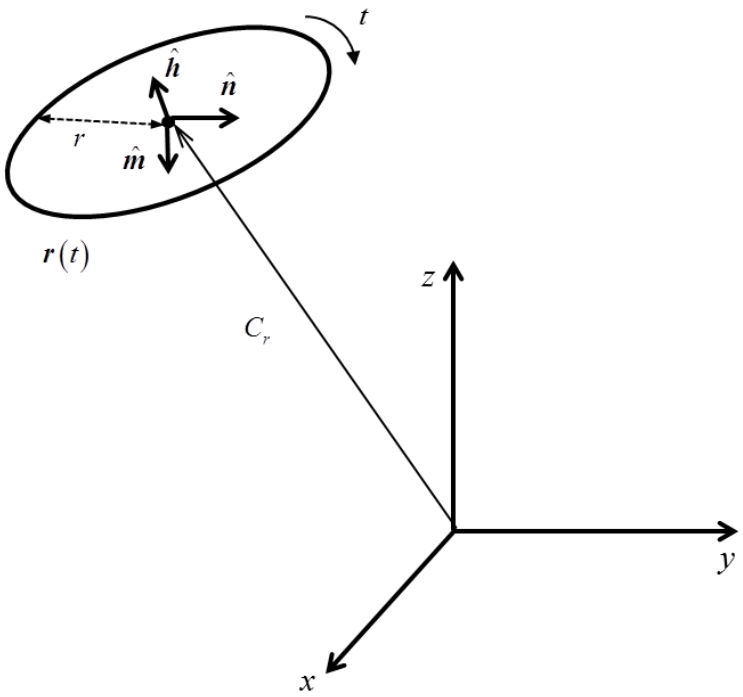

Figure 27. A parameterized circle is represented graphically.

Building off of the two-sensor scenario work in [12], the parameterization of the three-sensor TOA solution is presented. A network of three TOA sensors s_1, s_2, and s_3 is deployed in a noise-free environment in three-dimensional coordinates with positional vectors $\boldsymbol{p}_1$, $\boldsymbol{p}_2$, and $\boldsymbol{p}_3$, respectively. The three sensors are grouped in pairs to geolocate the emitter e. In the first iteration, sensors s_1 and s_2 begin to receive the beacon signal from the emitter. Utilizing Equations (1) and (2), we get the TOA measurement

$$\|\boldsymbol{p}_{esi}\| = \|\boldsymbol{p}_e - \boldsymbol{p}_{si}\| = \tau_{esi} c_o, \quad i = 1,2,3 \tag{60}$$

where $\boldsymbol{p}_e$ and $\boldsymbol{p}_{si}$ are range vectors beginning at the coordinate system origin and extending to the emitter and respective sensor. The term $\boldsymbol{p}_{esi}$ is the difference between the vectors $\boldsymbol{p}_e$ and $\boldsymbol{p}_{si}$. A cross-sectional view of the TOA measurement is shown in Figure 28.

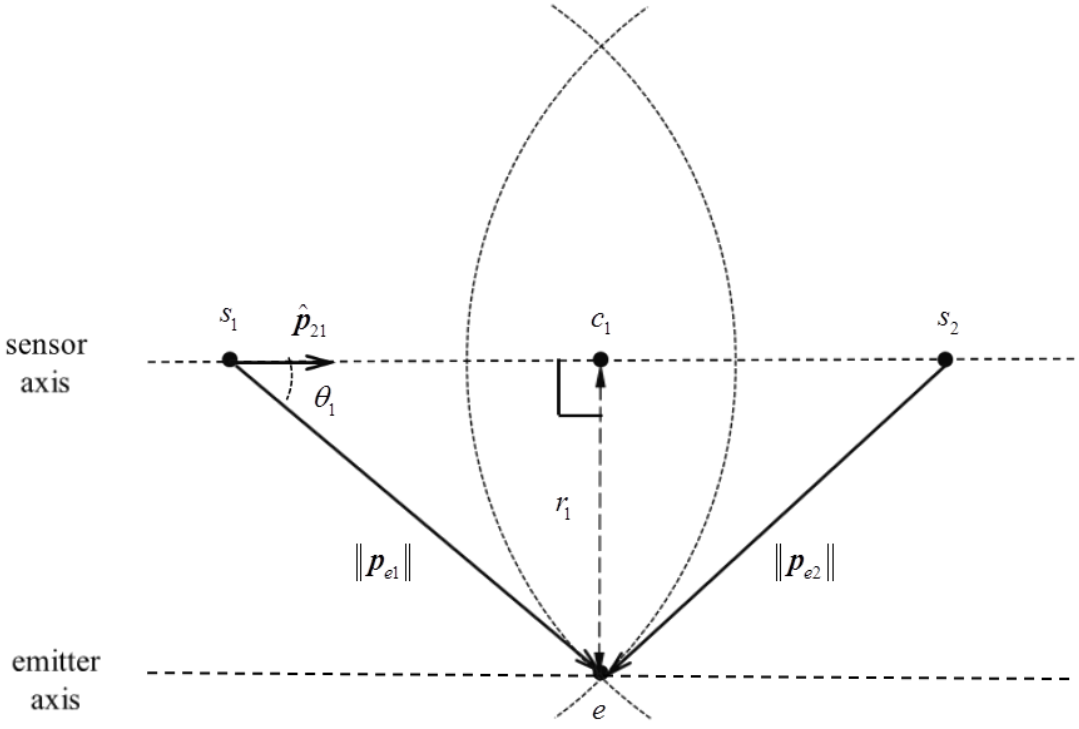

Figure 28. A cross section of sensors s_1 and s_2 performing a TOA geolocation measurement.

The variable $\hat{p}_{21}$ is a unit vector pointing from sensor s_1 to sensor s_2, while r_1 is the radius of the circular solution and c_1 is the center of the circular solution. Variables $\|\boldsymbol{p}_{e1}\|$ and $\|\boldsymbol{p}_{e2}\|$ are scalar range measurements from the respective sensor to the emitter. In order to translate these parameters into known amounts, we apply the law of cosines by way of [12] such that

$$\|\boldsymbol{p}_{e2}\|^2 = \|\boldsymbol{p}_2 - \boldsymbol{p}_1\|^2 + \|\boldsymbol{p}_{e1}\|^2 - 2\|\boldsymbol{p}_{e1}\|\|\boldsymbol{p}_2 - \boldsymbol{p}_1\|\cos(\theta_1). \tag{61}$$

In greater detail, θ_1 is given by

$$\theta_1 = \arccos\left(\frac{\|\boldsymbol{p}_2 - \boldsymbol{p}_1\|^2 + \|\boldsymbol{p}_{e1}\|^2 - \|\boldsymbol{p}_{e2}\|^2}{2\|\boldsymbol{p}_{e1}\|\|\boldsymbol{p}_2 - \boldsymbol{p}_1\|}\right) \tag{62}$$

while r_1 is given by

$$r_1 = \|\boldsymbol{p}_{e1}\|\sin(\theta_1). \tag{63}$$

In order to relate the unit vectors to parameterized values as shown in Figure 27, we set

$$\hat{h} = \hat{p}_{21} \tag{64}$$

due to the solution circle lying perpendicular to the plane of the sensors. Finally, we need to parameterize the unit values of $\hat{n}$ and $\hat{m}$. A chosen $\hat{n}$ value in which the *z*-component is zero simplifies the solution, and this implies

$$\hat{n} \bullet \hat{p}_{21} = (\hat{n}_x\hat{x} + \hat{n}_y\hat{y} + 0\hat{z}) \bullet (\hat{p}_{21x}\hat{x} + \hat{p}_{21y}\hat{y} + \hat{p}_{21z}\hat{z}) = 0 \tag{65}$$

where the root of Equation(65) is determined to be

$$\hat{n} = \left(-\sqrt{\frac{\hat{p}_{21y}{}^2}{\hat{p}_{21x}{}^2 + \hat{p}_{21y}{}^2}}\right)\hat{x} + \left(\sqrt{\frac{\hat{p}_{21x}{}^2}{\hat{p}_{21x}{}^2 + \hat{p}_{21y}{}^2}}\right)\hat{y} + (0)\hat{z} \tag{66}$$

Lastly, the parameter $\hat{m}$ is given by

$$\hat{m} = \hat{n} \times \hat{h} \tag{67}$$

where $\hat{h}$ and $\hat{n}$ are given in Equations (64) and (66), respectively. The first iteration of sensors is fully parameterized, and the second iteration which occurs simultaneously with the first iteration is evaluated. In the second iteration, sensors s_1 and s_3 begin to receive

the beacon signal from the emitter. A cross-sectional view of the TOA measurement is shown in Figure 29.

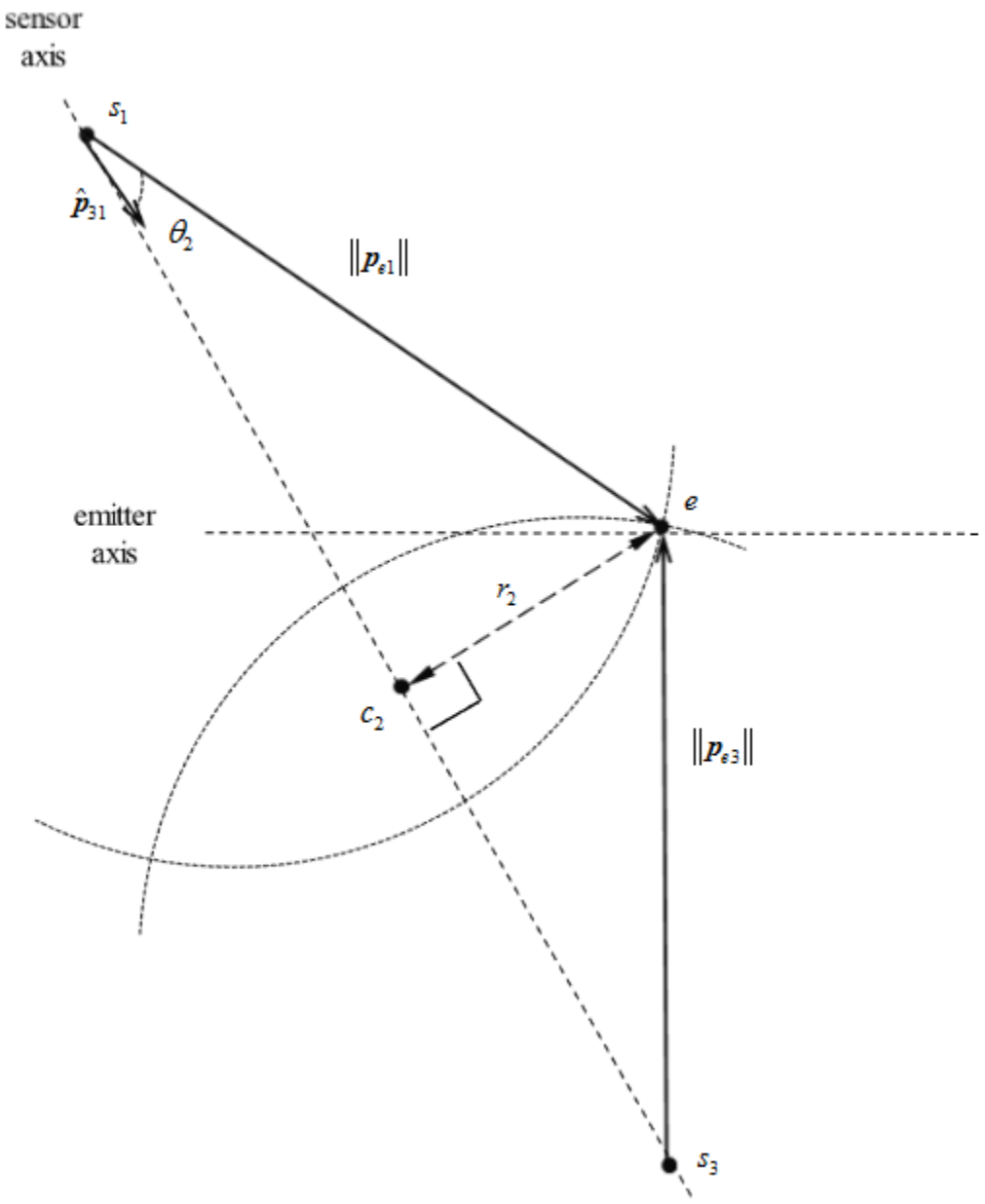

Figure 29. A cross-section of sensors s_1 and s_3 performing a TOA geolocation measurement.

The variable $\hat{p}_{31}$ is a unit vector pointing from sensor s_1 to sensor s_3, while r_2 is the radius of the circular solution and c_2 is the center of the circular solution. Variables $\|\boldsymbol{p}_{e1}\|$ and $\|\boldsymbol{p}_{e3}\|$ are scalar range measurements from the respective sensor to the emitter. In order to translate these parameters into known amounts, we apply the law of cosines by way of [12] such that

$$\|\boldsymbol{p}_{e3}\|^2 = \|\boldsymbol{p}_3 - \boldsymbol{p}_1\|^2 + \|\boldsymbol{p}_{e1}\|^2 - 2\|\boldsymbol{p}_{e1}\|\|\boldsymbol{p}_3 - \boldsymbol{p}_1\|\cos(\theta_2). \tag{68}$$

In greater detail, θ_2 is given by

$$\theta_2 = \arccos\left(\frac{\|\boldsymbol{p}_3 - \boldsymbol{p}_1\|^2 + \|\boldsymbol{p}_{e1}\|^2 - \|\boldsymbol{p}_{e3}\|^2}{2\|\boldsymbol{p}_{e1}\|\|\boldsymbol{p}_3 - \boldsymbol{p}_1\|}\right) \tag{69}$$

while r_2 is given by

$$r_2 = \|\boldsymbol{p}_{e1}\|\sin(\theta_2). \tag{70}$$

In order to relate the unit vectors to parameterized values as shown in Figure 27, we set

$$\hat{h} = \hat{p}_{31} \tag{71}$$

due to the solution circle lying perpendicular to the plane of the sensors. Finally, we need to parameterize the unit values of $\hat{n}$ and $\hat{m}$. A chosen $\hat{n}$ value in which the *z*-component is zero simplifies the solution and is given by

$$\hat{n} \bullet \hat{p}_{31} = (\hat{n}_x\hat{x} + \hat{n}_y\hat{y} + 0\hat{z}) \bullet (\hat{p}_{31x}\hat{x} + \hat{p}_{31y}\hat{y} + \hat{p}_{31z}\hat{z}) = 0 \tag{72}$$

where the root of Equation(72) is determined to be

$$\hat{n} = \left(-\sqrt{\frac{\hat{p}_{31y}{}^2}{\hat{p}_{31x}{}^2 + \hat{p}_{31y}{}^2}}\right)\hat{x} + \left(\sqrt{\frac{\hat{p}_{31x}{}^2}{\hat{p}_{31x}{}^2 + \hat{p}_{31y}{}^2}}\right)\hat{y} + (0)\hat{z}. \tag{73}$$

Lastly, the parameter $\hat{m}$ is the same as Equation (67). The second iteration of sensors is fully parameterized, and the third iteration which occurs simultaneously with the first and second iteration is evaluated. In the third iteration, sensors s_2 and s_3 begin to receive the beacon signal from the emitter. A cross-sectional view of the TOA measurement is shown in Figure 30.

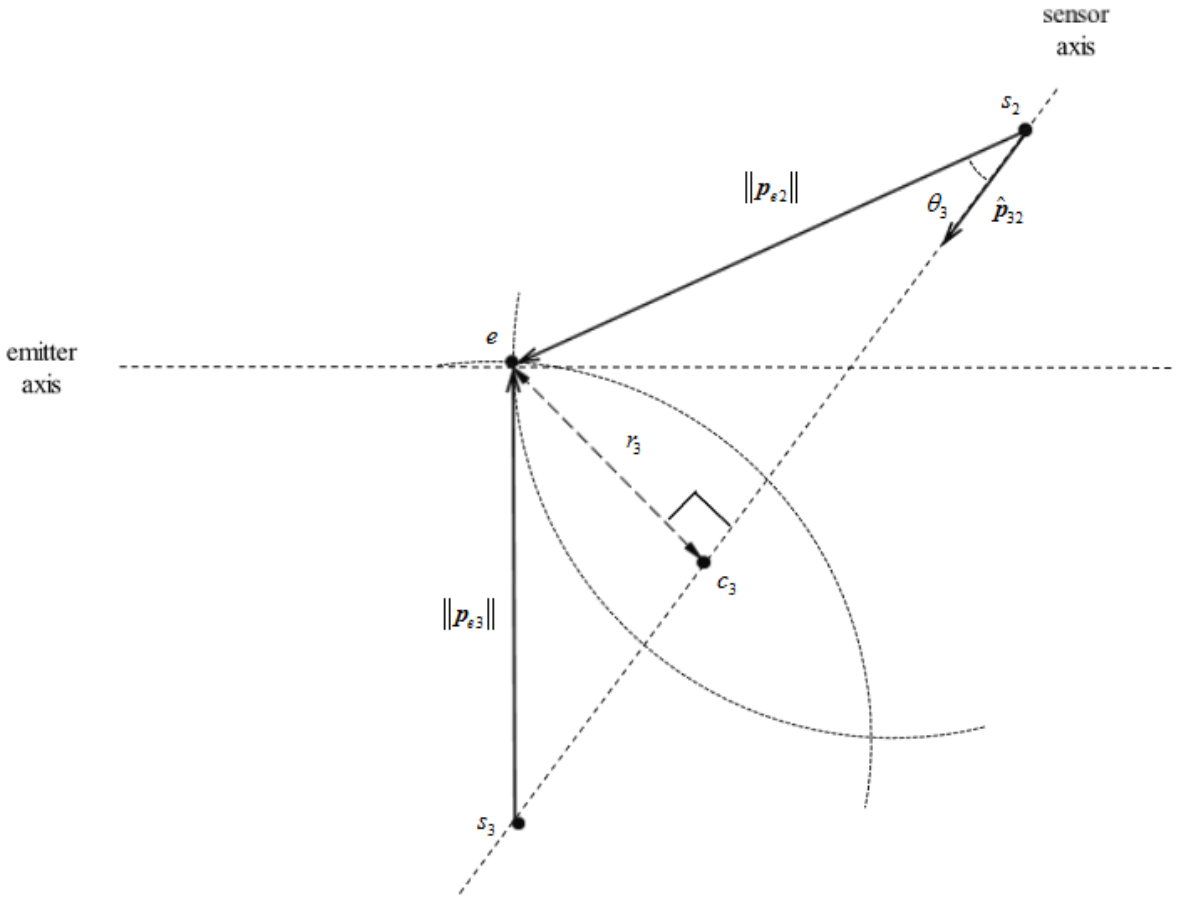

Figure 30. A cross-section of sensors s_2 and s_3 performing a TOA geolocation measurement.

The variable $\hat{p}_{32}$ is a unit vector pointing from sensor s_2 to sensor s_3, while r_3 is the radius of the circular solution and c_3 is the center of the circular solution. Variables $\|\boldsymbol{p}_{e2}\|$ and $\|\boldsymbol{p}_{e3}\|$ are scalar range measurements from the respective sensor to the emitter. In order to translate these parameters into known amounts, we apply the law of cosines by way of [12] such that

$$\|\boldsymbol{p}_{e2}\|^2 = \|\boldsymbol{p}_3 - \boldsymbol{p}_2\|^2 + \|\boldsymbol{p}_{e2}\|^2 - 2\|\boldsymbol{p}_{e2}\|\|\boldsymbol{p}_3 - \boldsymbol{p}_2\|\cos(\theta_3). \tag{74}$$

In greater detail, θ_3 is given by

$$\theta_3 = \arccos\left(\frac{\|\boldsymbol{p}_3 - \boldsymbol{p}_2\|^2 + \|\boldsymbol{p}_{e2}\|^2 - \|\boldsymbol{p}_{e3}\|^2}{2\|\boldsymbol{p}_{e2}\|\|\boldsymbol{p}_3 - \boldsymbol{p}_2\|}\right) \tag{75}$$

while r_3 is given by

$$r_3 = \|\boldsymbol{p}_{e2}\|\sin(\theta_3). \tag{76}$$

In order to relate the unit vectors to parameterized values as shown in Figure 27, we set

$$\hat{h} = \hat{p}_{32} \tag{77}$$

due to the solution circle lying perpendicular to the plane of the sensors. In the same manner as the previous iterations, we need to parameterize the unit values of $\hat{n}$ and $\hat{m}$. A chosen $\hat{n}$ value in which the *z*-component is zero simplifies the solution and is given by

$$\hat{n} \bullet \hat{p}_{32} = (\hat{n}_x\hat{x} + \hat{n}_y\hat{y} + 0\hat{z}) \bullet (\hat{p}_{32x}\hat{x} + \hat{p}_{32y}\hat{y} + \hat{p}_{32z}\hat{z}) = 0 \tag{78}$$

where the root of Equation (78) is determined to be

$$\hat{n} = \left(-\sqrt{\frac{\hat{p}_{32y}{}^2}{\hat{p}_{32x}{}^2 + \hat{p}_{32y}{}^2}}\right)\hat{x} + \left(\sqrt{\frac{\hat{p}_{32x}{}^2}{\hat{p}_{32x}{}^2 + \hat{p}_{32y}{}^2}}\right)\hat{y} + (0)\hat{z}. \tag{79}$$

Lastly, the parameter $\hat{m}$ is the same as Equation (67).

2. Circular Intersections

A synthetic aperture approach to TOA is a dynamic process of processing geolocation points over a set time period. Building off of the framework established in Equation (58) and the work in [12], we move forward explaining how the parametric terms determine circular intersections for three sensors over a specified time period. In order to keep the overall process simplified, we establish a notation that allows specific sensors to be identified throughout the computations. The first TOA iteration involves sensors s_1 and s_2 attempting to geolocate emitter e. Positon vector $\Upsilon_{\psi_{21},\lambda}$ describes the intersected solution ψ of sensors s_2 and s_1 at a time step λ. While many time steps are used to calculate the solution, we focus on time steps λ and $\lambda+1$ for simplicity. Furthermore, the parametric value u_λ for the emitter's geolocated position is represented as $\Upsilon_{\psi_{21},\lambda}(u_\lambda)$. Solving for the values of u_λ and $u_{\lambda+1}$ for which

$$\Upsilon_{\psi_{21},\lambda}(u_{\lambda}) = \Upsilon_{\psi_{21},\lambda+1}(u_{\lambda+1}) \tag{80}$$

allows us to find where subsequent circular emitter curves intersect in time [12]. In real-world operations, errors arising from noise, and algorithm calculations may cause situations where there are no specific intersections between circular curves. In this case, we find the minimum value between successive time points by

$$\| \Upsilon_{\psi_{21},\lambda}(\mu'_{\lambda}) - \Upsilon_{\psi_{21},\lambda+1}(\mu'_{\lambda+1}) \| = \min\left[\Upsilon_{\psi_{21},\lambda}(\mu_{\lambda}) - \Upsilon_{\psi_{21},\lambda+1}(\mu_{\lambda+1}) \right] \tag{81}$$

where μ'_{λ} and $\mu'_{\lambda+1}$ are the positional values under conditions where error is included in the geolocation. With the minimum points identified on both circles, we calculate the midpoint between the points as given by

$$\Lambda_{e,\lambda} = \frac{\Upsilon_{\psi_{21},\lambda}(\mu'_{\lambda}) + \Upsilon_{\psi_{21},\lambda+1}(\mu'_{\lambda+1})}{2}. \tag{82}$$

Equation (82) represents the midpoint between two success time steps of the synthetic aperture geolocation determination. Under normal synthetic aperture operations, a total of T time steps occur. The centroid calculation allows the most likely determination of the emitter's location and is determined by

$$\Lambda_{e1} = \frac{1}{T-1}\sum_{\lambda=1}^{T-1}\Lambda_{e,\lambda} \tag{83}$$

where Λ_{e1} is the emitter position for the first iteration using sensors s_1 and s_2. The second TOA iteration involves sensors s_3 and s_1 attempting to geolocate emitter e. Positon vector $\Upsilon_{\psi_{31},\lambda}$ describes the intersected solution ψ of sensors s_3 and s_1 at a time step λ. The calculations for the second iteration follow the same format as the first iteration. With the focus on time steps λ and $\lambda+1$, the midpoint is given by

$$\Lambda_{e,\lambda} = \frac{\Upsilon_{\psi_{31},\lambda}(\mu'_{\lambda}) - \Upsilon_{\psi_{31},\lambda+1}(\mu'_{\lambda+1})}{2} \tag{84}$$

and the centroid calculation is determined to be

$$\Lambda_{e2} = \frac{1}{T-1}\sum_{\lambda=1}^{T-1}\Lambda_{e,\lambda}. \tag{85}$$

The third and final TOA iteration involves sensors s_3 and s_2 attempting to geolocate emitter e. Positon vector $\Upsilon_{\psi_{32},\lambda}$ describes the intersected solution ψ of sensors s_3 and s_2 at a specific step in time λ. The calculations for the third iteration follow the same format as the first two iterations. With the focus on time steps λ and $\lambda+1$, the midpoint is given by

$$\Lambda_{e,\lambda} = \frac{\Upsilon_{\psi_{32},\lambda}(\mu'_{\lambda}) - \Upsilon_{\psi_{32}\lambda+1}(\mu'_{\lambda+1})}{2}\ , \tag{86}$$

and the centroid calculation is determined to be

$$\Lambda_{e3} = \frac{1}{T-1}\sum_{\lambda=1}^{T-1}\Lambda_{e,\lambda}. \tag{87}$$

With three centroid calculations from each of the sensor pairs, we refine the determination of the emitter's position through an additional centroid calculation given by

$$\Lambda_{eT} = \frac{1}{3}\sum_{j=1}^{3}\Lambda_{ej} \quad j=1,2,3 \tag{88}$$

where j represents the numerical value of the corresponding iteration centroid and Λ_{eT} is the final emitter's position via the TOA synthetic aperture calculation.

3. RMS Error

To objectively evaluate the difference between the estimated position of the emitter Λ_{eT} and the actual position p_e, we utilize the concept of root-mean-square derivation [66]. The distance between the estimated and true positon of the emitter is given by

$$\delta = \| \Lambda_{eT} - p_e \|. \tag{89}$$

The mean-square-error (MSE) which determines the squared difference of positional error in meters squared is given by

$$MSE = E\left[\| \Lambda_{eT} - p_e \|^2 \right] \tag{90}$$

where $E[\bullet]$ is the expected value symbol which is also referred to as the mean value symbol [67]. Taking the square root of the MSE is designated the RMSE and allows the positional error of our results to be calculated in meters by

$$RMSE = \sqrt{MSE} = \sqrt{E\left[\delta^2\right]}. \tag{91}$$

C. RESULTS

The work completed in this thesis for the TOA synthetic aperture approach builds largely off the work accomplished in [12], where two airborne sensors attempted to geolocate an unknown target. We added a third sensor to the calculations and have tested the assumption that additional sensors as well as additional sample points will increase the accuracy of the previous work.

The following scenario provides the framework for the results in the following sections. An emitter e sends out a beacon signal from an unknown positon. Sensor s_1 is located at $(-1000-b,-b,h)$, sensor s_2 is located at $(-b,-b,h)$, and sensor s_3 is located at $(+1000-b,-b,h)$, where h is the height of the sensor and b is the numerical coefficient of the respective Cartesian axis. While all three sensors are traveling at the same speed ς, they collect N TOA measurements over a specific time period T_{SA} [12]. The high noise $\sigma_{\tau H}$ and low noise $\sigma_{\tau L}$ conditions are defined in Chapter V. As GPS geolocation can be performed at different altitudes depending on the sensor employed, we chose to focus the research on high altitude satellites at 19.1 km and low altitude UAV operations at 10 km. These sensors are tested for their performance involving the sensor velocity angular spread and synthetic aperture size as described in the following sections.

1. TOA Velocity Angular Spread

In a three-sensor approach, there are three velocity angles that must be accounted for and held constant in order to test their validity. Each sensor s_i corresponds to a specific velocity v_i where i is the specific number corresponding to the sensor and velocity pair. For sensors s_1 and s_2 the corresponding angle α_1 is given by

$$\alpha_1 = \left(\frac{v_1 \cdot v_2}{\| v_1 \| \| v_2 \|} \right) = \arccos\left(\frac{v_1 \cdot v_2}{\varsigma^2} \right). \tag{92}$$

Furthermore, the angle α_2 for sensors s_2 and s_3 is given by

$$\alpha_2 = \left(\frac{v_2 \cdot v_3}{\| v_2 \| \| v_3 \|} \right) = \arccos\left(\frac{v_2 \cdot v_3}{\varsigma^2} \right). \tag{93}$$

Finally, the angle α_3 for sensors s_1 and s_3 is given by

$$\alpha_3 = \left(\frac{v_1 \cdot v_3}{\| v_1 \| \| v_3 \|} \right) = \arccos\left(\frac{v_1 \cdot v_3}{\varsigma^2} \right). \tag{94}$$

Each angle is confined to a range between zero and 180 degrees while the velocity moves the sensor through the spread angles [12]. The arrangement of sensors, equivalent velocities as well as their corresponding angles is shown in Figure 31.

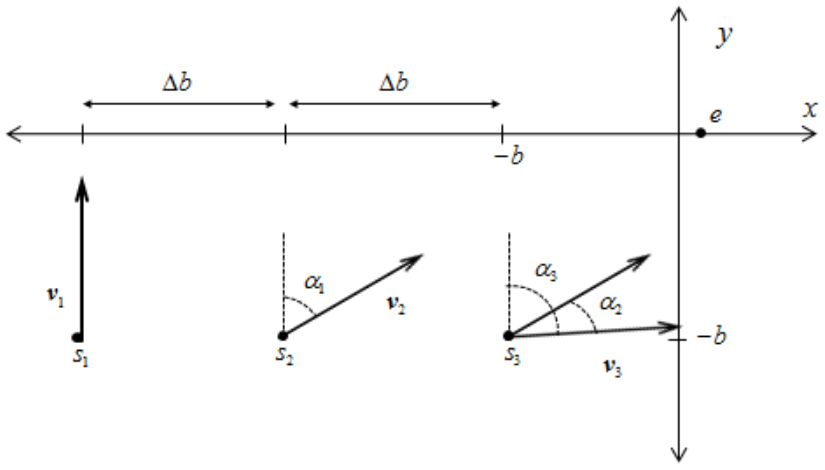

Figure 31. The visual representation of velocity angle spread.

For the first two-sensor iteration, the velocity v_1 for sensor s_1 remains fixed so that $v_1 = \varsigma \hat{y}$. The second velocity v_2 for sensor s_2 is adjusted to provide the spread where

$$v_2 = \varsigma \sin(\alpha_1)\hat{x} + \cos(\alpha_1)\hat{y}. \tag{95}$$

In the second two-sensor iteration, the velocity v_2 for sensor s_2 becomes the reference where v_3 for sensor s_3 is adjusted to provide the spread by

$$v_3 = \varsigma \sin(\alpha_2)\hat{x} + \cos(\alpha_2)\hat{y}. \tag{96}$$

In the third and final two-sensor iteration, the velocity v_1 for sensor s_1 again is fixed, while sensor s_3 is adjusted to provide the required spread α_3.

Each pair of TOA measurements collected is analyzed over either 20,000, 40,000, 60,000 or 80,000 sample points as shown by black dots in Figure 32 [12].

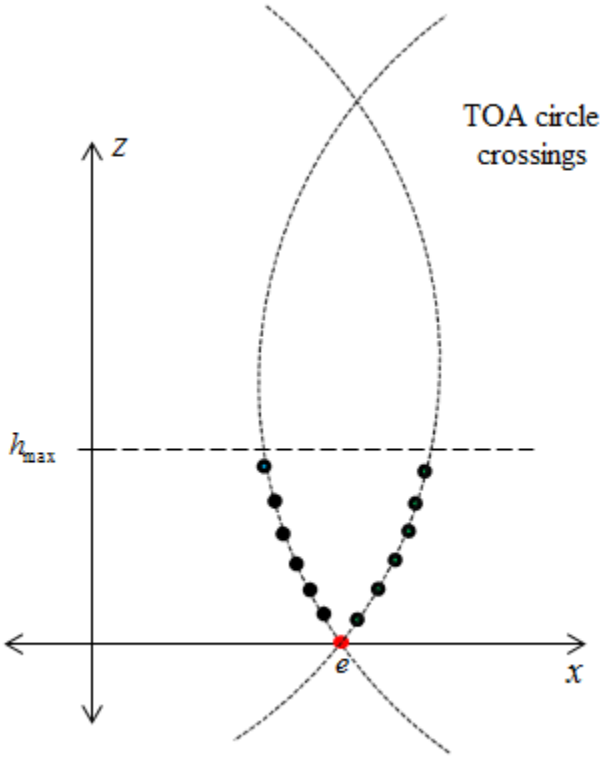

Figure 32. Sample points analyzed from a pair of TOA measurements constrained by altitude.

The altitude constraint $h_{\max}$ prevents extraneous computations for emitter geolocation beyond what is physically possible and reduces the time to provide a solution [12].

a. Satellite Sensors

The list of parameters and their corresponding values in Table 1 were used to conduct the TOA synthetic aperture angular velocity approach for both satellite and UAV sensors.

Table 1. TOA algorithm parameters are given for the TOA angular velocity spread calculations.

Parameter (units)	Satellite Sensors	UAV Sensors
h (m)	19.10×10^{6}	3.048×10^{3}
ς (m/s)	3.889×10^{3}	51.44
α (degrees)	variable on [0,90]	variable on [0,90]
N (samples)	5	5
ΔT_{SA} (s)	225	2.72
b (m)	1.750×10^{6}	280.1
$\sigma_{\tau H}$ (ns)	9.11	10.0
$\sigma_{\tau L}$ (ns)	0.911	1.0
$h_{\max}$ (m)	5000	1000

(1) Two versus Three Satellite Sensors No Noise Comparison

The most optimal test for the three-satellite TOA synthetic aperture configuration is in a noise free environment. This allows the algorithm to be tested for errors before noise is introduced into the calculations. The two-sensor TOA synthetic aperture calculations derived from [12] serve as the baseline for the comparison with the research completed in this thesis for the three-sensor approach. The work completed in [12] focused on the output solely at 20,000 samples due to high computation requirements in processing the data. We expanded the previous research to include samples taken at 40,000, 60,000 and 80,000 intervals. Emitter location RMSE is plotted against the number of samples across a range of twenty degrees to seventy degrees angular spread for two satellite sensors in Figure 33. The lines between the points were not directly

tested and are generated via linear interpolation. In addition, Figure 33 contains two important metrics for interpreting the value of the data. First, the lines on the graph show the amount of error for a specific angular separation across the sample interval. Second, at the specific sample intervals of 20,000, 40,000, 60,000, and 80,000 points, the graph is read vertically to show the angular trend for the given interval.

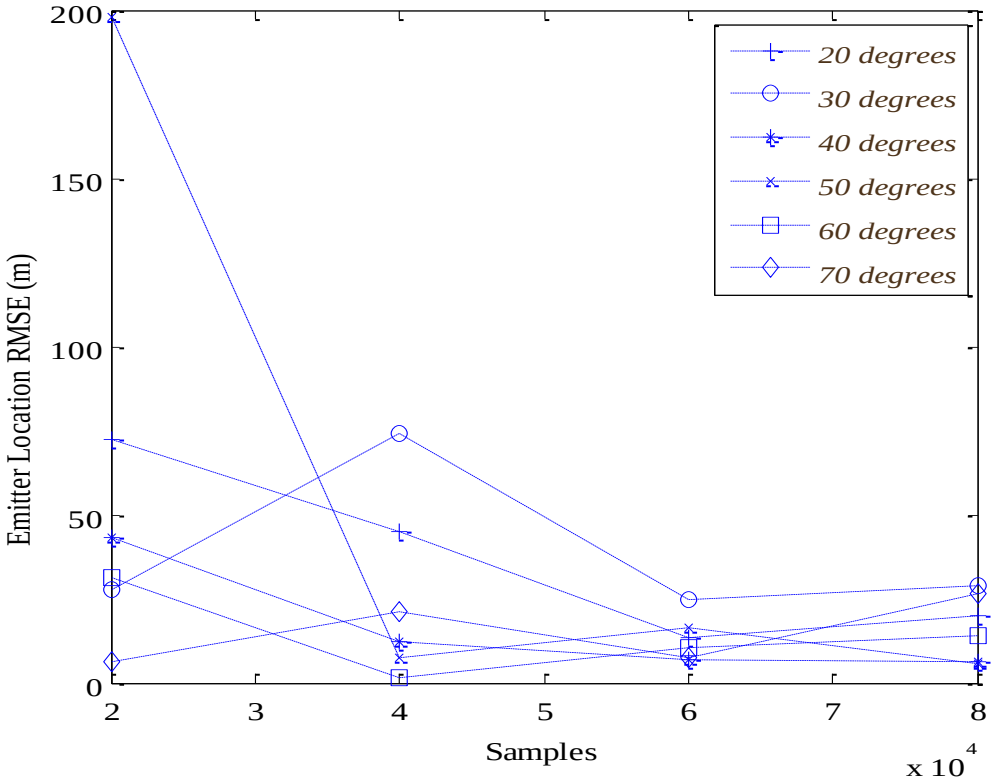

Figure 33. Emitter location RMSE is plotted against number of samples for two satellite sensors from twenty degrees to seventy degrees angular separation utilizing no noise interference.

The vertical trend for the 20,000, 60,000 and 80,000 sample points shows a significant variability between angular separation and increasing and decreasing values of emitter location error. The increase at these sample points does not guarantee a better position estimate as hypothesized in [12]. The most probable explanation in this variability comes from accuracy errors in the calculation algorithm in regards to the circular intersections and the calculations for the maximum height as the increasing

precision found up to 20,000 samples in [12] no longer holds constant. At 40,000 samples, there is a general trend of increasing precision in relation to the increase in angular velocity. While variability exists even at this sample point, it does highlight the calculations can produce results in keeping with previous research in [12]. The horizontal trend for 20 and 40 degrees of angular separation show a general increasing position trend as the sample points increase. At the low angular separation values of 20 and 30 degrees as well as the high end of 60 and 70 degrees, the odd values tend to have higher values of error in comparison to the even values across all sampled points. Further research is required to determine the reason behind this trend.

The research in [12] calculated the highest precision using a 70 degree separation angle resulting in a 6.0 meter error with no atmospheric noise injected into the equation. Increasing the sample points resulted in a higher precision using a 60 degree separation angle resulting in a 1.3 meter error. The most consistent increase of precision over the 20,000 to 80,000 sample range comes from a 40 degree separation angle decreasing from an error of 43.45 meters at 20,000 samples to an error of 5.4 meters at 80,000 samples. Additional sample points may provide a better position estimate, but due to the high computational demands it was not performed for this research. It is evident from the calculations that the algorithm can provide better resolution between 40 and 50 degrees separation with increased sampling above 40,000 points. At 80,000 samples, the error values were half the amount at 40,000 samples for these angles of separation, whereas an angular separation of 40 degrees dropped the error from 12.0 meters to 6.0 meters and 50 degrees dropped the error from 7.0 meters to 5.0 meters. It is plausible that additional sample points may provide higher position accuracy; however, due to the limited tests conducted, it cannot be stated for certain. With the two sensor test as the baseline, the calculations under the same parameters was run for three satellite sensors, and the results are shown in Figure 34.

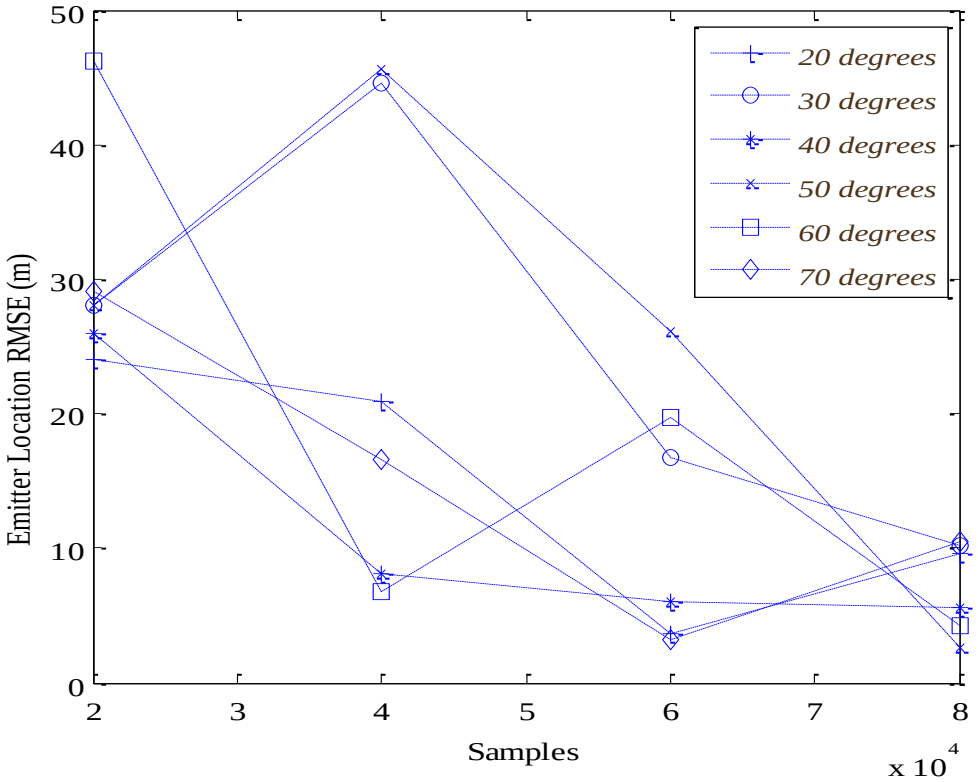

Figure 34. Emitter location RMSE is plotted against number of samples for three satellite sensors from twenty degrees to seventy degrees angular separation utilizing no noise interference.

The vertical trend for each of the sampled points shows an oscillation between successive angles of separation. These results stem from the calculation changes in angular separation between groups of sensors as the angle increases; however, the horizontal trend shows an overall increasing precision corresponding to the increase of sample points. In order to maintain a near identical comparison between two-sensor and three-sensor application approaches, the fusion technique remained the same between the two and was only adapted to include the third sensor. This most likely resulted in sub-optimal results stemming from additional errors included from the third sensor. Future research should investigate adjusting the position algorithm from fusing two sensors at a time and then finding the centroidal point between them to fusing all three points at once in order to evaluate the estimated position. While overall trends can be identified through

the results in Figures 33 and 34, a more detailed look at the error received at specific angles of separation allows for a more detailed analysis as shown in Figure 35.

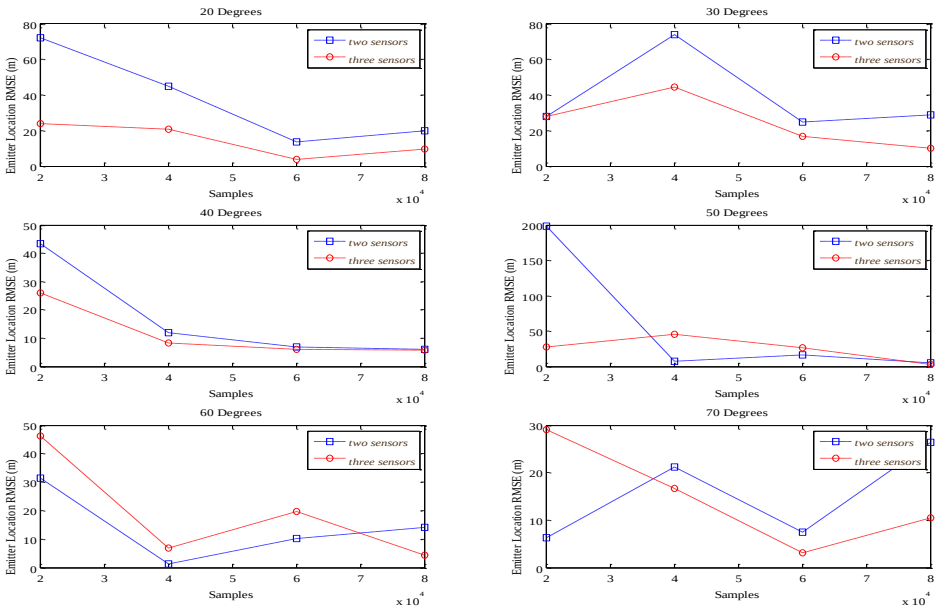

Figure 35. Emitter location RMSE is plotted against number of samples for two and three satellite sensors from twenty degrees to seventy degrees angular separation utilizing no noise interference.

The three sensor TOA synthetic aperture calculations are broken down into single angular separations from twenty degrees to seventy degrees in Figure 35. The boxes increase separation by 10 degrees from top left to bottom right. At 20 and 30 degrees separation across all sample points, the three-sensor technique retains a significant advantage over the two-sensor technique. In addition, the 40 degree angular separation has a 4.0 meter precision increase at 40,000 sample points and decreases to a 0.4 meter precision advantage at 80,000 samples. While the two sensor calculations retain a high precision over the 50 and 60 degree separations, at 70 degrees separation between satellites, the three sensor calculations regain the precision advantage using 40,000 or more sample points. In an ideal no noise environment, the TOA calculations should produce a nearly zero positional error when attempting to geolocate the emitter. Neither the two-sensor or three-sensor approaches are currently capable of providing this

precision. Increased sampling and additional sensors only proves to provide a minimal precision advantage. Errors from these calculations carry forward into the noisy environmental testing.

(2) Two versus Three Satellite Sensors High Noise Comparison

Emitter location RMSE is plotted against the number of samples across a range of twenty degrees to seventy degrees angular spread for two satellite sensors in Figure 36. The tests were run under a high noise environment. The lines between the points were not directly tested and are generated via linear interpolation.

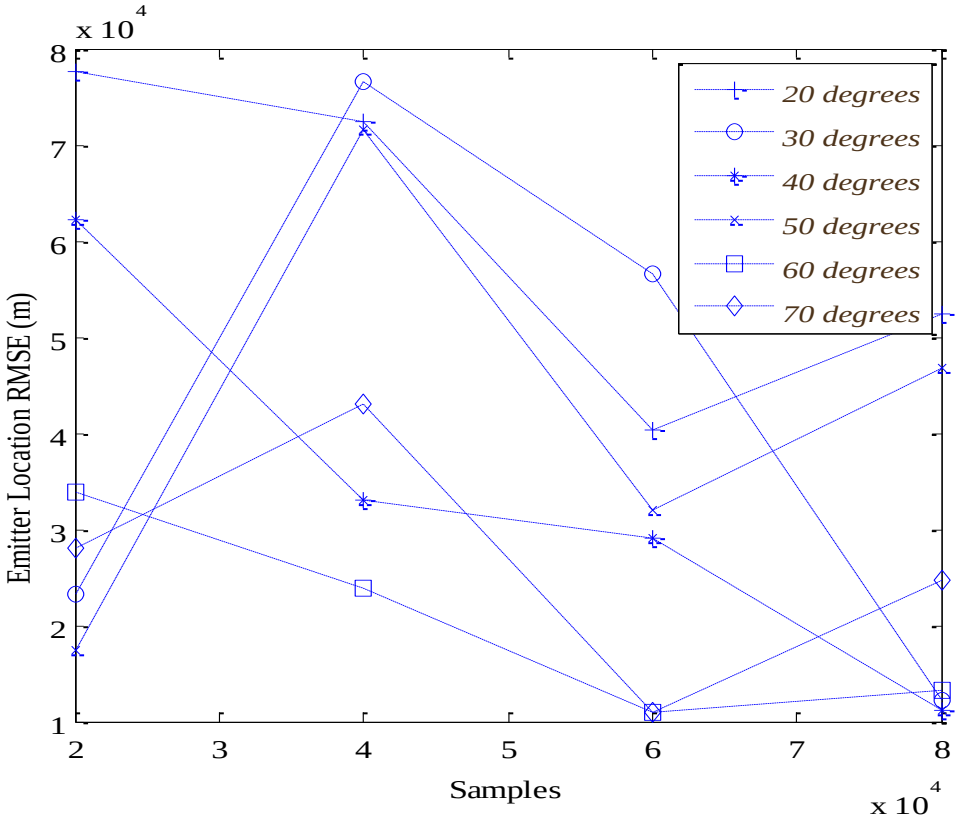

Figure 36. Emitter location RMSE is plotted against number of samples for two satellite sensors from twenty degrees to seventy degrees angular separation utilizing high noise interference.

Many significant features of the TOA synthetic aperture approach are brought forward due to the increase in sample points. First, the overall magnitude of the RMSE at higher sample points from previous research retains a magnitude of error at 10^4. This magnitude at higher sample points negates the ability for this specific algorithm to be used in high precision applications. The higher resolution provided by the additional samples does not outweigh the error introduced from the high noise environment using deviations of 9.11 ns. While angles of 20 degrees, 40 degrees, and 60 degrees show an overall decreasing error slope with an increase of sample points, the 40 degree separation is the only line that has a near linear decrease in error due to the increase in sample points reaching its lowest value at 80,000 samples with an error of 1.115×10^4. Additional testing is required to determine the ideal precise angle and max resolution capable of delivering the best estimation. The best resolution of 1.086×10^4 for the two sensor testing comes from the highest angular separation at 70 degrees closely followed by 60 degrees of separation at 1.092×10^4, both calculated at only 60,000 samples. The relative small difference of 0.198×10^4 between the 40 degree separation error of 1.115×10^4 and the 60 degree separation error of 1.313×10^4 as well as the overall negative trend in the lines displays the characteristic that a higher resolution is obtained in a window between these values as the sample points are increased. With this baseline intact and using the same sample points, emitter location RMSE is plotted against the number of samples across a range of twenty degrees to seventy degrees angular spread for three satellite sensors in Figure 37.

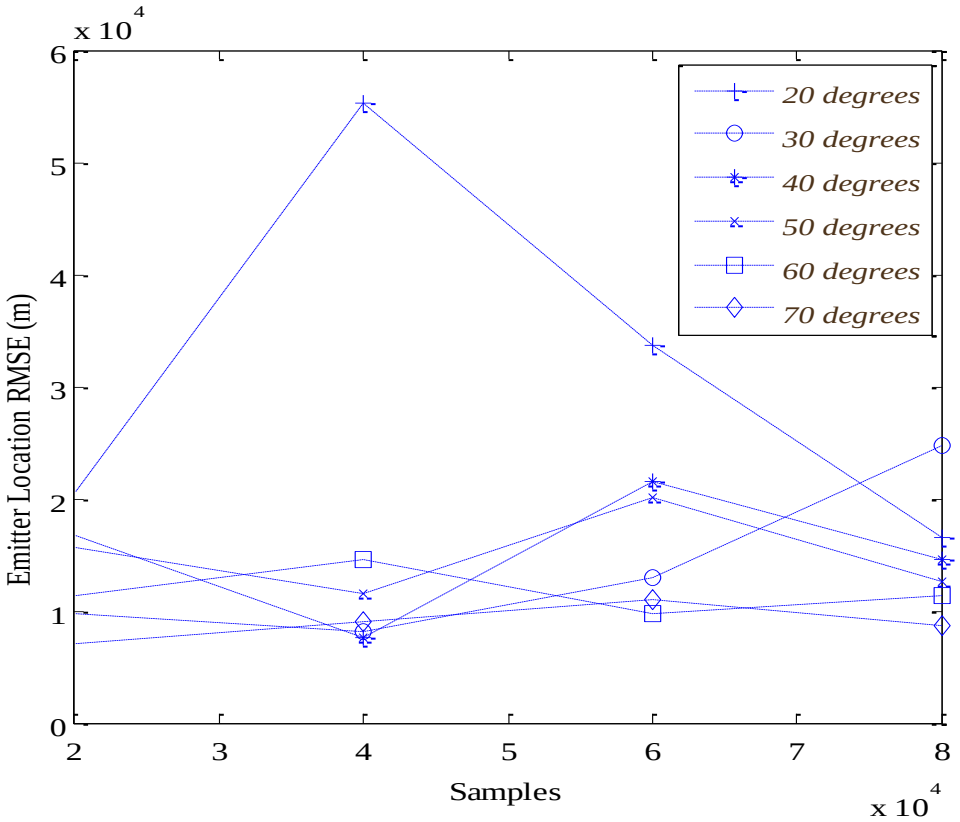

Figure 37. Emitter location RMSE is plotted against number of samples for three satellite sensors from twenty degrees to seventy degrees angular separation utilizing high noise interference.

The introduction of the third sensor not only decreased the error at each sample point, it also decreased the variability of the error at the high noise environment. The overall error magnitude remains the same at 10^4. This correlation between the two and three sensor calculations highlights the fact that neither the increased resolution from a third sensor or the increased samples under this condition can adequately remove the effects of noise on the signal. It is vital that the noise be mitigated for the error to decrease to a point where this algorithm can be used in precision operations. Unlike the two sensor model, the three sensor orientation reveals that error resolution is nearly the same at low and high angular separation. This is advantageous in that when the effects of noise are removed, it lowers the overall error across all angle separations more uniformly. The best precision in this model is found at 40 degrees of separation using 40,000

samples resulting in an error of only 7654 meters. This is a drastic increase in the precision over the two-sensor model. While overall trends can be identified through the results in Figures 36 and 37, a more detailed look at the error received at specific angles of separation allows for a more detailed analysis as shown in Figure 38.

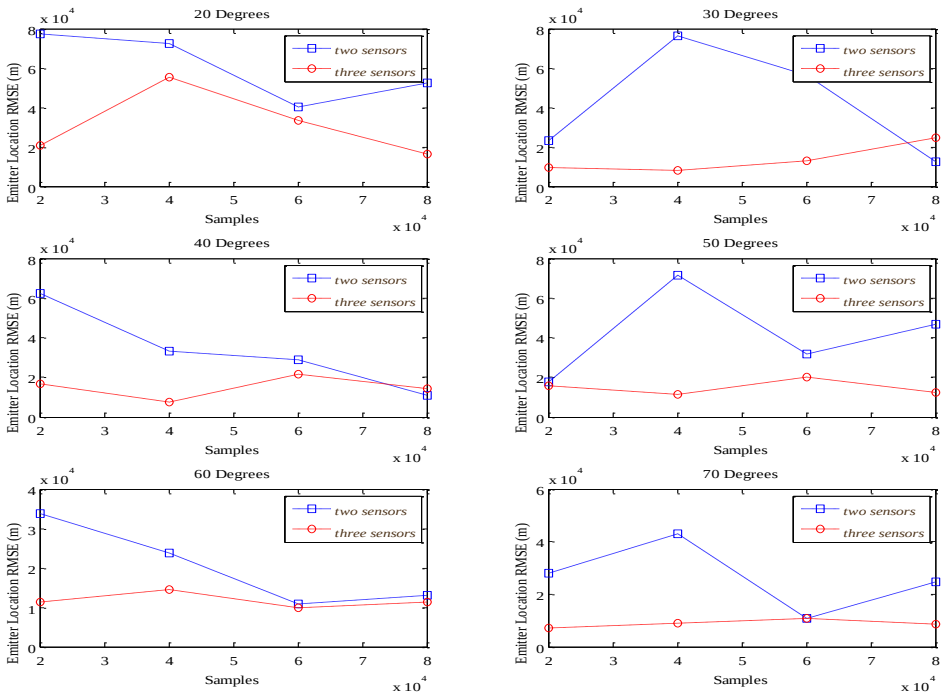

Figure 38. Emitter location RMSE is plotted against number of samples for two and three satellite sensors from twenty degrees to seventy degrees angular separation utilizing high noise interference.

The three sensor TOA synthetic aperture calculations are broken down into single angular separations from twenty degrees to eight degrees in Figure 38. The subplots increase separation by 10 degrees from top left to bottom right. With the exception of points above 70,000 samples at 30 and 40 degree separation, the error of the three sensor approach is significantly less than the two sensor approach. The greatest advantage in precision is seen between 20,000 and 60,000 samples. These results suggest that random sampling is necessary using this algorithm under a high noise environment in conjunction with a specific angular separation of the satellites. This is accomplished through

modifications in the positon determination algorithm. The best precision for the two sensor model is found at 50 degrees of separation using 20,000 samples. Conversely, the lowest error for the three sensor model is 7106 meters at 80 degrees of separation using 20,000 samples. While additional sensors definitively produce better results, additional sample points above 20,000 samples in a high noise environment will not increase precision.

(3) Two versus Three Satellite Sensors Low Noise Comparison

As discussed in Chapter V, ionopsheric noise makes up roughly ninety-nine percent of the delay in the signal as it traverses this region. In order to test the mitigation of this noise in our research, we set the standard deviation to one tenth of the value in the high noise scenario. This corresponds with removing ninety percent of the ionospheric delay and is suitable for testing the algorithm in a near real world scenario. Emitter location RMSE is plotted against the number of samples across a range of twenty degrees to seventy degrees angular spread for two satellite sensors in Figure 39. The lines between the points were not directly tested and are generated via linear interpolation.

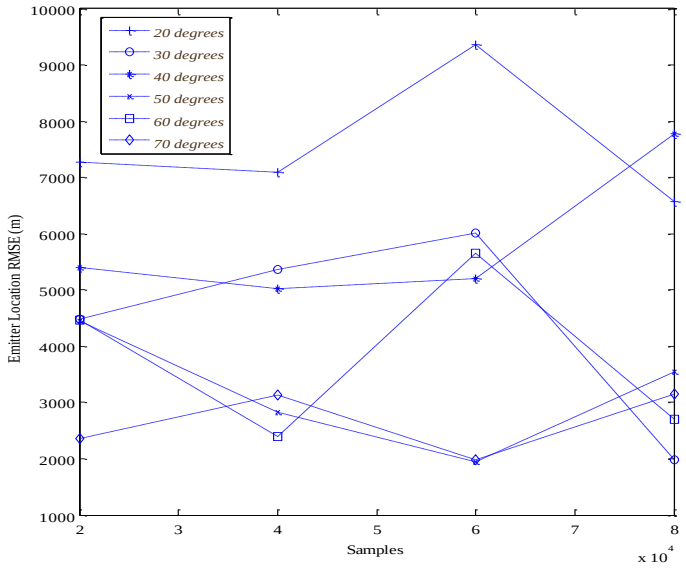

Figure 39. Emitter location RMSE is plotted against number of samples for two satellite sensors from twenty degrees to seventy degrees angular separation utilizing low noise interference.

Comparing Figure 36 to Figure 39 shows a significant reduction in emitter location RMSE confirming that the ionospheric noise was the major contributor holding all other values the same. The lowest error for the low noise model is 1977 meters at 70 and 50 degrees angular separation using 60,000 samples as well as at 30 degrees using 80,000 samples. This provides roughly a 2500 meter improvement for the 30 and 50 degree angles while the 70 degree angle resulted in a 378 meter improvement in the emitter's position estimate. It is also important to note that the low noise model shares a similar variability of results to the high noise model which is not seen when the noise is removed as shown in Figure 33. Additional sample points do not reduce the variability but does provide windows in sampling that result in a better positional estimate. Next, we test the precision of the two-sensor model to the three-sensor model using a low noise scenario. Emitter location RMSE is plotted against the number of samples across a range of twenty degrees to seventy degrees angular spread for three satellite sensors in Figure 40.

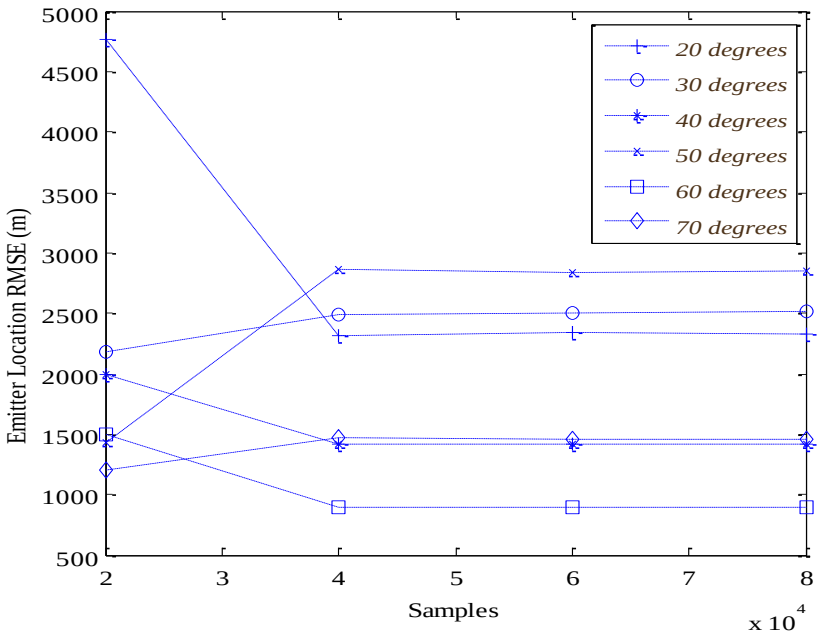

Figure 40. Emitter location RMSE is plotted against number of samples for three satellite sensors from twenty degrees to seventy degrees angular separation utilizing low noise interference.

The vertical trend for the data in Figure 40 shows that while variability to noise still exists, precision increases as the angular spread increases. The horizontal trend shows variability between 20,000 samples and 40,000 samples. In addition, from 40,000 to 80,000 samples the data for all degrees of angular separation are almost the same creating a plateau effect in the graph. There is little value in increasing computation time to obtain 40,000 samples or greater. Next, we compare the two-sensor and three-sensor low noise approaches in Figure 41 in order to gain a better side-by-side evaluation of the effects at each specified degree of angular separation.

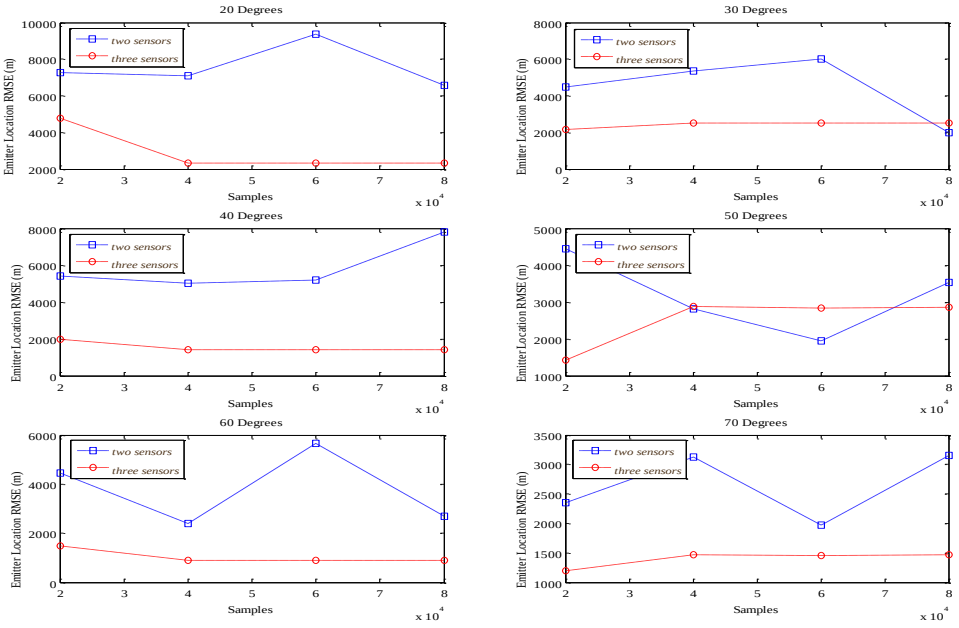

Figure 41. Emitter location RMSE is plotted against number of samples for two and three satellite sensors from twenty degrees to seventy degrees angular separation utilizing low noise interference.

The three-sensor model maintains its precision advantage over the two-sensor model for all angles with the exception at 50 degrees angular separation and 30 degree angular separation at 80,000 samples. The three-sensor model reaches a minimum error at 890.5 meters using an angular separation of 60 degrees. In contrast, the two-sensor model reached the highest precision at 1977 meters using a 30 degree angular separation. The

crossover points in the 30 degree and 50 degree angular separation graphs where the two-sensor model outperforms the three-sensor model may be an indication of the effects of noise variability and the algorithm's ability to calculate an accurate positon at these angles. Further research is required to fully understand the cause of these effects.

b. Two versus Three UAV Sensors

Emitter location RMSE is plotted against the number of samples across a range of angular spread for two UAV sensors in a noise free environment; the results are shown in Figure 42.

(1) Two versus Three UAV Sensors No-Noise Comparison

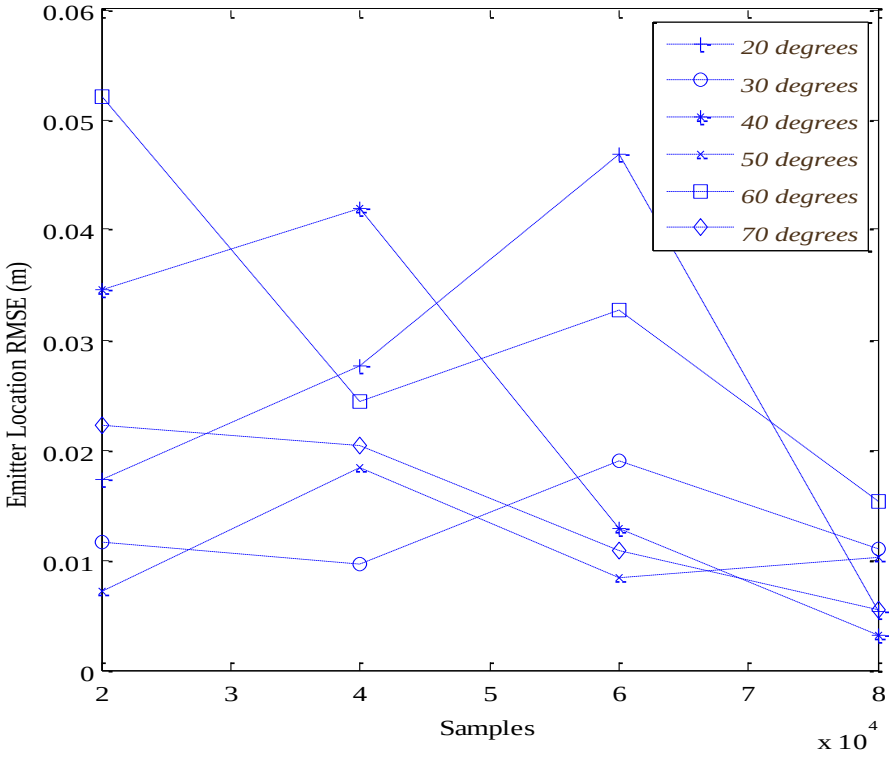

Figure 42. Emitter location RMSE is plotted against number of samples for two UAV sensors from twenty degrees to seventy degrees angular separation utilizing no noise interference.

The vertical trend for the two UAV model has varying precision as the angular separation is increased from 20 degrees to 70 degrees. The precision less than 0.053 meters allows for high accuracy operations to be utilized with this algorithm. The horizontal trend for two UAV sensors mirrors the vertical trend in increasing precision with increased sampling points. By removing small calculation errors in the algorithm, it is possible to further refine the variability and precision of this approach. In comparison, the emitter location RMSE is plotted against the number of samples across a range of angular spread for three UAV sensors in a noise free environment; the results are shown in Figure 43.

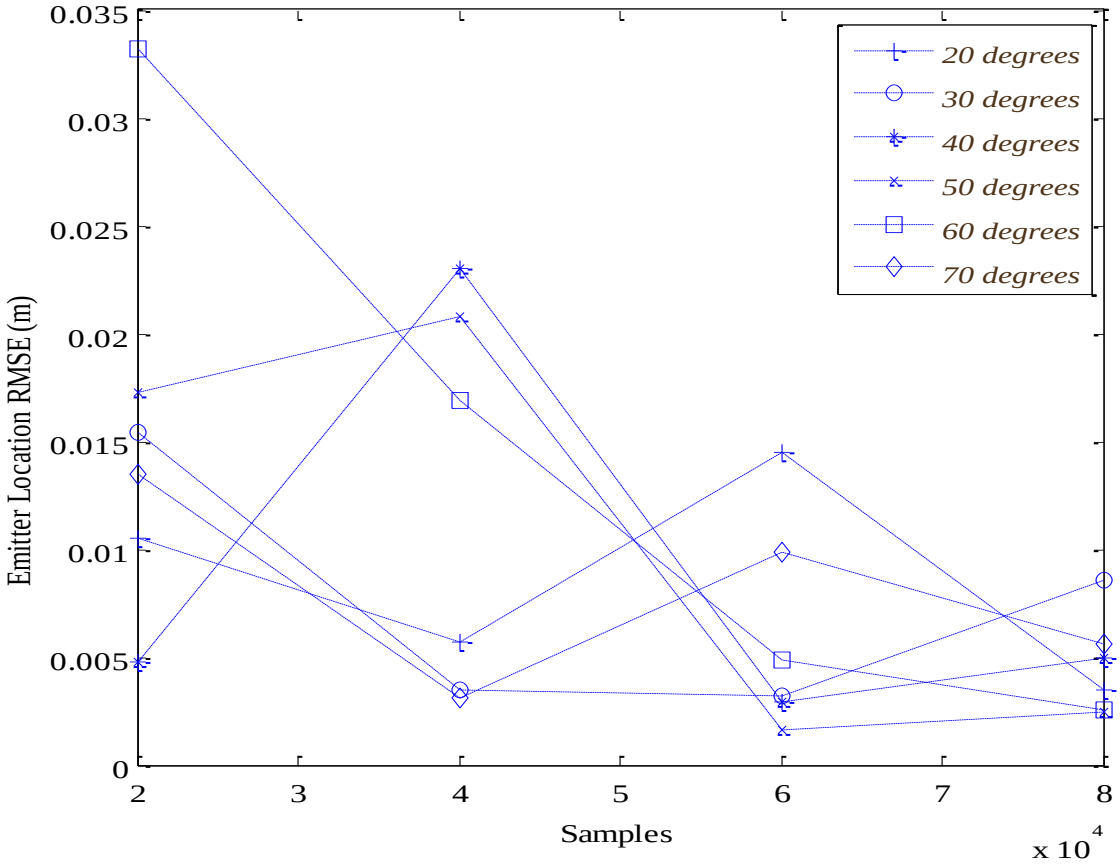

Figure 43. Emitter location RMSE is plotted against number of samples for three UAV sensors from twenty degrees to seventy degrees angular separation utilizing no noise interference.

With the exception of the 20 degree angular spread, the vertical trend of the three UAV model shows a strong increase in precision as angular spread increases. The horizontal trend in Figure 43 shows an overall increase in precision as the angular separation increases. The maximum error in this model is 0.033 meters at 60 degrees angular separation, and the minimum error is 0.0016 meters at 50 degrees of angular separation. Furthermore, as the sample size increases, the horizontal trend shows a decrease in the range of error among the different angular separations. Further testing is required to find the absolute minimum value that this algorithm is capable of producing. Intensive computational demands precluded the examination at points higher than 80,000 samples. At this resolution, the three-sensor model is capable of providing reliable high precision results across a wide range of angular separations. Next, we compare the two- and three-sensor approaches in Figure 44 to gain a better understanding of the effects at different angular separations.

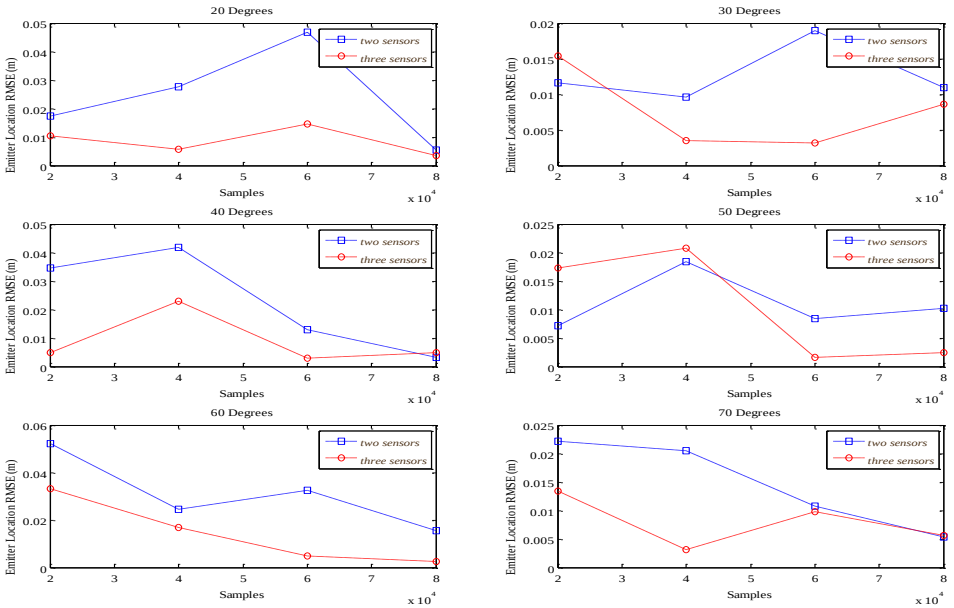

Figure 44. Emitter location RMSE is plotted against number of samples for two and three UAV sensors from twenty degrees to seventy degrees angular separation utilizing no noise interference.

The model outperforms the two-sensor model at increasing sample points using an angular separation of 20 and 60 degrees. In angular separations of 20, 30, and 70 degrees, the two-sensor and three-sensor models precision converges leaving a roughly 0.002 meter difference in performance; however, at angular separations between 50 and 60 degrees, the three-sensor model consistently outperforms its counterpart.

(2) Two versus Three UAV Sensors High-Noise Comparison

Emitter location RMSE is plotted against the number of samples across a range of angular spread for two satellite sensors in Figure 45. The tests were run under a high noise environment. The lines between the points were not directly tested and are generated via linear interpolation.

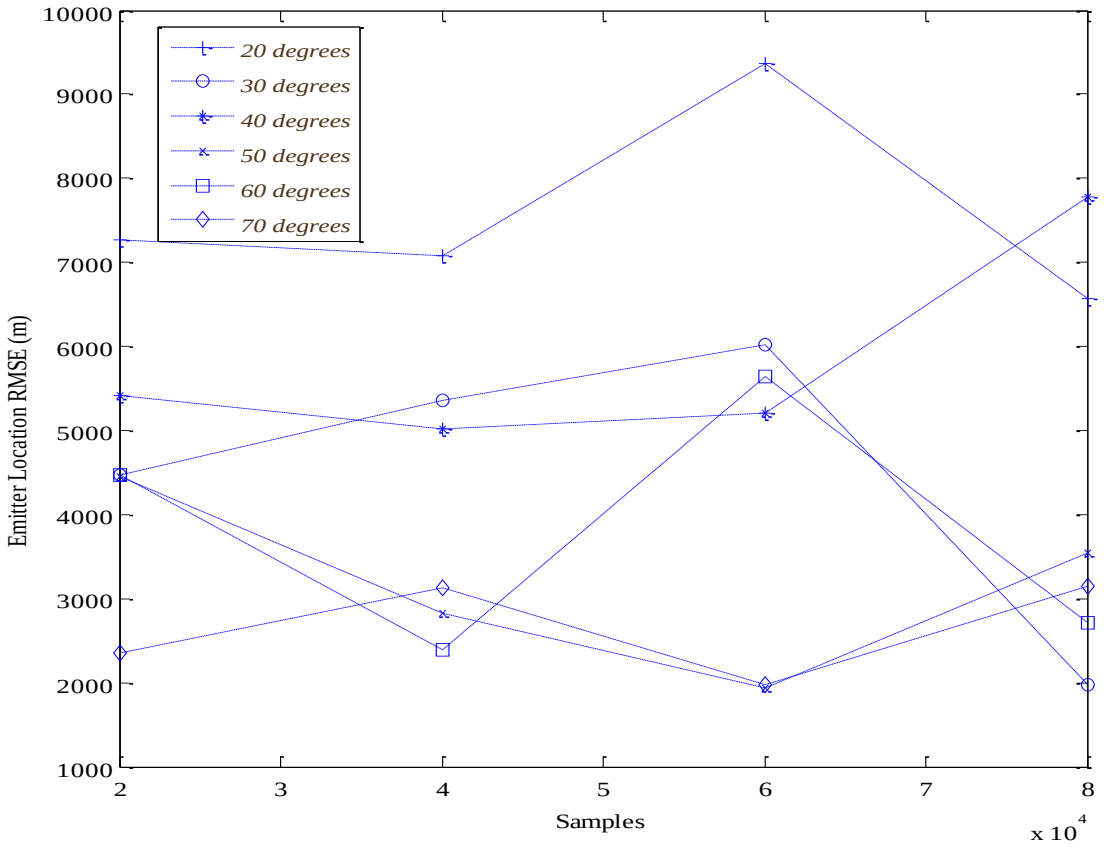

Figure 45. Emitter location RMSE is plotted against number of samples for two UAV sensors from twenty degrees to seventy degrees angular separation utilizing high noise interference.

The two-sensor model under high-noise interference maintains the overall trend of a slight increase in precision from 20,000 to 80,000 samples. The horizontal trend shows a general slight decrease in error over the whole sample period with the exceptions at 40 and 70 degrees. The maximum error is 9359 meters at 20 degrees separation using 60,000 samples, while the minimum error is 1945 meters using 60,000 samples. As in the satellite models, the noise injected into the model has increased errors by over 9000 meters and renders the model incapable of performing in high precision operations. In comparison, the emitter location RMSE is plotted against the number of samples across a range of angular spread for three UAV sensors in a high-noise environment, the results are shown in Figure 46.

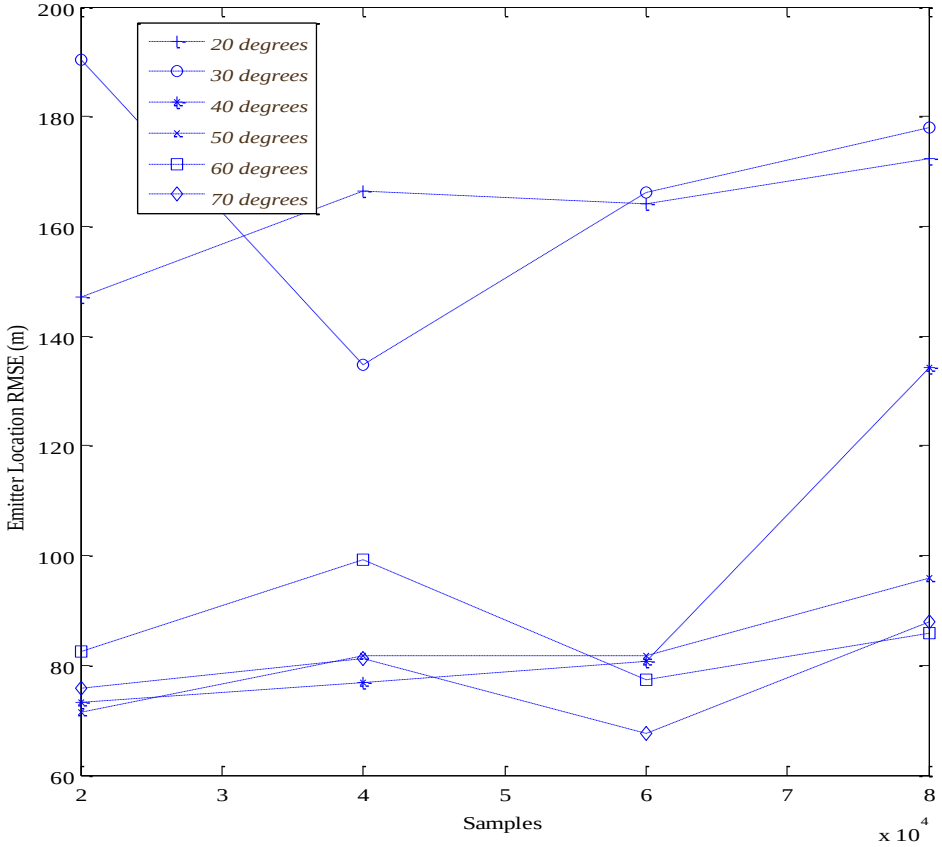

Figure 46. Emitter location RMSE is plotted against number of samples for three UAV sensors from twenty degrees to seventy degrees angular separation utilizing high-noise interference.

The vertical trend of the three-sensor model still shows a trend of increasing precision with an increase in angular separation; however, there is a larger gap between the lower angles of 20 and 30 degrees and the rest of the angles. The maximum error calculated is 190.4 meters at 30 degrees separation while the minimum error is 67.6 meters at 70 degrees separation. The three-sensor UAV model does not generally gain precision when the sample size is increased past 20,000 samples. This is due in part to the additional error of the third sensor calculated in the algorithm. The additive noise could be removed by adjusting the fusion from finding the centroidal point of three pairs of sensors to fusing three sensors and then estimating the error to the true emitter position. Next, we compare the two-sensor and three-sensor high-noise approaches in Figure 47 to gain a better understanding of the effects due to different separations.

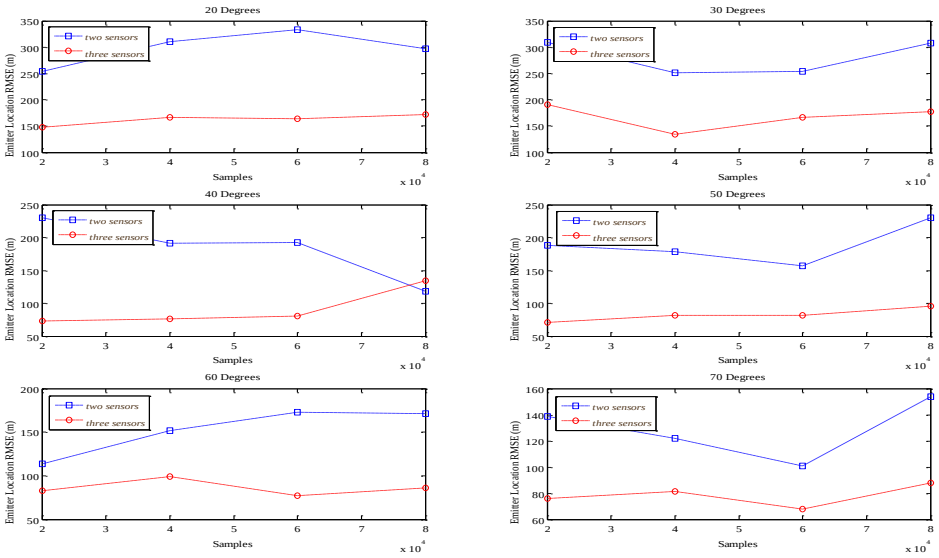

Figure 47. Emitter location RMSE is plotted against number of samples for two and three UAV sensors from twenty degrees to seventy degrees angular separation utilizing high-noise interference.

The three-sensor model significantly outperforms the two sensor model as the sample points are increased. In addition, at each angle, the three sensor approach greatly reduces the variability between angles providing a better geolocation precision as the UAV tracks across the operational area.

(3) Two versus Three UAV Sensors Low-Noise Comparison

In order to test the mitigation of this noise in our research, we set the standard deviation to one tenth of the value in the high-noise scenario. Emitter location RMSE is plotted against the number of samples across a range of angular spread for two UAV sensors and is shown in Figure 48. The lines between the points were not directly tested and are generated via linear interpolation.

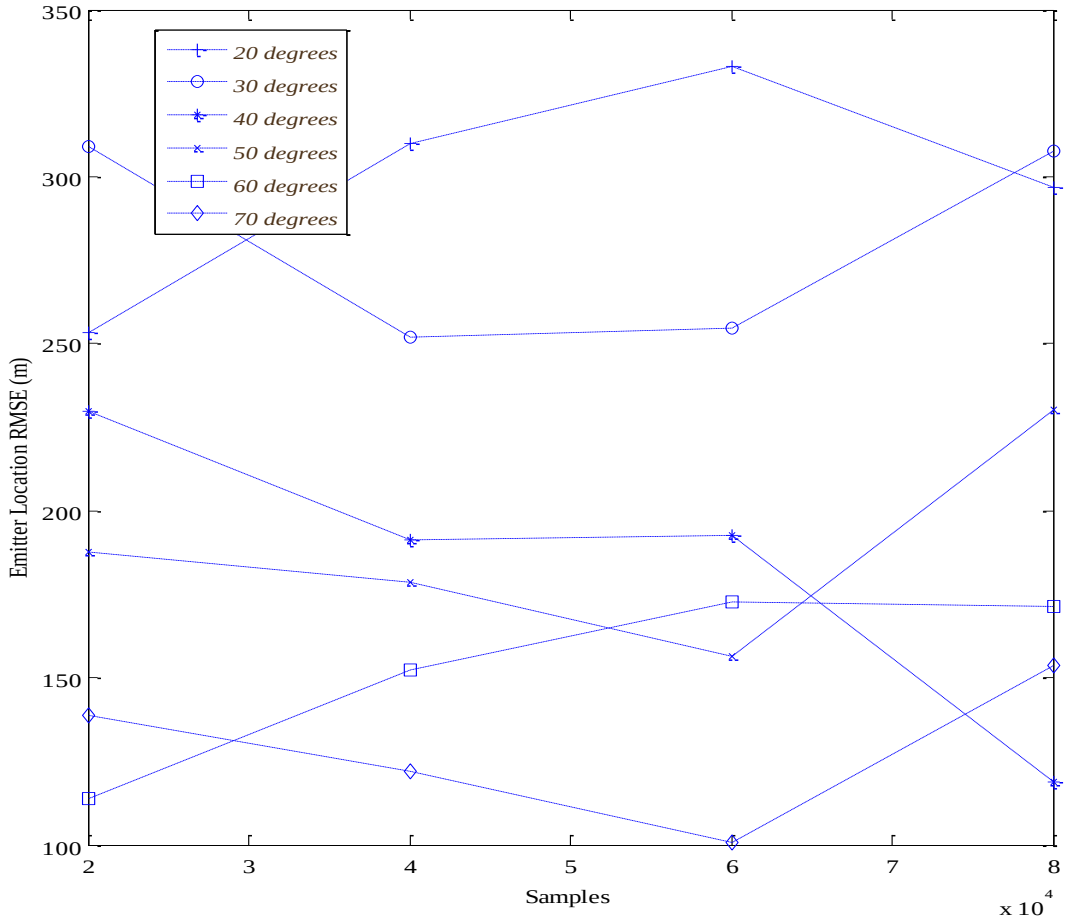

Figure 48. Emitter location RMSE is plotted against number of samples for two UAV sensors from twenty degrees to seventy degrees angular separation utilizing low-noise interference.

At each sample point in Figure 48, the degrees of separation create a vertical trend that shows an overall decrease in error from 20 degrees to 80 degrees. The most notable trend is a consistent increase in error at the low angles of 20 and 30 degrees compared to the improved precision from 40 to 70 degrees. Each degree of separation also creates a horizontal trend that shows a general increase of error as the angular separation increases. The exception is seen at 40 degrees where there is an optimal decrease in error. The three-sensor high-noise UAV model mirrors the satellite high-noise model in that neither can be used for high-precision operations. This reinforces the need for mitigation of noise effects. In comparison to the two-sensor model, the emitter location RMSE is plotted against the number of samples across a range of angular spread for three UAV sensors in a low-noise environment as shown in Figure 49.

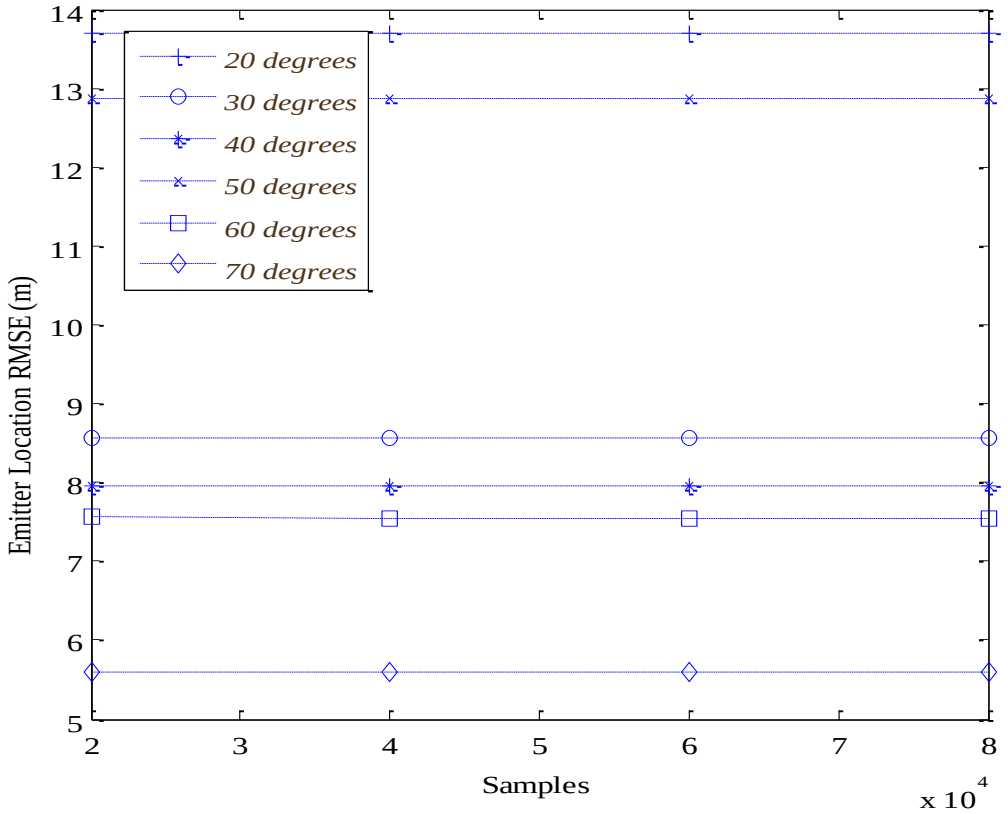

Figure 49. Emitter location RMSE is plotted against number of samples for three UAV sensors from twenty degrees to seventy degrees angular separation utilizing low-noise interference.

The three sensor model vertical trend shows a notable decrease in error from 20,000 to 80,000 samples; however, the horizontal trend shows only minute variability to the extent of 0.001 between sample points for any angle separation. Some of the variability across the sample period is lost as the odd sample points were not calculated. In addition, further research is required to fully understand this phenomenon. Despite the appearance in the lack of variation, the three sensor model had a significant increase in precision over the high noise scenario. Next, we compare the two-sensor and three-sensor high-noise approaches in Figure 50 in order to gain a better evaluation of the effects with respect to angular separation.

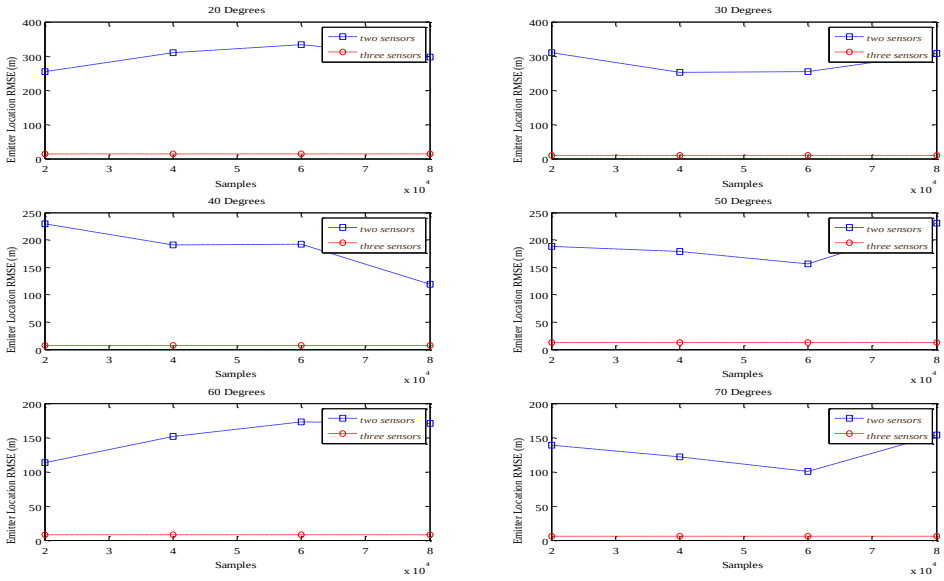

Figure 50. Emitter location RMSE is plotted against number of samples for two and three UAV sensors from twenty degrees to seventy degrees angular separation utilizing low-noise interference.

The three-sensor model consistently outperforms the two-sensor model. The maximum variation between the two-sensor and three-sensor models is 320 meters using 20 degrees of separation, while the minimum error decrease between the two models is 110 meters using a 40 degree angular separation. In addition, the lowest error recorded by the three-sensor model is 5.6 meters at 80 degrees of separation.

2. TOA Aperture Size

The definition of synthetic aperture for our research is the combination of data from multiple moving sensors. The aperture size is defined as the number of TOA solution circles combined to create a singular solution for the emitter; it is also referred to as the number of samples. The time between samples ΔT_{SA} is held constant in relation to the number of samples [12]. As the number of samples N increases, the time between the samples decreases. In the case of a single sample, one TOA solution circle is used to determine the location of the emitter. This is disadvantageous as the emitter could be located at any point on the circumference of the circle. For our research, we set a lower bound of $N > 2$ and varied the aperture size to a maximum value of fifty. In keeping with the research of [12], all applicable parameters are provided in Table 2.

Table 2. TOA algorithm parameters are given for the Synthetic Aperture size calculations.

Parameter (units)	Satellite Sensors	UAV Sensors
h (m)	19.10×10^{6}	3.048×10^{3}
ς (m/s)	3.889×10^{3}	51.44
α (degrees)	45	45
$N_{\max}$ (samples)	50	50
$N_{\min}$ (samples)	2	2
$\Delta T_{SA,\min}$ (s)	64.3	0.778
b (m)	1.750×10^{6}	280.1
$\sigma_{\tau H}$ (ns)	9.11	10.0
$\sigma_{\tau L}$ (ns)	0.911	1.0
$h_{\max}$ (m)	5000	1000

a. Two versus Three Satellite Sensors

(1) No-Noise Satellite Sensors

In order to test the TOA synthetic aperture algorithm's ability to process the geolocation data, two-sensor and three-sensor calculations were made without noise interference. This serves to create a baseline to which we can compare the high-noise and low-noise calculations provided later in following sections. Emitter location RMSE is plotted against synthetic aperture for two satellite sensors using no noise interference as shown in Figure 51.

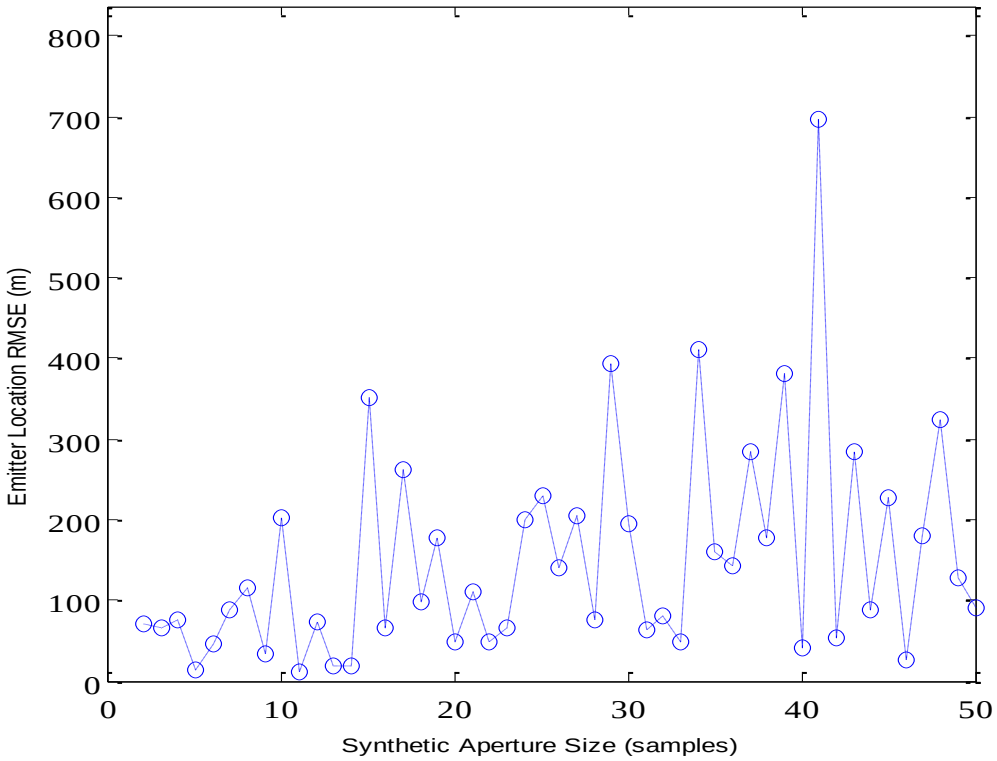

Figure 51. Emitter location RMSE is plotted against synthetic aperture for two satellite sensors using no noise interference.

Without any interference affecting the signal, lower aperture sizes produce lower errors than higher aperture sizes. At an aperture size equal to two, the RMSE error is 69.97 meters. Conversely, at a maximum aperture size equal to fifty, the RMSE error is

91.46 meters. Many factors such as sensor placement, variability in swath angle, and a limited number of sensors may be affecting the algorithms ability to derive a lower RMSE value. Further research is required to pinpoint these inaccuracies. In addition, we note the magnitude of the error varies widely over the sample set. The most consistent variability occurs during the aperture sizes of 36 to 46 where the algorithm alternates in a low-high-low pattern over the interval. The maximum error obtained across the entire aperture is 697 meters at an aperture size of 41, while the minimum error is 11.07 meters at an aperture size of 11. The utilization of an additional third sensor is tested where emitter location RMSE is plotted against synthetic aperture for three satellite sensors using no noise interference as shown in Figure 52.

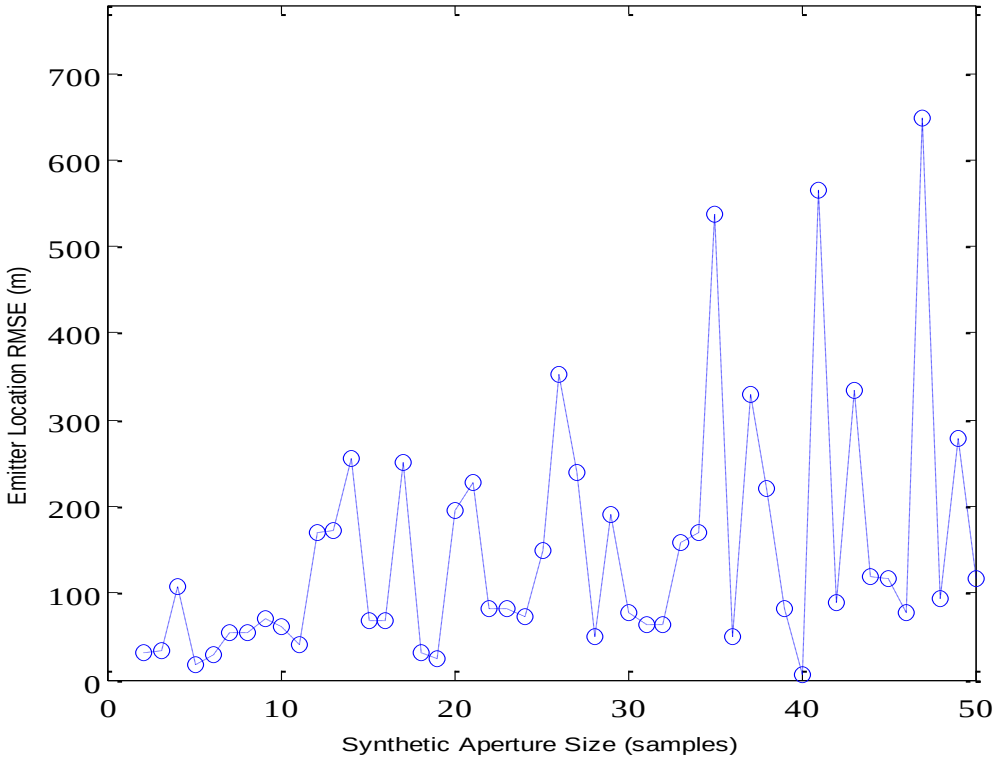

Figure 52. Emitter location RMSE is plotted against synthetic aperture for three satellite sensors using no noise interference.

The three-sensor synthetic aperture model follows the same trend as the two-sensor model with an increase in RMSE as the aperture size increases; however, the

variability has been slightly reduced as fewer peaks are present between aperture size values resulting in a more linear movement from the minimum to maximum aperture size. In addition, the additional sensor resulted in an insignificant improvement on the maximum and minimum RMSE values. The maximum RMSE value for three sensors is 697.5 meters, where the minimum value remains at 11.07 meters. This finding is important in that additional sensors should have resulted in a significant reduction in RMSE. Using the two and three sensor synthetic aperture calculations in a noise free environment as a baseline, we now present the performance of the algorithm under noisy conditions analogous to real-world operations.

(2) High Noise Satellite Sensors

Emitter location RMSE is plotted against synthetic aperture for two satellite sensors using high-noise interference as shown in Figure 53.

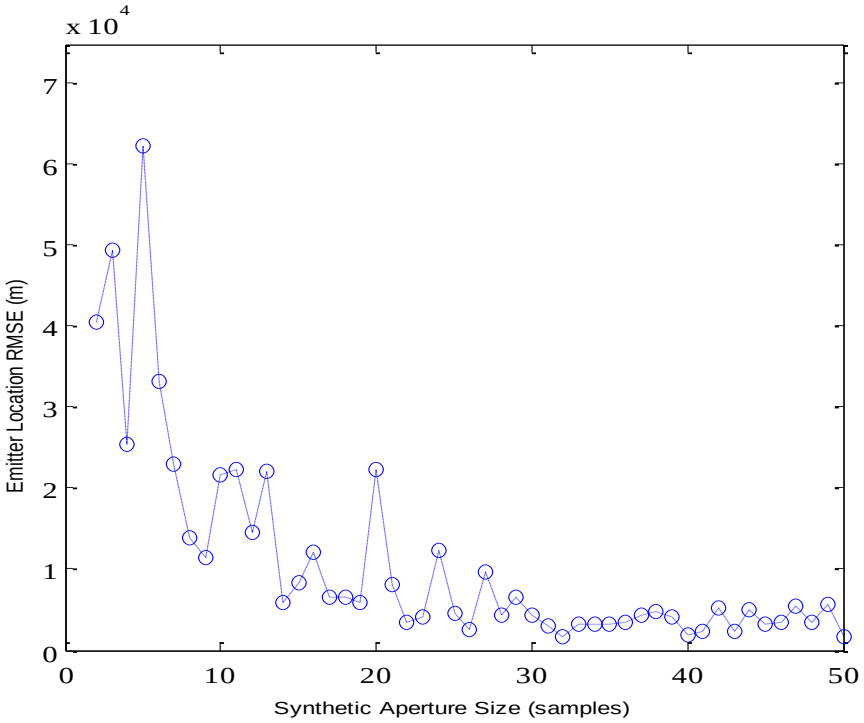

Figure 53. Emitter location RMSE is plotted against synthetic aperture for two satellite sensors using high-noise interference.

The large amplitude of the RMSE value for satellite sensors is continually present despite the type of testing performed. The presence of this error in the synthetic aperture calculations strengthens the need for previously mentioned mitigation techniques. The trend in the high-noise environment is ideally aligned to expectations where the increase of samples drives a lower RMSE value. There are two distinct sections within the curve. From an aperture size of two to approximately thirty-two, the RMSE value decreases rapidly from a maximum error of 6.239×10^4 meters to a minimum value of 2908 meters. Most increases of sample size result in a lower RMSE value. From an aperture size of thirty-four to fifty, the decreasing trend of RMSE values stagnates and results in variability centered around 3400 meters. The maximum value during this period is 5715 meters at an aperture size of forty-nine, while the absolute minimum value during this range is 1617 meters at an aperture size of fifty. Overall, the trend is promising where increasing the aperture size produces a lower RMSE value. Comparing the high-noise to the no-noise scenario, we see that the synthetic aperture algorithm appears to be dependent on noise to produce an optimal trend. Next, an additional third sensor is tested where emitter location RMSE is plotted against synthetic aperture for three satellite sensors using no-noise interference as shown in Figure 54.

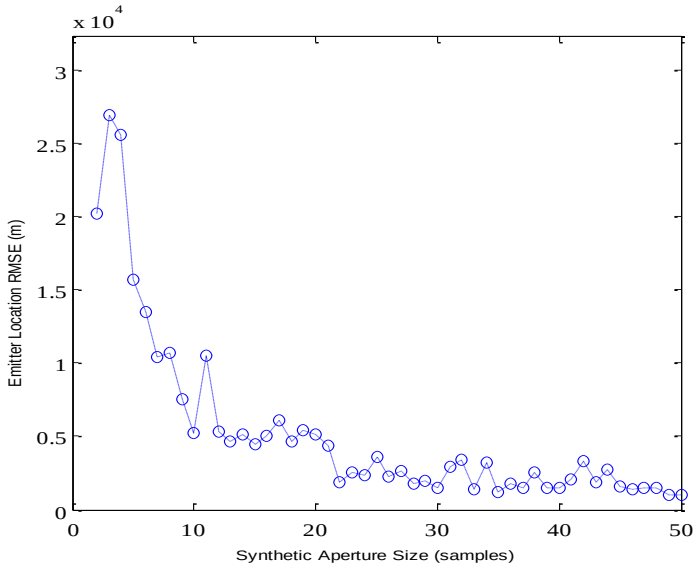

Figure 54. Emitter location RMSE is plotted against synthetic aperture for three satellite sensors using high-noise interference.

The third sensor not only decreases the overall RMSE from the two-sensor scenario but also refined the variability that was present. The maximum value is 2.962×10^{4} meters at an aperture size of three, while the absolute minimum value is 1035 meters at an aperture size of fifty. Unlike the two sensor model, RMSE decays rapidly, more like an exponential. Using two and three sensor synthetic aperture calculations for a high-noise environment, we now present the performance of the algorithm for low-noise conditions.

(3) Low-Noise Satellite Sensors

Emitter location RMSE is plotted against synthetic aperture for two satellite sensors using low-noise interference as shown in Figure 55.

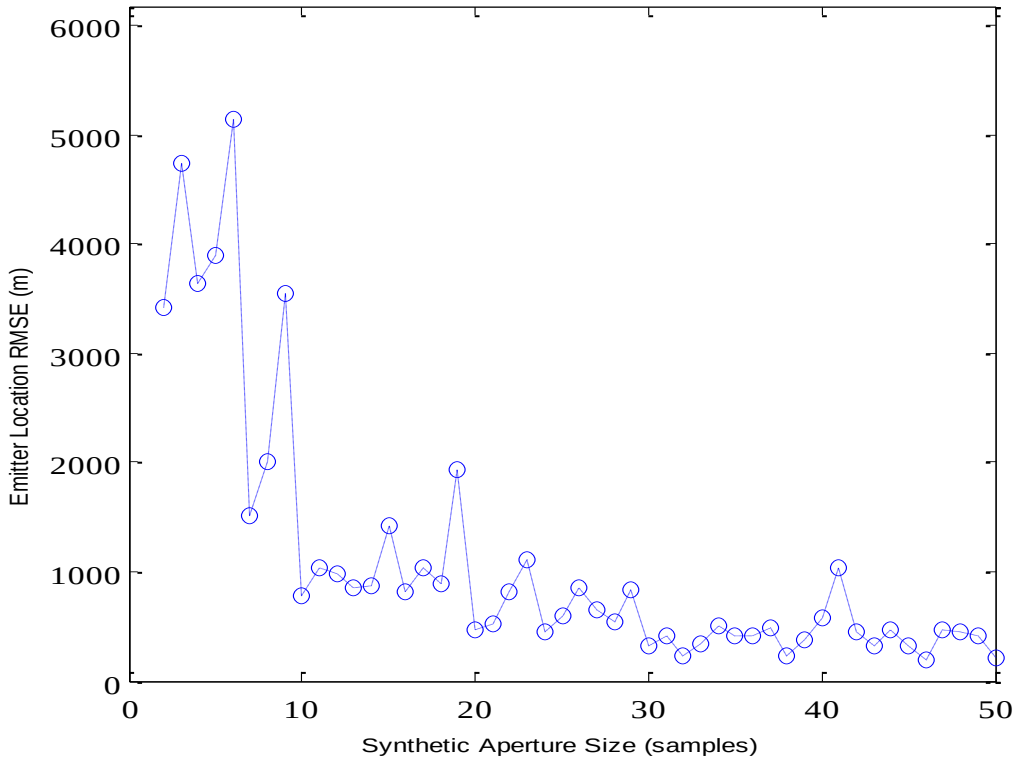

Figure 55. Emitter location RMSE is plotted against synthetic aperture for two satellite sensors using low-noise interference.

In a low-noise environment, the two-sensors model has a significant reduction in RMSE while maintaining the overall increasing emitter location precision when the aperture size is increased. The maximum value during this period is 5152 meters at an aperture size of six while the absolute minimum value during this range is 196 meters at an aperture size of forty-six. In addition, the reduction in noise created a more linear downward trend in location RMSE, removing the stagnation at an aperture size of 32 in the high-noise testing. Next, an additional third sensor is tested where emitter location RMSE is plotted against synthetic aperture for three satellite sensors using low-noise interference as shown in Figure 56.

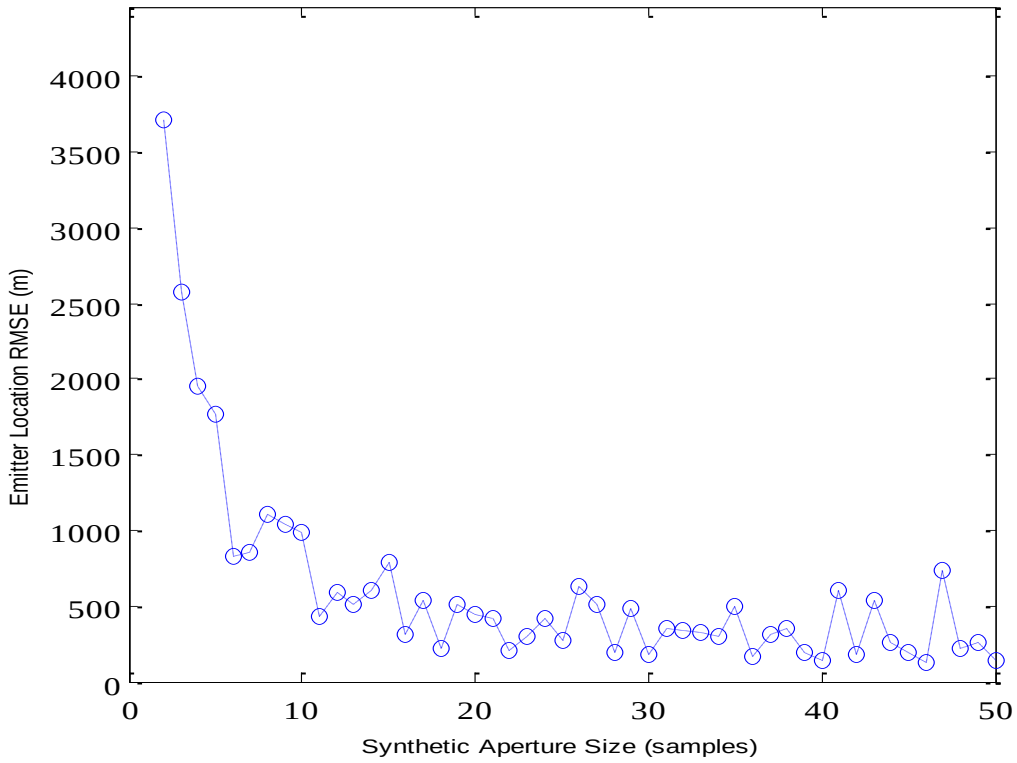

Figure 56. Emitter location RMSE is plotted against synthetic aperture for three satellite sensors using low-noise interference.

The three-sensor model in a low-noise environment shares the same trend as the two-sensor model. The major difference is that rapid RMSE decrease stops at an aperture size of six vice the aperture size of ten in the two-sensor model. The maximum value

during this period is 3137 meters at an aperture size of two; the absolute minimum value during this range is 123.9 meters at an aperture size of forty-six. While the results are an improvement over the two-sensor model, they still do not produce results for high precision use.

b. Two versus Three UAV Sensors

(1) No-Noise UAV Sensors

In order to test the TOA synthetic aperture algorithm's ability to process the geolocation data, two-sensor and three-sensor calculations at an altitude conducive to UAV operations were made without noise interference. This serves to create a baseline to which we can compare the high-noise and low-noise calculations provided in following sections. Emitter location RMSE is plotted against synthetic aperture for two UAV sensors using no-noise interference as shown in Figure 57.

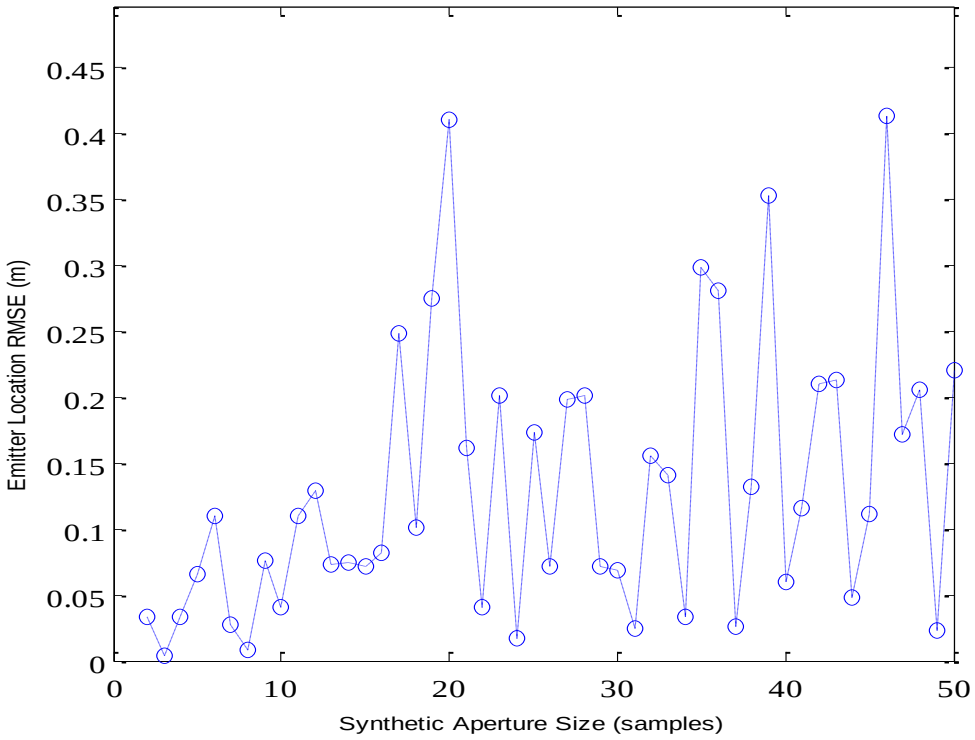

Figure 57. Emitter location RMSE is plotted against synthetic aperture for two UAV sensors using no-noise interference.

The two-sensor UAV model shares the same overall increasing RMSE trend as determined in the two-sensor satellite model. First, this is important as it reveals that the height of the sensor affects the overall RMSE. The lower elevation produces an enhanced position estimate of the emitter. This information can be used to find the most optimal positioning of the satellites for geolocation operations. Second, when the aperture size increased, the trends created by the algorithm remained the same between the test evaluated with satellites and UAVs. This confirms that changes to the fundamental calculations are necessary in order to decrease RMSE as the aperture size increases. The utilization of an additional third sensor is tested where emitter location RMSE is plotted against synthetic aperture for three UAV sensors using no noise interference, the results are shown in Figure 58.

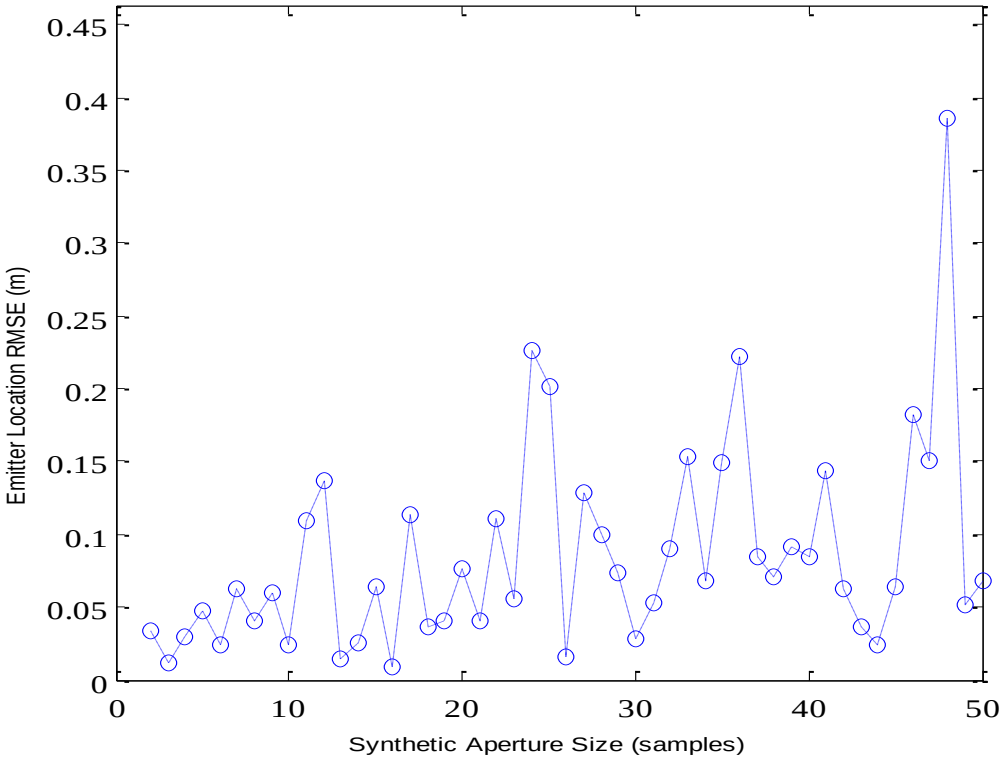

Figure 58. Emitter location RMSE is plotted against synthetic aperture for three UAV sensors using no noise interference.

The three UAV model shares the same trend as the three-sensor satellite model in an environment without interference. For brevity, the same recommendations for the two-sensor model are applied to the three-sensor model. Using the two-sensor and three-sensor synthetic aperture calculations in a noise free environment as a baseline, we now present the performance of the algorithm in noisy conditions analogous to real world operations.

(2) High-Noise UAV Sensors

Emitter location RMSE is plotted against synthetic aperture for two UAV sensors using high-noise interference as shown in Figure 59.

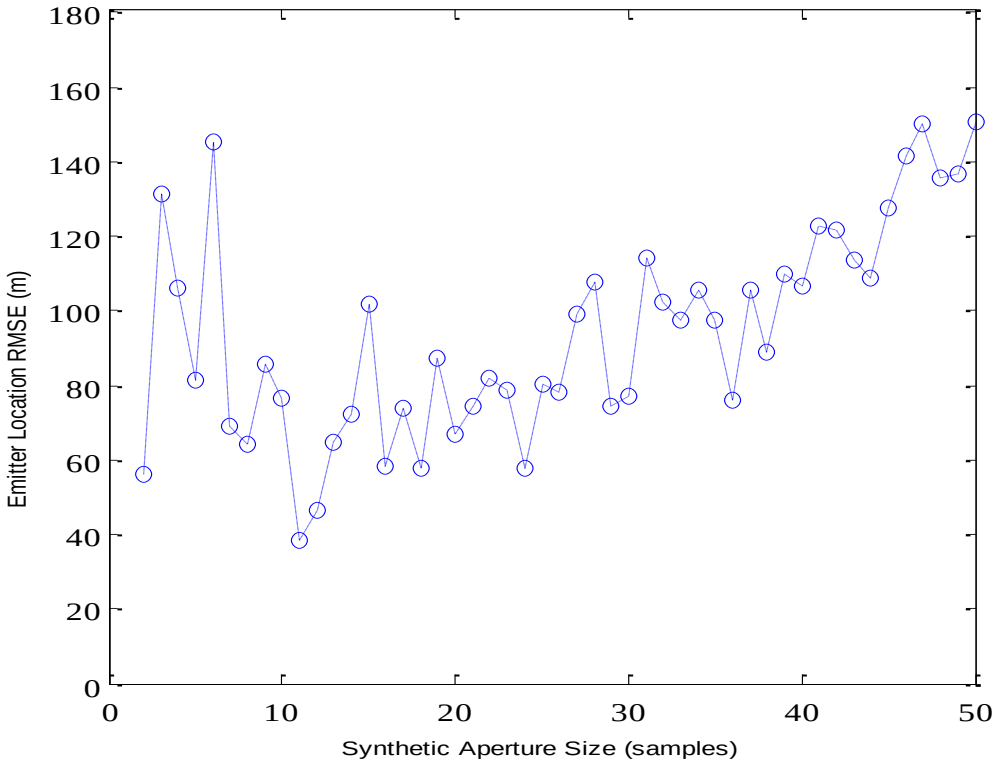

Figure 59. Emitter location RMSE is plotted against synthetic aperture for two UAV sensors using high-noise interference.

Unlike the high-noise satellite calculations, the two-sensor UAV calculations carry forward the overall upward trend of increasing RMSE with increased aperture;

however, there is a fluctuation of RMSE values at lower apertures before dropping down to a minimum value of 38.64 meters. This difference in trends between the satellite and UAV calculations may be solely dependent on altitude [12]. To test the hypothesis of [12], we plotted the emitter location RMSE against synthetic aperture for three UAV sensors using high-noise interference as shown in Figure 60.

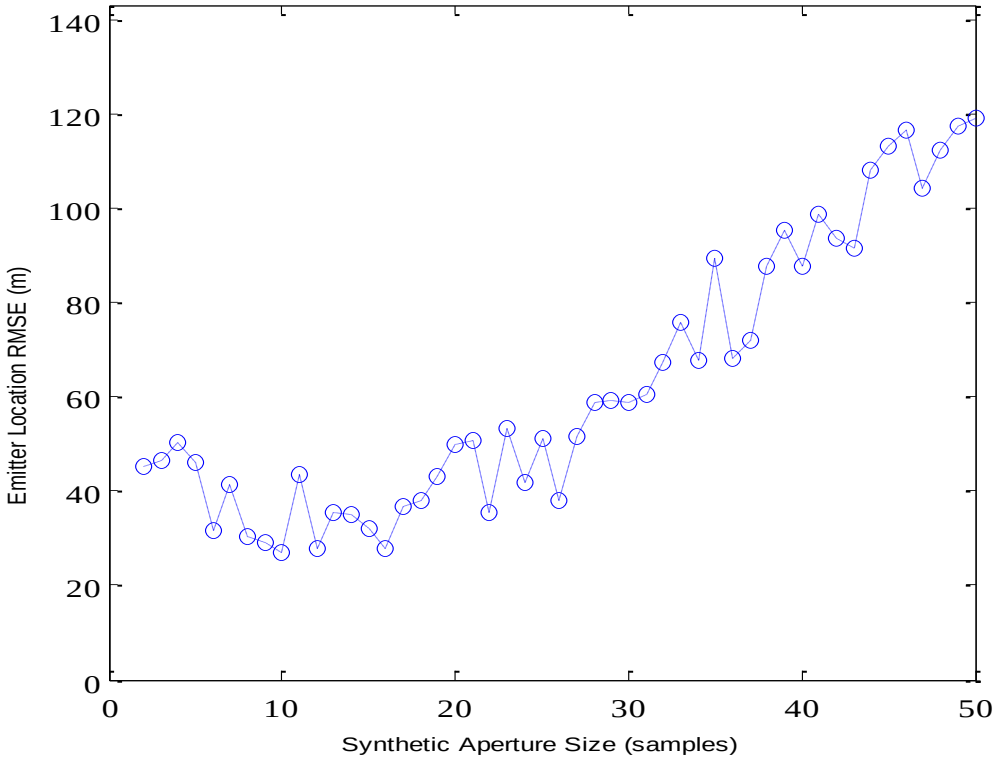

Figure 60. Emitter location RMSE is plotted against synthetic aperture for three UAV sensors using high-noise interference.

While the additional sensor decreases the overall RMSE, it does not affect the increasing trend. With all other variables held constant and only varying the number of sensors, it is likely that altitude is the limiting factor between the downward trend of the satellites and the upward trend of the UAVs. Further research is required to determine the crossover altitude between these trends. From the two-sensor and three-sensor synthetic aperture calculations in a high-noise environment, we now present the performance of the algorithm in low-noise conditions.

(3) Low-Noise UAV Sensors

Emitter location RMSE is plotted against synthetic aperture for two UAV sensors using low-noise interference as shown in Figure 61.

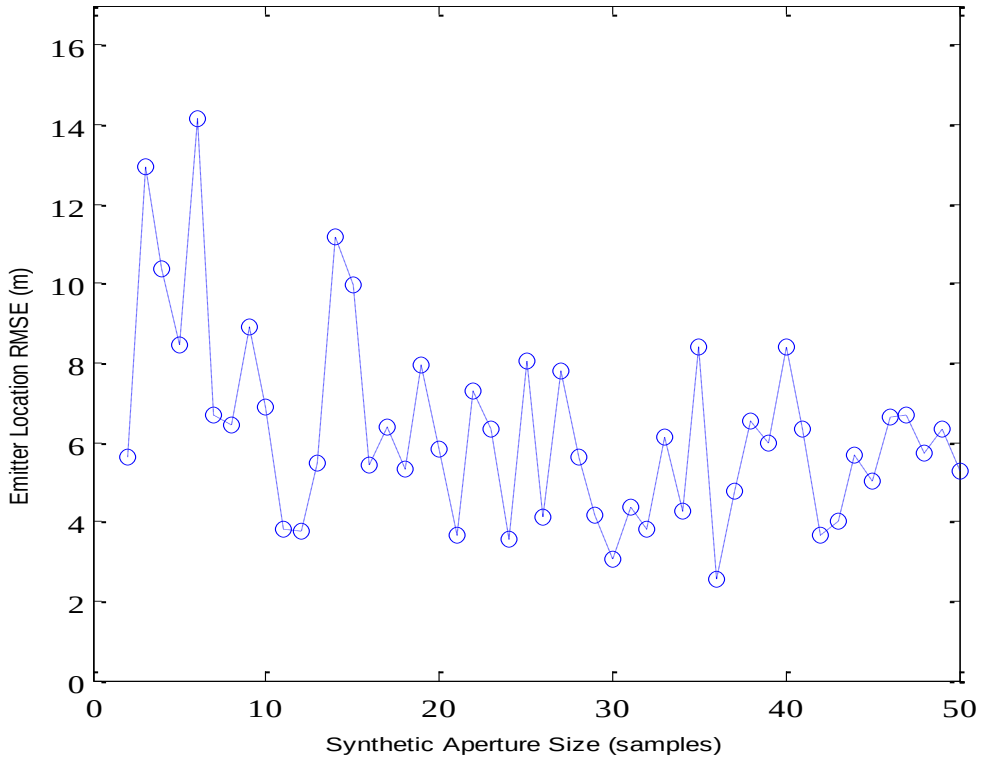

Figure 61. Emitter location RMSE is plotted against synthetic aperture for two UAV sensors using low-noise interference.

As the noise interference is reduced by ninety-percent, the median in the low-noise trend flattens out in RMSE of around 5.4 meters as the aperture size is increased. This significant shift from the high-noise condition reveals a noise dependency in the synthetic aperture algorithm. The baseline trend with no noise interference revealed the algorithm itself has an upward bias when the aperture size is increased. The difference between the high and low noise levels appears to indicate that there is a window of noise values in which the algorithm more correctly processes the geolocation data. Further research is required to indicate the lower and upper bound of this windowing effect and if

it is possible to find a range of noise values in which the algorithm process the geolocation data correctly. In order to test this hypothesis, we plotted the emitter location RMSE against synthetic aperture for three UAV sensors using low-noise interference as shown in Figure 62.

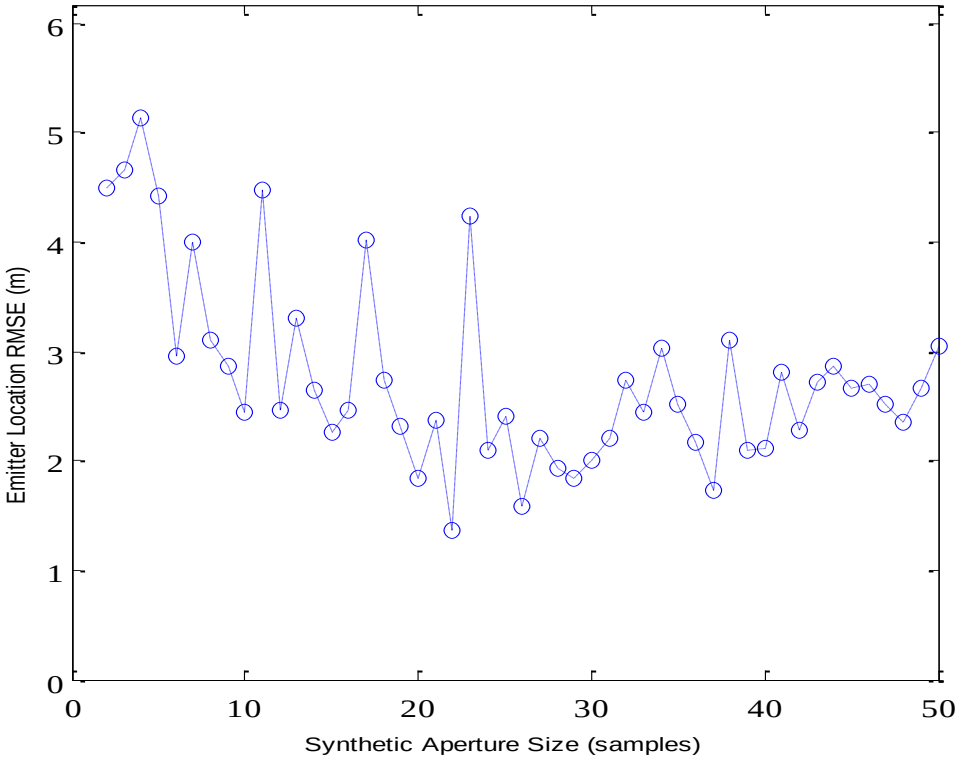

Figure 62. Emitter location RMSE is plotted against synthetic aperture for three UAV sensors using low-noise interference.

The additional sensor not only decreased the overall RMSE of the emitter's location, it also obtained a decreasing trend in RMSE as the synthetic aperture was increased. The RMSE at an aperture size of two is 4.494 meters, while at a maximum aperture size of fifty, the RMSE is 3.051 meters. The most accurate RMSE value recorded is 1.371 meters at an aperture size of twenty-two. These results confirm that there is a window of noise values in which the algorithm more correctly processes the geolocation data. By increasing the number of available sensors, a lower RMSE is possible.

D. SUMMARY

Overall, the three-sensor approach provided better geolocation precision than the two-sensor model. The evaluation of the no-noise environment for angular separation allowed for the algorithm of both the two and three sensors to be evaluated. Further adjustments to the geolocation algorithm are required to bring the overall RMSE below 10000 meters. In addition, the three-sensor fusion technique should be updated to fuse all three points at once and then evaluate the estimated position. The no-noise model for the synthetic aperture appeared to be noise dependent, creating an increasing RMSE value for increasing aperture size. The high-noise evaluation reflected the expected increase in geolocation error as given in Chapter V for both two-sensors and three-sensors. The angular spread satellite models revealed an increase in precision for the emitter geolocation estimate and removed a significant amount of the jitter for the three-sensor model. In addition, the comparison of the two and three sensor satellite and UAV models revealed altitude dependence in the algorithm where the overall RMSE trend shifts significantly due to the increase in noise interference. Mitigating the ionospheric noise for satellite and UAV sensors reduced overall RMSE values; however, it also revealed a noise dependence in the geolocation algorithm between the high and low noise models in relation to the no noise baseline and created a windowing effect allowing the correct RMSE trend only between certain values.

VII. SYNTHETIC APERTURE: TDOA-FDOA FUSION

A. SOLUTION STRATEGY

The TDOA-FDOA geolocation principles discussed in Chapters III and IV relinquish the simple TOA curve analysis for geolocation and rather incorporate a more analytically intensive combination of hyperboloid sheets and Doppler. While an analytic solution is possible, the work in [12] opted for an exhaustive search methodology to reduce complexity while maintaining the precision required for geolocation operations. That work is applied here and analyzed for performance versus a three-sensor model.

1. TDOA/FDOA Optimization

The TDOA-FDOA fusion technique developed by [12] develops a geolocation of the emitter's location based upon coordination between the bounding box principle and the discretization of samples within the bounding box volume. The aim of our research is to find the optimum intersection between bounding box size and the quantitative nature of the discretization in order to bring about the minimum RMSE value possible and extend the research to a three-sensor approach. From this measurement, the bounding box and discretization can be expanded to meet a wide range of operations while maintaining the proper ratio.

a. Bounding Box

In order to determine the emitter's location, we place a cube, also known as the bounding box, around the best estimate for the emitter $L(x_L, y_L, z_L)$ [12]. The cube's side length is equal to 2g where *g* is the side length of the bounding box, and every point within the volume of the cube represents a possible true location of the emitter as shown in Figure 63.

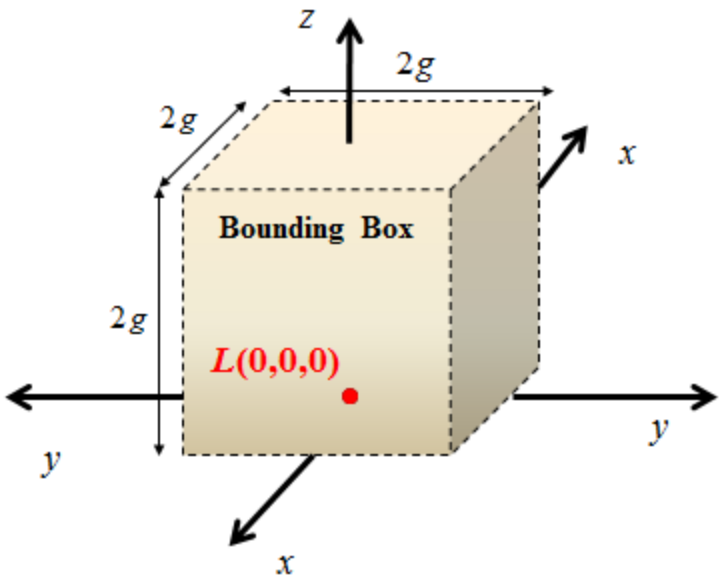

Figure 63. A bounding box surrounds the possible locations of the emitter.

b. Discretization Technique

In order to create a uniform search environment, Γ points are evenly mapped within the bounding box as denoted in [12] and spaced evenly at an interval of

$$\frac{2g}{\Gamma - 1}. \tag{97}$$

The total number of points within the box is Γ^3 [12].

2. TDOA and FDOA Metric

While the bounding box and discretization techniques are universal between the two-sensor and three-sensor approaches, modifications to the two-sensors approach from [12] for TDOA-FDOA fusion is necessary and changes are presented.

At time t_0, the algorithm begins to evaluate the estimated position calculated from sensors s_1, s_2, and s_3 at every point within the bounding box. With every time step, the points are evaluated. From these calculations, the four matrices created are a measured TDOA matrix M_T, a translated TDOA matrix $\tilde{M}_T$, as well as a measured

FDOA matrix M_F, and a translated FDOA matrix $\tilde{M}_F$ each with dimension $\Gamma \times \Gamma \times \Gamma$ [12]. Similar to TOA, the three sensors are grouped in pairs to geolocate the emitter. In the first iteration, sensors s_1 and s_2 begin to receive the beacon signal from the emitter and populate the measured TDOA matrix M_{T_q} for each point of the bounding box where q is the iteration index. The translated TDOA matrix $\tilde{M}_{T_q}$ is given by

$$\tilde{M}_{T_q}(i,j,k) = \exp\left[\frac{-\left(M_{T_q}(i,j,k)\right) - \tau_{31}\right)^2}{2\left(\sigma_{TDOA_q}\right)^2}\right] \tag{98}$$

where τ_{31} is the TDOA measurement from sensors s_3 and s_1. The term σ_{TDOAq} is given by

$$\sigma_{TDOA_q} = \left(\frac{[\max(M_{T_q}) - \min(M_{T_q})}{20}\right). \tag{99}$$

At the same time, when the measured and translated TDOA matrices are being determined, the algorithm calculates the measured and translated FDOA matrices. Sensors s_3 and s_1 populate the measured FDOA matrix M_{F_q}, while the translated FDOA matrix $\tilde{M}_{F_q}$ is given by

$$\tilde{M}_{F_q}(i,j,k) = \exp\left[\frac{-\left(M_{T_q}(i,j,k)\right) - \Delta f_{31}\right)^2}{2\left(\sigma_{FDOA_q}\right)^2}\right] \tag{100}$$

where Δf_{31} is the FDOA measurement from sensors s_1 and s_3. The term σ_{FDOA_q} is given by

$$\sigma_{FDOA_q} = \left(\frac{[\max(M_{F_q}) - \min(M_{F_q})}{20}\right). \tag{101}$$

The translated TDOA and FDOA matrices are fused into a combination matrix $\tilde{M}_{\lambda}$ for a corresponding time step λ and total time T [12]. The combination matrix is given as

$$\tilde{M}_q(i'_q, j'_q, k'_q) = \sum_{\lambda=1}^{T} \tilde{M}_{\lambda} = \sum_{\lambda=1}^{T} (\tilde{M}_{T_q,\lambda} + \tilde{M}_{F_q,\lambda}). \tag{102}$$

Once the combination matrix is calculated, the indices (i'_q, j'_q, k'_q) are the estimated emitter position indices (x'_q, y'_q, z'_q), which populate the iteration emitter position vector $\mathrm{r}''_{\mathrm{e}_q} = x'_q\,\hat{\mathrm{x}} + y'_q\,\hat{\mathrm{y}} + z'_q\,\hat{\mathrm{z}}$. In the second iteration, sensors s_2 and s_3 take the TDOA measurement τ_{23} as well as the FDOA measurement Δf_{23} and compute equations (98)-(102) resulting in the second emitter positon vector. In the third iteration, sensors s_1 and s_2 take the TDOA measurement τ_{21} as well as the FDOA measurement Δf_{21} and compute equations (98)-(102), resulting in the third emitter positon vector. The three emitter position vectors are combined through a centroid calculation to generate the total emitter positon vector given as

$$R'''_{\mathrm{eQ}} = \frac{1}{Q}\sum_{q=1}^{Q} \mathrm{r}''_{\mathrm{e}_q} \tag{103}$$

where Q is the total number of iterations. The goal of our research was to determine the optimum ratio between the number of TDOA/FDOA samples and the bounding box size. Utilizing three satellite sensors in a noiseless environment, we established an initial condition where the difference between the estimated and true emitter positon was zero. From this point, the number of samples *K* and bounding box size *g* were increased incrementally in order to test the algorithm. The optimum ratio was determined when increasing sample sizes for a given bounding box size failed to produce a lower RMSE value. The lowest combination of number of samples and bounding box size that resulted in a practical result is given by

$$\Re_O = \frac{K}{g} = \frac{5}{0.0055}. \tag{104}$$

3. RMS Error

In order to differentiate between the estimated positon and the true positon of the emitter for the TDOA-FDOA fusion, we calculate the RMSE based on Equations (89)-(91) in Chapter VI.

B. RESULTS

The work completed in this thesis for the TDOA-FDOA fusion synthetic aperture approach builds largely off the work accomplished in [12] where two satellite sensors attempted to geolocate an unknown sensor. We added a third sensor to the calculations and adjusted the calculations for the sensor placement as well as the bounding box versus discretization ratio.

The following scenario builds off the framework of Chapter VI. For the three sensor approach, an emitter e sends out a beacon signal from an unknown positon. The satellite sensors s_1, s_2, and s_3 are located at $(-100000-b,-b,h)$, $(-b,-b,h)$, and $(+100000-b,-b,h)$, respectively. The TDOA high noise $\sigma_{\tau H}$ and low noise $\sigma_{\tau L}$ conditions as well as the FDOA high noise $\sigma_{\delta fH}$ and low noise $\sigma_{\delta fL}$ conditions are defined in Chapter V. We retain the operating altitude for satellites at 19.1 km. Fusion of TDOA-FDOA with respect to sensor angular velocity spread is evaluated and presented in the following section.

Emitter location RMSE is plotted against increasing sample sizes used for TDOA-FDOA fusion with two and three satellite sensors with no noise interference. The angle and velocity calculations from Equations (92)-(96) of Chapter VI, Section 1 still hold valid. The list of parameters and their corresponding values in Table 3 were used to conduct the TDOA-FDOA angular velocity approach for satellite sensors.

Table 3. TDOA-FDOA fusion algorithm parameters are given for the TDOA-FDOA angular velocity spread calculations.

Parameter (units)	Satellite Sensors
h (m)	19.10×10^{6}
v_s (m/s)	3.889×10^{3}
α (degrees)	variable on [0,90]
N (samples)	5
ΔT_{SA} (s)	225
b (m)	1.750×10^{6}
$\sigma_{\tau H}$ (ns)	9.11
$\sigma_{\tau L}$ (ns)	0.911
$\sigma_{\delta fH}$ (Hz)	1.371
$\sigma_{\delta fL}$ (Hz)	0.1371
$L(x_L, y_L, z_L)$ (m)	$(0,0,0)$
g (m)	Variable on [5,20,40]
Γ (m)	Minimum value [.0055]

The aim of our research was to identify the optimal balance between the number of samples and the corresponding bounding box size in order to provide a foundation into the inner workings of the algorithm for future research. The noise-free environment allowed us the opportunity to test the algorithm without outside influence. The two-sensor TDOA-FDOA synthetic aperture calculations derived from [12] serve as the baseline for the comparison with the research completed in this thesis for the three-sensor approach. Emitter location RMSE is plotted against the number of samples for two and three satellite sensors from twenty degrees to seventy degrees angular separation utilizing no noise interference and is shown in Figure 64. Bounding box size was increased by a factor of $(2+\Delta)g$ where Δ is the size of the incremental step. The results for two and three sensor models are represented by a square and circle in Figure 64, respectively.

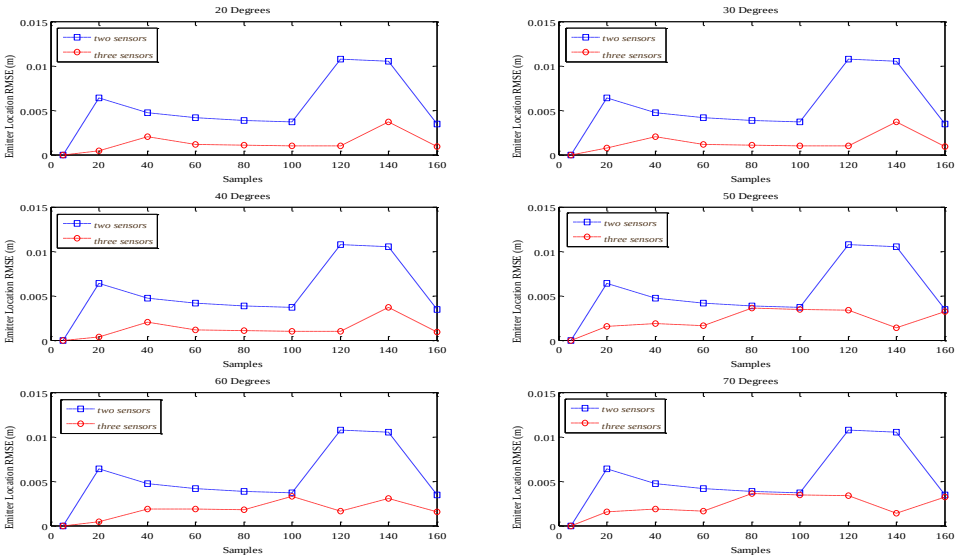

Figure 64. Emitter location RMSE is plotted against number of samples for two and three satellite sensors from twenty degrees to seventy degrees angular separation with no noise interference.

The three-sensor model has a lower overall RMSE across all separation angles over the two-sensor model with a 0.00284 meter advantage across twenty to forty separation angles and a 0.00915 meter advantage across the separation angles of forty to seventy between 120 and 140 samples. Four important results are derived from Figure 65. First, the bounding box methodology does not have a direct linearity between increasing size and higher RMSE. Instead, the optimum ratio of Equation (114) can provide a high-precision solution. Second, the computational times required to reach the upper bound of 160 samples for the two-sensor model took approximately eight hours, and the three sensor model took approximately 24 hours to obtain. This precludes the exhaustive search methodology from the use of high sampling in real-world applications. Third, in order for the optimum ratio to be used in real-world applications, a good estimated location of the emitter must be known prior to the beacon emanating the signal. Since many GPS devices are capable of transmitting on several wavelengths, information from cell towers, Wi-Fi, or other similar means can triangulate the coordinates of the emitter and transmit this information in the beacon signal to the sensors. Once the sensors receive this information, it is formatted into the variable $L(x_L, y_L, z_L)$, allowing for a smaller

sample size to derive a highly precise location. Lastly, additional sensors provide a better overall RMSE when all other factors are held constant for satellite sensors.

C. SUMMARY

Our results suggest that the TDOA-FDOA method can provide superior results in comparison to TOA while utilizing the optimum bounding box-to-sample size ratio. In addition, an exhaustive search methodology is a viable option with the inclusion of a priori information sent from the emitter to the sensor in the beacon symbol. This precludes a large sample size requirement for larger bounding boxes that cause sampling times to rise to limits that prevent its use in real-world satellite operations. Additionally, the results validate that a wide range of angular velocities do not inhibit the precision of the three-sensor model and allow for optimum geolocation results despite the satellite's location at the time of receipt of the signal.

VIII. CONCLUSION

A. RESEARCH CONTRIBUTIONS

The initial goals of this research focused on three main areas. First, we investigated the accuracy of a three-sensor synthetic aperture model in comparison to previous research utilizing a two-sensor approach measuring time-of-arrival, time-difference-of-arrival, and frequency-difference-of arrival geolocation estimates. We predicted that the addition of a third sensor would decrease the geolocation error over the two-sensor model when tested for satellite and UAV sensors. In order to lay a foundation for this prediction, we brought forth from literature the governing equations as well as the relevant two-dimensional and three-dimensional solutions in conjunction with geolocation principles and examples. Next, we laid the foundation of signal interference and mitigation techniques in the ionosphere and troposphere. In addition, we specified the noise factors and noise models that are imperative to provide accurate geolocation estimates. These regions corresponded to the intended testing altitudes for satellite and UAV geolocation. Finally, we investigated the TDOA-FDOA fusion algorithm to determine the optimum configuration of parameters that would result in the lowest possible geolocation estimate.

The synthetic aperture three-sensor model utilizing TOA geolocation outperformed the two-sensor model with a lower overall RMS error; however, the application of three satellite sensors still provided RMS error values that preclude its use in high-precision operations. In our research, three pairs of geolocation estimates at each time step were created and combined via a centroid function to test the estimated position from the actual location. It is possible to adjust the three-sensor algorithm to calculate the position estimate from all three satellites at each time step instead of utilizing three pairs of two sensors and then finding the centroid point at each time step. This may further decrease the RMS error. The utilization of three UAV sensors provided not only better geolocation estimates than the two-sensor version but also produced results that can be used in operations where precision is crucial to the success of the mission. A main discovery within the TOA algorithm was that while increasing the sample size produced

lower RMS error values, the computational time to meet these demands precluded their use in real-world, time-sensitive operations.

The investigation into the various signal interferences in the ionosphere for satellite sensors and troposphere for UAV sensors laid the groundwork for future research. Once adjustments to the TOA, TDOA, and FDOA algorithms have been made to lower the overall RMS error, the mitigation techniques outlined in our research allows the transition from a purely theoretical framework to one that more closely resembles real-world operations. In addition, our noise modeling research provides the basis to implement real-time integration of noise sensing and mitigation techniques. This allows a superior advantage to synthetic aperture methods that currently exist.

The optimization of the TDOA-FDOA fusion algorithm was essential to prove that the algorithm was capable of high precision geolocation as well as demonstrate that large sample testing generated a trend of lowering RMS values for the three-sensor approach. The accuracy for the three-sensor approach outperformed the two-sensor approach. Moreover, the optimized ratio determined through an exhaustive search methodology provided high precision resolution across all utilized sample points and decreased RMSE as the sample size was increased. In order for this precision to be implemented in real-world operations, a priori emitter location information must be provided in the beacon signal.

Overall, additional sensors as well as the larger sample points in geolocation provide lowered RMSE at the cost of computation time. The UAV implementation of the synthetic aperture TOA algorithm is already suited for future testing. The satellite synthetic aperture TOA algorithm as well as the TDOA-FDOA fusion algorithm requires future research to lower RMS values to include their use in real-world operations.

B. OPPORTUNITIES FOR FUTURE WORK

The future work on the three-sensor synthetic aperture geolocation scenario can be broken down into four main areas that deliver the greatest impact based on previous research and testing. First, noise affecting the signal as well as the corresponding mitigation requires real-time dynamic inputs to ensure the highest possible precision is

accomplished. Second, the synthetic aperture TDOA-FDOA fusion algorithm needs to be adjusted to allow for both larger bounding box sizes a priori emitter geolocation position information. Third, the synthetic aperture TOA and TDOA-FDOA fusion algorithms require automation of environmental inputs to ensure that the most accurate information is provided to the geolocation calculations. Lastly, high speed computing is required to significantly reduce computation times.

1. Noise Effects and Mitigation

A dynamic approach to model the interference a signal interacts with in real-world observations is needed. The synthetic aperture model by definition requires the movement of the sensors across a fixed distance. This movement can acquire differing values of interference based on changes in latitude, longitude, space weather, and time-of-operations. Accounting for these variations allows for a more precise geolocation estimate. Also, more accurate and timely atmospheric calculations allow for a more precise geolocation estimate.

2. Bounding Box and Discretization Technique

Our research showed the current bounding box algorithm is capable of high-precision geolocation. Future research should continue to refine these results across a wider range of bounding box sizes as well as reduce the computational requirements in the calculations to minimize the time delay while maintaining the highest possible precision in emitter geolocation. Future changes should incorporate techniques to sequentially decrease the bounding box size with each additional time step as well as research the benefit in providing a priori emitter location information in the beacon signal.

3. Automation

Our current research employed a pre-calculated atmospheric noise value based on historic collection. Due to the dynamic nature of the atmospheric effects on the signal as it traverses from the emitter to the respective sensor, automating the input of the noise variables allows for a more timely calculation and mitigation thereby reducing the

overall computation of the TOA and TDOA-FDOA fusion geolocation. To accomplish this task, a new model must be created that allows for either the collection of real-time atmospheric data or the cataloging of modeled data in a way that propagates this information to a central processing center or the sensors for use in mitigation calculations.

4. High-speed Computing

One major limitation that permutated through each section of our research was a high computation time associated with increasing sample sizes inputted into the geolocation algorithm. This limitation can be mitigated through the use of a platform that incorporates higher speed computing. To aid future research in this endeavor, the synthetic aperture TOA and TDOA-FDOA fusion algorithms require optimization for processing in a high-speed computing laboratory. Through additional processing speed, the true upper bound of sampling can be obtained as well as the possibility for real-time geolocation to come to fruition.

LIST OF REFERENCES

[1] G. Fuller and K. Horton, "Protecting GPS availability from EMI," in *Digital Avionics System Conference,* Philadelphia, PA, 2000, pp. 21–27.

[2] B. Aktug, O. Lenk, M. Kurt, E. Parmaksiz, and S. Ozdemir, "Space weather activities of IONOLAB group using TNPGN GPS Network," in *5th International Conference on Recent Advances in Space Technologies,* Istanbul, 2011, pp. 604–607.

[3] M. Bogens, M. Durfee, L. Gardner, and R. Streeper, "Basic Land Navigation," National Wildfire Coordinating Group, Boise, ID, Rep. PMS 475, June 2007.

[4] P. Daly, "Navstar GPS and GLONASS: Global Satellite Navigation Systems," *Electronic & Communication Engineering Journal,* vol. 5, pp. 349–357, Dec. 1993.

[5] J. Shen and A. F. Molisch, "Accurate passive location estimation using TOA measurements," *IEEE Transactions on Wireless Communications,* vol. 11, pp. 2182–2192, June 2012.

[6] X. Yanrong, L. Xiaohue, X. Longxia, and R. Ye, "Research on position differential method of dual-satellites TDOA and FDOA in passive location system," in *IEEE International Frequency Control Symposium,* Baltimore, MD, 2012, pp. 1–5.

[7] R. Bajaj, S. Ranaweera, and D. Agrawal, "GPS: Location-tracking technology," *Computer,* vol. 35, pp. 92–94, Apr. 2002.

[8] B. M. Hannah, "Modelling and simulation of GPS multipath propagation," Ph.D. dissertation, Queensland University of Technology, Brisbane, Queensland, 2001.

[9] C. Gentile and R. Raulefs, *Geolocation Techniques: Principles and Applications.* New York, NY: Springer, 2013, pp. 18–22.

[10] S. Mirchandani, C. Rawat, A. Krishnan, A. Agarwal, G. Isola, and V. Sivaprasad, "Maximum likelihood angle of arrival estimation using least mean squares technique," in *International Conference on Emerging trends in Robotics and Communication Technologies,* Chennai, 2010, pp. 129–132.

[11] G. Welch and G. Bishop, "An introduction to the Kalman filter," unpublished.

[12] K. Elam, "Two-sensor synthetic aperture geolocation techniques," M.S. thesis, Naval Postgraduate School, Monterey, CA, 2014.

[13] S. A. Zekavat and R. M. Buehrer, Eds, *Handbook of Position Location: Theory, Practice, and Advances.* Hoboken, NJ: John Wiley & Sons, 2012.

[14] R. Kaune, "Performance analysis of passive emitter tracking using TDOA, AOA, and FDOA measurements," in *Society for Computer Science,* Leipzig, 2010, pp. 838–843.

[15] W. S. Rickman, (2014, Sept. 09).*Proofs for Hyperbola* [Online]. Available: http://www2.seminolestate.edu/srickman/Proofs/Proofs%20for%20the%20hyperbola.pdf.

[16] J. V. Hernandez, "The significance of passive acoustic array-configurations on sperm whale range estimation when using the hyperbolic algorithm," Ph.D. dissertation, Heriot-Watt University, Edinburgh, Scotland, UK, 2009.

[17] R. J. Ulman and E. Gerantiotis, "Motion detection using TDOA and FDOA measurements," *IEEE Transactions on Aerospace and Electronic Systems,* vol. 37, pp. 759–764, Apr. 2001.

[18] J. Yuanwei, N. Donoughue, and J. Moura, "Position location by time reversal in communication networks," in *IEEE International Conference on Acoustics, Speech and Signal Processing,* Las Vegas, NV, 2008, pp. 3001–3004.

[19] M. Karatas, "A multi foci closed curve: Cassini oval, its properties and applications," *Dogus University Journal*, vol. 14, pp. 231–248, July 2013.

[20] W. Wang and X. Zou, "A novel analysis method for broadband noise signal," in *International Workshop on Intelligent Systems and Applications,* Wuhan, 2009, pp. 1–3.

[21] R. Langley, (1997, June).*GPS Receiver System Noise* [Online]. Available: http://gauss.gge.unb.ca/papers.pdf/gpsworld.june1997.pdf.

[22] NASA, (2014, Oct. 25).*Earth's Atmospheric Layers* [Online]. Available: http://www.nasa.gov/content/earths-atmospheric-layers/#.VEwIDvnF91Z.

[23] J. A. Klobuchar, (1991, Apr.) *Ionospheric Effects on GPS* [Online]. Available: http://gauss.gge.unb.ca/gpsworld/EarlyInnovationColumns/Innov.1991.04.pdf.

[24] C.O. Andrei and C. Ruizhi, "Tropospheric delay estimation based on numerical weather model," *REVCAD Journal of Geodesy and Cadastre*, pp. 87–94, July 2007.

[25] M. Bevis, S. Businger, T. Herring, C. Rocken, R. Anthes, and R. Ware, "GPS meteorology: Remote sensing of atmospheric water vapor using the Global Positioning System," *Journal of Geophysical Research,* vol. 97, pp. 15787-15801, Oct. 1992.

[26] T. Schuler, "On ground based GPS: Tropospheric delay estimation," Ph.D. dissertation, Bundeswehr University, Munich, 2001.

[27] A. Niell, "The IMF mapping functions," in *GPSMet Workshop,* 2003, pp. 1–10.

[28] F. S. Solheim and J. Vivekanandan, "Propagation delays induced in GPS signals by dry air, water vapor, hydrometers, and other particles," *Journal of Geophysical Research*, vol. 104, pp. 9663–9670, Apr. 1999.

[29] FYS3610. Class Lecture, Topic: "Chapter 3-The middle and upper atmosphere." Department of Physics, University of Oslo, Oslo, Norway, 2004.

[30] FYS3610. Class Lecture, Topic: "Chapter 4-The ionosphere." Department of Physics, University of Oslo, Oslo, Norway, 2004.

[31] J.A. Shim, "Analysis of Total Electron Content (TEC) variations in the low-and middle-latitude ionosphere," Ph.D. dissertation, Utah State University, Logan, UT, 2009.

[32] A.M. Hamad, "Estimation of the parameter of an exponential distribution when applying maximum likelihood and probability plot methods using simulation," *Ibn Al-Haitham Journal for Pure and Applied Science*, vol. 25, pp. 1–10, Oct. 2012.

[33] A.A. Giordano and F. Haber, "Modeling of atmospheric noise," *Radio Science*, vol. 7, pp. 1011–1023, Nov. 1972.

[34] H.J. Larson, *Introduction to the Theory of Statistics*. New York, NY: John Wiley & Sons, 1973.

[35] K.-W. Chiang, W-C. Peng, Y-H. Yeh, and K-H. Chen, "Study of alternative GPS network meteorological sensors in Taiwan: Case studies of the Plum rains and typhoon Sinlaku," *Sensors*, vol. 9, pp. 5001–5021, June 2009.

[36] V.B. Mendes and R.B. Langley, "Tropospheric zenith delay prediction accuracy for airborne GPS high-precision positioning," in *Proceedings of the 54th Annual Meeting of the Institute of Navigation,* Denver, CO, 1998, pp. 337–347.

[37] A. Leick, *GPS Satellite Surveying.* New York, NY: John Wiley & Sons, 2003.

[38] I. Sanlioglu and M. Zeybek, "Investigation on GPS heighting accuracy with use of tropospheric models in commercial GPS softwares for different heights," in *FIG Working Week*, Rome, Italy, 2012, pp. 1–15.

[39] R. Eresmaa and H. Jarvinen, "An observation operator for ground-based GPS slant delays," *Tellus,* vol. 58, pp. 131–140, 2006.

[40] T. Kos, M. Botincan, and A. Dlesk, “Mitigating GNSS positioning errors due to atmospheric signal delays,” *Pomorstvo Journal of Maritime Studies,* vol. 23, pp. 495–513, Dec. 2009.

[41] Y.D. Opaluwa, Q.A. Adejare, Z.A. Suleyman, I.C. Abazu, T.O. Adawale, A.O. Odesanmi, and V.C. Okorocha, “Comparative analysis of five standard dry tropospheric delay models for estimation of dry tropospheric delay in GNSS positioning,” *American Journal of Geographic Information System,* vol. 2, pp. 121–131, 2013.

[42] A. E. Niell, “Global mapping functions for the atmosphere delay at radio wavelengths,” *Journal of Geophysical Research,* vol. 101, pp. 3227–3246, Feb. 1996.

[43] J. W. Marini, “Correction of satellite tracking data for an arbitrary tropospheric profile,” *Radio Science,* vol. 7, pp. 223–231, Feb. 1972.

[44] J.L. Davis and T.A. Herring, “Geodesy by radio interferometry: Effects of atmospheric modeling errors on estimates of baseline length,” *Radio Science,* vol. 20, pp. 1593–1607, Nov.-Dec. 1985.

[45] J.C. de Munck and T.A.TH. Spoelstra, *Refraction of Transatmospheric Signals in Geodesy: Proceedings of the Symposium.* Delft. Netherlands: Nederlandse Commissie Voor Geodesie, 1992.

[46] R.B. Seidensticker, “Continued fractions for high-speed and high-accuracy computer arithmetic,” in *6th Symposium on Computer Arithmetic,* Aarhus, Denmark, 1983, pp. 184–193.

[47] J. Zhang, “Investigations into the estimation of residual tropospheric delays in a GPS network,” M.S. thesis, University of Calgary, Calgary, Alberta, Canada, 1999.

[48] M. Mainul Hoque and Norbert Jakowski. (2012). *Global Navigation Satellite Systems: Signal, Theory and Applications* [Ebrary version]. [Online] Available: http://www.intechopen.com/books/global-navigation-satellite-systems-signal-theory-andapplications/ionospheric-propagation-effects-on-gnss-signals-and-new-correction-approaches.

[49] D. Anderson and T. Fuller-Rowell, “The Ionosphere,” NOAA, Boulder, CO, Rep. SE-14, 1999.

[50] Y.T. Morton, F.V. Graas, Q. Zhou, and J. Herdtner, “Assessment of the higher order ionosphere error on position systems,” Navigation: Journal of The Institute of Navigation, vol. 56, pp. 185–193, May 2009.

[51] M.M. Alizadeh, D.D. Wijaya, T. Hobiger, R. Weber, and H. Schuh, (2013). Ionospheric effects on microwave signals, *Atmospheric Effects in Space Geodesy*, J. Bohm and H. Schuh (Ed.), ISBN: 978–3642369315, Springer, 35–45.

[52] About ionopsheric scintillation, Australian Government Bureau of Meteorology, [Online]. Available: http://www.ips.gov.au/Satellite/6/3. (Accessed: 2014 Nov. 04)

[53] R. Romero, "Effect of interference in the calculation of the amplitude scintillation index S4," in International Conference on localization and GNSS, Turin, 2013, pp. 1–6.

[54] T.E. Humphreys, M.L. Psiaki, J.C. Hinks, B. O'Hanlon, and P.M. Kintner, "Simulating ionosphere-induced scintillation for testing GPS receiver phase tracking loops," IEEE Journal of Selected Topics in Signal Processing, vol. 3, pp. 707–715, Aug. 2009.

[55] P.W. Ward, J.W. Betz, and C.J. Hegarty, "Satellite signal acquisition, tracking, and data demodulation," in *Understanding GPS: Principles and Applications*, 2nd ed., E.D. Kaplan, Ed.: Artech House, 2005, pp. 153–241.

[56] P.M. Kintner, B.M. Ledvina, and E.R. DePaula, "GPS and ionospheric scintillations," Space Weather, vol. 5, pp. 1–23, Sept. 2007.

[57] A.D. Schmidt, "Radar imaging of satellites at meter wavelengths," Ph.D. dissertation, Stanford University, Palo Alto, CA, 1999.

[58] C.N. Mitchell, (2014, Nov. 04).Multi-instrument data analysis system [Online]. Available: http://people.bath.ac.uk/eescnm/midas.htm.

[59] Y. Xia, L. Jiangchen, and Z. Shoujian, "Ionopsheric correction for spaceborne single-frequency GPS based on single layer model," Journal of Earth System Science, vol. 123, pp. 767–778, Jun. 2014.

[60] R.E. Daniell Jr, L.D. Brown, D.N. Anderson, M.W. Fox, P.H. Doherty, D.T. Decker, J.J. Sojka, and R.W. Schunk, "Parameterized ionospheric model: A global ionopsheric parameterization based on first principles models," Radio Science, vol. 30, pp. 1499–1510, Sept.-Oct. 1995.

[61] *Guide to Reference and Standard ionosphere Models*, American National Standards Institute, Reston, VA, Rep. ANSI/AIAA G-034-2011, 2011.

[62] (2014, Nov. 04).Parameterized ionospheric model (PIM) [Online]. Available: http://www.cpi.com/products/pim.html.

[63] D. Bilitza, ”Ionospheric models for radio propagation,” in Review of Radio Science: 1999–2002 URSI, W.R. Stone, Ed. : Wiley-IEEE Press, 2002, pp. 625–677.

[64] J.A. Klobuchar, “Ionospheric time-delay algorithm for single-frequency GPS users,” IEEE Transactions on Aerospace and Electronic Systems, vol. AES-23, pp. 325–331, Feb. 2007.

[65] J. Feldman. (n.d.). Parameterizing circles [Online]. Available: http://www.math.ubc.ca/~feldman/m317/circle.pdf.

[66] M.S. Butler, “Low cost, low complexity sensor design for non-cooperative geolocation via received signal strength,” M.S. thesis, Air Force Institute of technology, Wright-Patterson AFB, OH, 2012.

[67] K. Imani, POL 571, Topic: “Expectations and functions of random variables.” Princeton, NJ, Mar. 10, 1996.

INITIAL DISTRIBUTION LIST

1. Defense Technical Information Center
   Ft. Belvoir, Virginia

2. Dudley Knox Library
   Naval Postgraduate School
   Monterey, California